國 立 交 通 大 學

環境工程研究所

博 士 論 文

單一電極線電暈單極充電器

的奈米微粒充電效率改善研究

Improvement of the Nanoparticle Charging Efficiency

of a Single-wire Corona Unipolar Charger

研 究 生： 簡 誌 良

指導教授： 蔡 春 進 博士

吳 宗 信 博士

中 華 民 國 一 〇 一 年 六 月

單一電極線電暈單極充電器

的奈米微粒充電效率改善研究

Improvement of the Nanoparticle Charging Efficiency of a
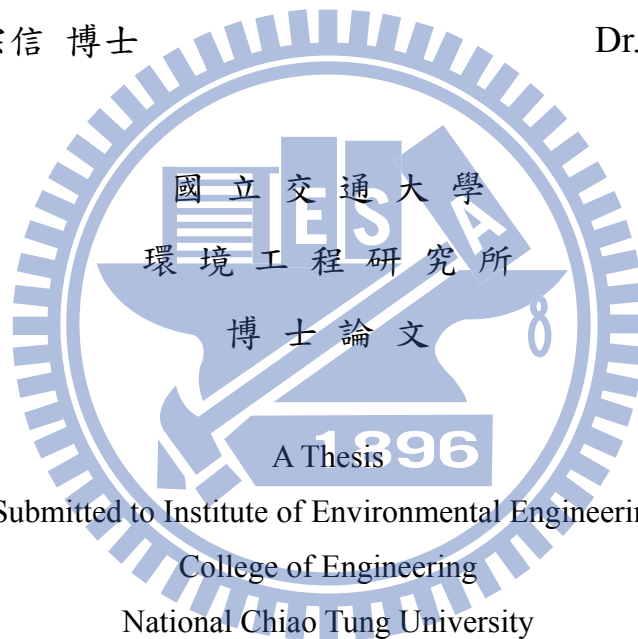
Single-wire Corona Unipolar Charger

研 究 生：簡誌良   Student: Chih-Liang Chien

指導教授：蔡春進 博士   Advisor: Dr. Chuen-Jinn Tsai

吳宗信 博士   Dr. Jong-Shinn Wu

國 立 交 通 大 學

環 境 工 程 研 究 所

博 士 論 文

A Thesis

Submitted to Institute of Environmental Engineering

College of Engineering

National Chiao Tung University

in Partial Fulfillment of the Requirements

for the Degree of

Doctor of Philosophy

in

Environmental Engineering

June 2012

Hsinchu, Taiwan, Republic of China

中 華 民 國 一〇一 年 六 月

單一電極線電暈單極充電器的奈米微粒充電效率改善研究

研究生：簡誌良　　　　　　　　　　　　指導教授：蔡春進 博士

　　　　　　　　　　　　　　　　　　　　　　　　　吳宗信 博士

國立交通大學環境工程研究所

摘　要

　　本研究的目的在於利用包覆空氣減少微粒損失進而提升電暈單極充電器的奈米微粒充電效率。首先設計一個具有軸向包覆空氣的充電器，其構造包含一個內徑 30 mm 的圓柱外殼，及使用一直徑為 50 μm、長度為 2 mm 的黃金電極線作為放電電極，並在固定氣膠流量 1 L/min 的條件下測試充電器對單徑 2.5～20 nm 銀微粒之充電效率。本研究並建立了一個二維數值模式來推估單極微粒充電器的奈米微粒充電效率，充電器內部的流場利用 SIMPLER 方法而得，電位場及離子濃度場則利用 Poisson 方程式及對流擴散方程式來求解；之後再利用對流擴散方程式配合 Fuchs 擴散充電理論求取帶電微粒的濃度場及充電效率。研究結果顯示，模擬的外在充電效率與實驗值相符。模擬結果說明了使用軸向包覆空氣減少帶電微粒損失的優點，並指出主要帶電微粒損失的發生位置。但由於較小的微粒較難被充電，使得具有軸向包覆空氣的充電器對粒徑小於 10 nm 的微粒之充電效率不佳，仍有改進的空間。

　　為進一步有效地提升奈米微粒的充電效率，本研究另設計一個具有徑向包覆空氣以減少帶電微粒損失的單一電極線單極氣膠充電器。此充電器之構造包含一個用來引入徑向包覆空氣的 6 mm 長接地多孔金屬套管，嵌入於內徑 6.35 mm 的絕緣鐵氟龍管正中央，及一直徑為 50 μm、有效長度為 6 mm 的放電黃金電極線。本

研究利用已建立的數值模式評估及最佳化此充電器的充電效能。研究過程中發現徑向包覆空氣的開口位置對減少帶電微粒損失的影響是重要的，故本研究針對兩種不同的充電器設計進行探討，在設計 1 中，徑向包覆空氣 6 mm 寬的開口兩端對準 6 mm 長的放電電極兩端，然而在設計 2 中，徑向包覆空氣的開口往電極線前端的左方偏移 2 mm。

與具有軸向包覆空氣的充電器比較，模擬結果顯示具有徑向包覆空氣的充電器之充電區並未觀察到迴流場的存在，在相同的操作條件下，因為帶電微粒沉降區的減少，使得設計 2 的靜電損失小於設計 1，模擬結果說明了使用徑向包覆空氣並配合適當包覆空氣的開口位置具有減少帶電微粒損失的優點。與目前文獻上具有最高外在充電效率的兩組單極氣膠充電器相較 (Chen and Pui 1999; Kimoto et al. 2010)，模擬結果顯示，針對 10 nm 以下微粒，在施加電壓為+3.5 kV、氣膠流量為 0.5 L/min 及包覆空氣流量為 0.7 L/min 時，具有徑向包覆空氣的充電器之設計 2 有相似的充電效能，對 2.5–10 nm 微粒的外在充電效率達到 15.2%–65.8%，而 Chen and Pui (1999)的充電器對 3–10 nm 微粒的外在充電效率為 22%–65%，Kimoto et al. (2010) 的充電器對 5–10 nm 微粒的外在充電效率為 59%–64%。

預期本研究設計的具有徑向包覆空氣的充電器可作為高效率的奈米微粒充電器，可改善監測儀器對奈米微粒的偵測靈敏度，未來可進行實驗驗證理論值以加強實用性。

Improvement of the Nanoparticle Charging Efficiency of a Single-wire Corona Unipolar Charger

Student: Chih-Liang Chien

Advisor: Dr. Chuen-Jinn Tsai

Dr. Jong-Shinn Wu

Institute of Environmental Engineering

National Chiao Tung University

ABSTRACT

The objective of this study is to develop a corona unipolar charger with sheath air to minimize particle loss and enhance the nanoparticle charging efficiency. At first, a unipolar charger with axial sheath air was designed which consists of a cylindrical casing of 30 mm in inner diameter in which a gold wire of 50 μm in diameter and 2 mm in length is used as the discharge electrode. The experimental charging efficiency was obtained at a fixed aerosol flow rate of 1 L/min using monodisperse silver nanoparticles of 2.5 to 20 nm in diameter. A 2-D numerical model was also developed to predict nanoparticle charging efficiency in the unipolar charger. Laminar flow field was solved by using the Semi-Implicit Method for Pressure Linked Equations (SIMPLER Method), while electric potential and ion concentration fields were solved based on Poisson and convection-diffusion equations, respectively. The charged particle concentration fields and charging efficiency were then calculated based on the convection-diffusion equation incorporating the Fuchs diffusion charging theory (Fuchs 1963). Good agreement between simulated and experimental extrinsic charging efficiency was obtained. Numerical results show the advantage of using axial sheath air to minimize charged particle loss and indicate the location where major charged particle loss occurs. However, the extrinsic charging efficiency of the charger with axial sheath air is still
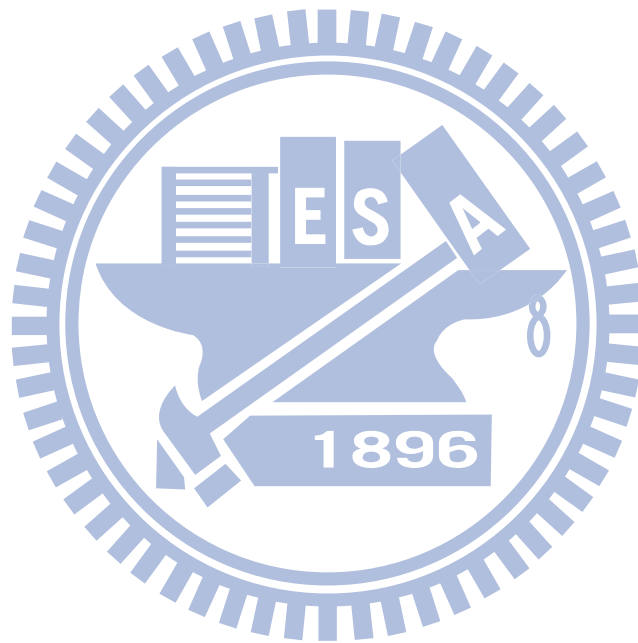
low for particles smaller than 10 nm in diameter due to low intrinsic charging efficiency.

In order to improve the design of the charger, a single-wire corona unipolar charger with radial sheath air to minimize charged particle loss was proposed to enhance the charging efficiency of nanoparticles. The charger consists of an insulated Teflon tube (inner diameter ID = 6.35 mm) with a 6 mm long grounded porous metal tube inserted at the center from which radial sheath air is introduced, and a discharge gold wire of 50 μm in ID and 6 mm in effective length. The performance of the charger was evaluated and optimized by the present numerical model. The effect of the position of the sheath air opening on reducing the loss of charged particles was found to be important and two different designs were studied. In design 1, both ends of 6 mm wide sheath air opening are aligned with the ends of 6 mm long discharge wire, while in design 2 the sheath air opening is shifted 2 mm toward the left of the leading edge of the wire.

Compared to the charger with axial sheath air, numerical results show that no flow recirculation region is observed in the charging zone of the charger with radial sheath air. At the same operating condition, design 2 was found to have less electrostatic loss than design 1 because of its smaller deposition region of charged particles. Numerical results show the advantage of using radial sheath air with an appropriate position of the sheath air opening to minimize charged particle loss. Compared with two existing unipolar chargers with the highest extrinsic charging efficiency for particles smaller than 10 nm in diameter (Chen and Pui 1999; Kimoto et al. 2010), results show that design 2 operated at the applied voltage of +3.5 kV, aerosol flow rate of 0.5 L/min, and sheath air flow rate of 0.7 L/min was found to have extrinsic charging efficiency of 15.2%–65.8% for particles ranging from 2.5 to 10 nm in diameter, which is comparable to that of the charger of Chen and Pui (1999), 22%–65% for particles ranging from 3 to 10 nm in diameter, and that of the charger of Kimoto et al. (2010), 59%–64% for particles

ranging from 5 to 10 nm in diameter.

It is expected that the charger with radial sheath air designed in this study could be used as an efficient nanoparticle charger to improve the sensitivity of monitoring instruments for nanoparticles. In the future, the experiments will be conducted to validate the simulated results and to further enhance the feasibility of the charger.
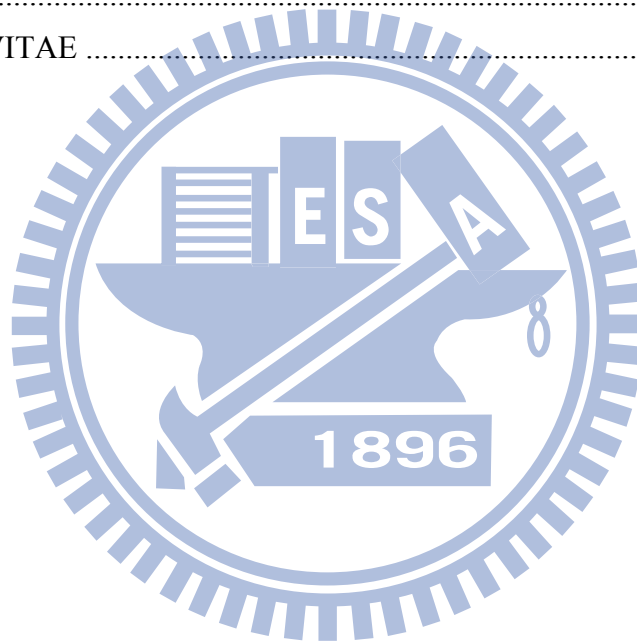
ACKNOWLEDGMENTS

TABLE OF CONTENTS

VIII

LIST OF TABLES

LIST OF FIGURES

XII

NOMENCLATURE

English symbols

A	cross area for ions (m^2)
a	radius of particles (m)
C_c	slip correction factor
C_{in}	particle number concentration measured upstream of the charger (particles/m^3)
$C_{out,OFF}$	particle number concentration measured downstream of the second ESP when no voltage is applied on the charger and the second ESP (particles/m^3)
C_{out}^0	particle number concentration measured downstream of the charger when the charger is on and sufficiently high voltage is applied on the second ESP (particles/m^3)
$C_{out,ON}$	particle number concentration measured downstream of the charger when the charger is on and the second ESP is off (particles/m^3)
$\bar{c}_i$	mean thermal speed of ions (m/s)
D_i	ion diffusion coefficient (m^2/s)
D_B	Brownian diffusion coefficient of particles (m^2/s)
d_p	particle diameter (m)
d_w	diameter of the discharge wire (m)
E	electric field strength (V/m)
E_b	breakdown voltage (kV/m)
E_r	electric field strength in radial direction (V/m)
E_w	electric field on the corona wire surface (kV/cm)
E_z	electric field strength in axial direction (V/m)
e	elementary charge (C)
f	dilution factor

G_{IN}	first iteration correction to the flux
I	corona current (A)
Kn	Knudsen number
k_b	Boltzmann constant (J/K)
L_d^0	diffusion loss of uncharged particles
$L_{con-dif}^c$	convection-diffusion loss of charged particles
L_{el}	electrostatic loss
M_{air}	molecular weights of air (kg/mol)
M_i	molecular weights of ions (kg/mol)
N_a	Avogadro number (#/mol)
$N_{con-dif}^c$	convection-diffusion deposition rate of charged particles (particles/s)
N_{el}	electrostatic deposition rate of charged particles (particles/s)
N_i	ion number concentration (ions/m^3)
N_{in}	rate of uncharged particles entering the inlet of the charger (particles/s)
N_{out}^c	rate of charged particles exiting the charger (particles/s)
$N_{p,q}$	concentration of particles carrying q elementary charges (particles/m^3)
$N_{p,T}$	concentration of total charged particles (particles/m^3)
N_T	concentration of total uncharged particles at the inlet (particles/m^3)
P	pressure (Pa)
P_0	pressure (atm)
P_{ESP}	penetration of uncharged particles through the second ESP
Q_a	aerosol flow rate (L/min)
Q_{sh}	sheath air flow rate (L/min)
q	number of charges carried by particles

r	distance between particles and ions center (m)
r_a	apsoidal distance (m)
r_t	radius of the tube (m)
r_w	radius of the discharge wire (m)
S_c	source term
S_p	sink term
T	temperature (K)
T_0	temperature (K)
t	charging time (sec)
u_r	air velocity in radial direction (m/s)
u_z	air velocity in axial direction (m/s)
V	electric potential (Volt)
V_c	critical voltage for the corona generation (Volt)
Z_i	ion mobility (m^2/s·V)
Z_P	particle electrical mobility (m^2/s·V)

Greek letters

α_0	combination coefficient between an ion and an uncharged particle (m^3/s)
α_q	combination coefficient of ions for particles carrying q elementary charges (m^3/s)
α^*	charging parameter
δ	relative density of air
δ_r	radius of the limiting sphere (m)
ε_0	permittivity of air (A·s/Volt·m)
ε_p	dielectric constant of particles

η_{ext}	extrinsic charging efficiency
η_{int}	intrinsic charging efficiency
θ	dimensionless parameter
λ_i	mean free path of ions (m)
μ_{air}	air viscosity (kg/m·s)
ξ	striking probability
ρ_{air}	air density (kg/m^3)
ρ_i	space charge density (C/m^3)
$\rho_{i,0}$	space charge density at the discharge wire surface (C/m^3)
ϕ	electric potential between the particle and the ion (Volt)

Additional superscripts

0	uncharged particles
c	charged particles
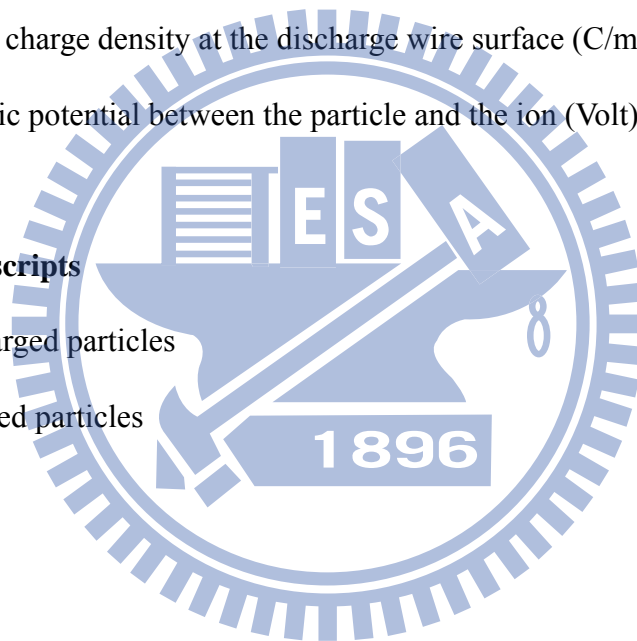
CHAPTER 1
INTRODUCTION

1.1 Motivation

Nanomaterial is defined as a material with any external dimension in the nanoscale or having internal structure or surface structure in the nanoscale. This generic term is inclusive of nano-object and nanostructured material (ISO/TS 80004-1:2010), in which nanoparticle is one of the types of nano-object with all three external dimensions in the nanoscale (ISO/TS 27687:2008; ISO/TS 80004-3:2010). Nanoparticles possess many unique physical, chemical and biological properties which lead to their diverse applications. However, some of the same unique properties that make nanoparticles useful are also properties that may cause nanoparticles harmful to humans or the environment. Many parameters such as size, shape, density, surface characteristics and composition influence the behavior, fate, transport, and toxicity of nanoparticles. Among them, size is one of the most important parameters. Therefore, it is important to characterize the size of nanoparticles accurately.

The differential mobility analyzer (DMA) shows the greatest promise for accurate sizing and classification of nanoparticles (Chen et al. 1998). To operate the DMA, aerosol particles must first be charged electrically to a known charge distribution on which nanoparticle sizing and classifying is based. In electrical aerosol instruments, the most commonly used techniques for charging particles is diffusion charging. Diffusion charging of particles can be either unipolar or bipolar, depending on the polarity of the ions colliding with particles. In unipolar charging, ions of only one polarity are present, and particles increase their charge with time. In bipolar charging, both positive and negative ions are present, and particles will acquire charges with time by attachment of ions of the opposite polarity until they reach an equilibrium charge distribution. This

process is also known as charge neutralization.

Bipolar diffusion chargers are commonly used with DMAs in scanning mobility particle sizers (SMPSs) (model 3085, TSI Inc.; Wang and Flagan 1990) for the measurement of particle size distribution because of a well defined charge distribution. However, the charging efficiency for nanopaticles is low because both charging and neutralization mechanisms happen at the same time, which is only 0.7%–4% and 0.8%–5%, respectively, for positively and negatively charged particles of 2–10 nm in diameter (Wiedensohler 1988). In other words, lots nanoparticles would be wasted during the classification process (Chen and Pui 1999). In addition, the extremely low nanoparticle charging efficiency of bipolar chargers could lead to low sensitivity in detecting nanoparticles with low concentration. Therefore, it is desirable to have high concentration of charged nanoparticles from the charger and before they are classified by the DMA.

Unipolar diffusion chargers provide higher charging efficiency than bipolar diffusion chargers because the recombination of charged particle with the ions of opposite polarity is avoided. To achieve high charging efficiency, various unipolar chargers were developed using corona discharge, ionizing radiation, soft X-rays or UV-light techniques to generate ions for diffusion charging (Kimoto et al. 2010; Intra and Tippayawong 2011). Among these techniques, corona discharge can produce unipolar ions at a high enough concentration for efficient diffusion charging (Hinds 1999). In comparison, radioactive sources are often undesirable due to the tight regulatory restriction, and soft X-rays sources are expensive. Moreover, the charging efficiency of UV-light technique is strongly material-dependent (Kulkarni et al. 2011).

Current commercial instruments that employ corona unipolar chargers include the electrical aerosol analyzer (EAA, model 3030, TSI Inc.), the ultrafine particle monitor

(UFP Monitor, model 3031, TSI Inc.), the electrical aerosol detector (EAD, model 3070A, TSI Inc.), the engine exhaust particle sizer (EEPS, model 3090, TSI Inc.), the fast mobility particle sizer (FMPS, model 3091, TSI Inc.), the nanoparticle surface area monitor (NSAM, model 3550, TSI Inc.; DC2000CE, EcoChem Analytics, League City, TX, USA), the portable nanoparticle aerosol monitor to determine lung-deposited surface area concentration (Aerotrak 900, TSI Inc.) and nanoparticle concentrations (Nanocheck, model 1.320, Grimm Aerosol Technik GmbH, Ainring, Germany; Nanotracer, Philips Areasense, Eindhoven, Netherlands), and the electrical low pressure impactor (ELPI, Dekati Ltd., Tampere, Finland).

Numerous corona-based unipolar chargers were designed using either a wire or a needle as the discharge electrode (Hewitt 1957; Whitby 1961; Kruis and Fissan 2001; Hernandez-Sierra et al. 2003; Unger et al. 2004; Biskos et al. 2005a; Alonso et al. 2006; Qi et al. 2008; Li and Chen 2011). Some designs involved mixing ion jet flow with aerosol flow in the charging chamber without an external electric field to reduce charged particle loss (Medved et al. 2000; Marquard et al. 2006a; Park et al. 2007; Qi et al. 2007; Kimoto et al. 2010). However, high efficiency charging is still difficult to obtain for nanoparticles smaller than 10 nm. Therefore, an aerosol charger with higher charging efficiency in this size range is needed to improve the sensitivity and accuracy of monitoring instruments for nanoparticles.

Some corona-wire charger designs have an additional sheath air flow either near the wall of the charger to reduce charged particle loss or around the discharge wire to prevent accretion of particles in the charging chamber. In the charger with axial sheath air, sheath air is introduced into the charging chamber in the same direction as the aerosol flow in the axial direction of the charger (Liu and Pui 1975; Büscher et al. 1994; Biskos et al. 2005b; Tsai et al. 2008, 2010), while sheath air is introduced into the

charging chamber perpendicular to the aerosol flow in the charger with radial sheath air (Cheng et al. 1997). For the charger with axial sheath air in Tsai et al. (2010), the extrinsic charging efficiency, defined as the intrinsic charging efficiency minus electrostatic loss, was higher than that of many existing corona-based unipolar chargers but lower than two unipolar chargers, which have the highest extrinsic charging efficiency for particles smaller than 10 nm in diameter. One of the charger was developed by Chen and Pui (1999) with the extrinsic charging efficiency of 22%–65% (d_p = 3–10 nm; d_p: particle diameter). The other is the charger of Kimoto et al. (2010) with the extrinsic charging efficiency of 59%–64% (d_p = 5–10 nm). For the charger of Kimoto et al. (2010), no extrinsic charging efficiency for particles with $d_p < 5$ nm was reported. In addition, charged particle loss was reduced but the charging efficiency was not reported for the charger with radial sheath air (Cheng et al. 1997). Therefore, the effect of radial sheath air on the charging efficiency and the optimization of the charger remain to be studied.

Diffusion charging has been studied theoretically and various models are available. Detailed overview on the diffusion charging models in all aerosol regimes can be seen in the literature (Romay and Pui 1992a; Biskos et al. 2004; Marquard 2007). For the unipolar charger, a comprehensive model, including the calculation of the flow, electrical potential, and ion concentration fields in the charging zone, is needed to predict the extrinsic charging efficiency and charged particle concentration field accurately (Qi et al. 2008). But so far no such detailed numerical models are currently available. An accurate numerical model which can be used to facilitate the design of an efficient unipolar charger for charging nanoparticles needs to be developed. Recently, Lin and Tsai (2010) developed a 2-D numerical model to predict the nanoparticle collection efficiency in single-stage wire-in-plate electrostatic precipitators (ESPs). The

flow filed, electric potential, and ion concentration fields in the ESPs were solved first. The charged particle concentration field and particle collection efficiency were then calculated based on the convection-diffusion equation in which particle charging was calculated by Fuchs theory (1963). The numerical model of Lin and Tsai (2010) was able to predict the experimental nanoparticle collection efficiency very well for particles smaller than 20 nm in diameter.

1.2 Objectives of this study

The objectives of this study are summarized as:

1. To design a corona-wire unipolar aerosol charger with axial sheath air to minimize particle loss and use experimental method to determine an optimum operating condition and investigate the charging efficiency.

2. To develop a 2-D numerical model to predict nanoparticle charging efficiency in the unipolar charger with axial sheath air and validate it with the experimental data.

3. To simulate a corona-wire unipolar aerosol charger with radial sheath air to enhance the charging efficiency of nanoparticles and evaluate the performance of the charger to determine an optimum operating condition numerically.

1.3 Content of this thesis

In chapter 2, literature related to the previous designs and numerical studies of the corona unipolar chargers is reviewed. In chapter 3, the experimental methods for evaluating the performance of the charger with axial sheath air designed in this study are presented first, followed by the numerical methods for predicting the flow, electric potential, ion concentration, and charged particles concentration fields.

Chapter 4 first covers the experimental results for the optimum operating condition of

the charger with axial sheath air and the comparison of experimental data and numerical results. Then the numerical results for the performance evaluation of two designs of the charger with radial sheath air are presented. Finally, the predicted extrinsic charging efficiency of the charger with radial sheath air is compared with the highest extrinsic charging efficiency of the previous unipoalr chargers (Chen and Pui 1999; Kimoto et al. 2010). In chapter 5, the conclusions of this thesis are drawn and future work is recommended.

CHAPTER 2
LITERATURE REVIEW

A variety of unipolar chargers have been designed to generate ions by radioactive sources (Adachi et al. 1985, 1992; Romay et al. 1991; Romay and Pui 1992a; Wiedensohlor et al. 1994). In the charger of Adachi et al. (1992), as shown in Figure 2.1, the charger consisted of a Po^{210} radioactive source placed between two screen electrode enclosed by a Plexglass tube. When a positive voltage was applied to the inlet screen electrode and the out electrode was grounded, a uniform electric field was established between the electrodes. Negative ions were attracted to the inlet electrode, while positive ions flowed to the outlet electrode.
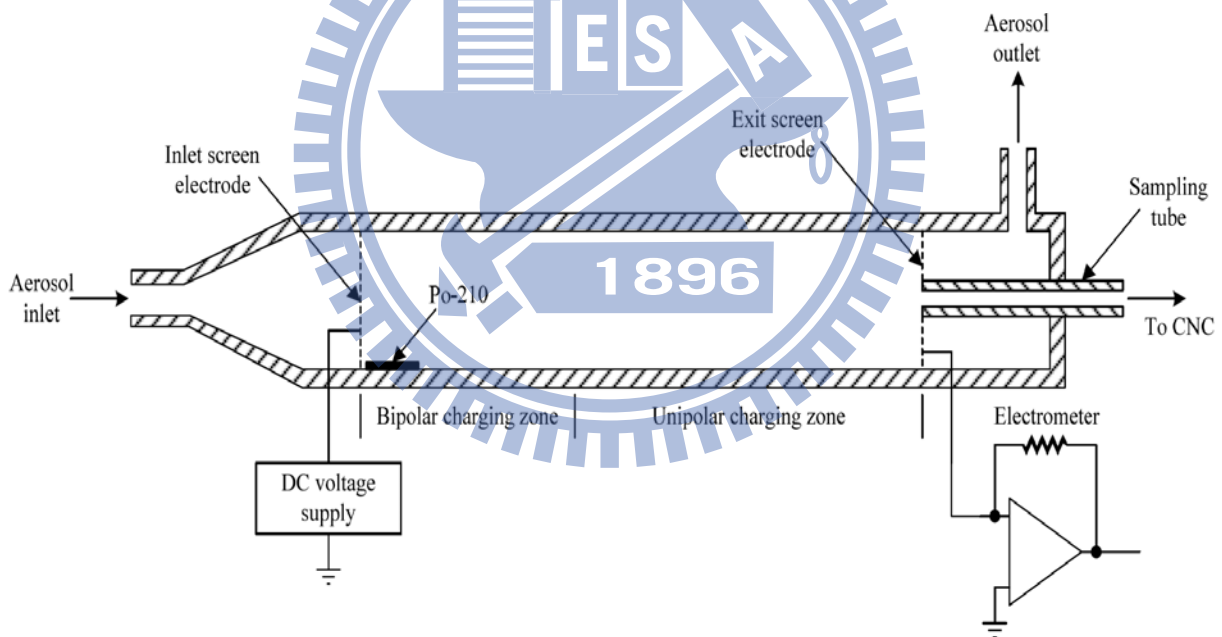
Figure 2.1 Schemataic diagram of the unipolar charger using a radioactive source developed by Adachi et al. (1992). (from Intra and Tippayawong, 2011)

In a later work, Chen and Pui (1999) designed a unipolar charger with the parallel configuration of aerosol and ion flow, as shown in Figure 2.2. A relatively weak electrical field was applied to keep the same polarity ions and collect the opposite

polarity ions from a Po^{210} radioactive source. The design further used a sheath air surrounding the aerosol flow to keep charged particles in the core region to minimize electrostatic loss. The extrinsic charging efficiency was found as high as 22% for 3 nm, 48% for 5 nm, and 65% for 10 nm particles. So far, this design has the highest extrinsic charging efficiency for particles smaller than 5 nm in diameter among all unipolar chargers. However, the issue of tight safety regulations on using radioactive sources remains. Moreover, the unipolar charger using radioactive sources required an electric field to separate the positive and negative ions is also referred to as a relatively complicated design. These technical features complicate the structure of the particle charging apparatus, resulting in the increase of cost and causing the apparatus unable to be miniaturized for the use in a portable particle measuring instrument. Charging nanoparticles with unipolar ions produced by corona discharge instead of by radioactive sources is therefore a preferred option.
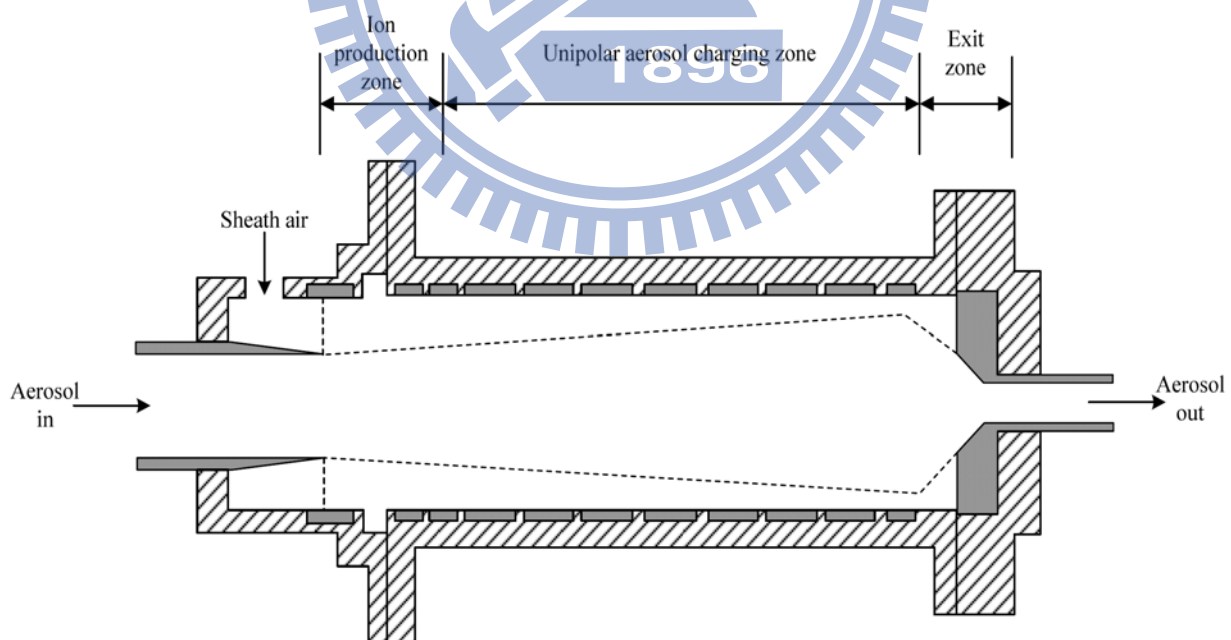
Figure 2.2 Schemataic diagram of the unipolar charger using a radioactive source developed by Chen and Pui (1999). (from Intra and Tippayawong 2011)

2.1 Previous corona unipolar chargers

Numerous corona-based unipolar chargers were designed to achieve high charging efficiency using either a wire or a needle as the discharge electrode. Compared to the typical unipolar chargers using radioactive sources, the advantages of the corona unipolar chargers are the higher ion concentration and the elimination of radioactive sources. Intra and Tippayawong (2009, 2011) presented a detailed review of the corona-based unipolar chargers including the operating principles and physical characteristics of these chargers. The following paragraphs give a brief overview of the different designs of corona unipolar chargers and a comparison of the charging efficiency based on the work of Intra and Tippayawong (2009, 2011). The corona-wire chargers without sheath air are introduced first, followed by the corona-wire chargers with sheath air and corona-needle chargers.

In the corona-wire chargers without sheath air, Hewitt (1957) was one of the first to develop a corona-wire diffusion charger, as shown in Figure 2.3. The Hewitt charger consisted of a cylinder with a concentric wire along the axis. The corona discharge and aerosol flow region were separated by a metallic mesh and an alternating voltage (AC) was applied between the mesh and the outer electrode of the charger to reduce particles loss. Hewitt reported that the electric field strength resulted in high electrostatic loss for particles with a diameter as small as 70 nm. An improvement on the corona-wire charger based on the Hewitt's design was carried out by Kruis and Fissan (2001). It was called the twin Hetwitt charger, as shown in Figure 2.4. The charging zone of this charger was separated from two ion production zones by the metal wire screens connected to two square-wave generators to prevent the expansion of aerosol flow into the corona discharge zone. Ions were produced in two cylindrical sections with an Au wire placed in the center of the metal cylinder. It was reported that the extrinsic

charging efficiency of this charger as high as about 5% for 5 nm particles.
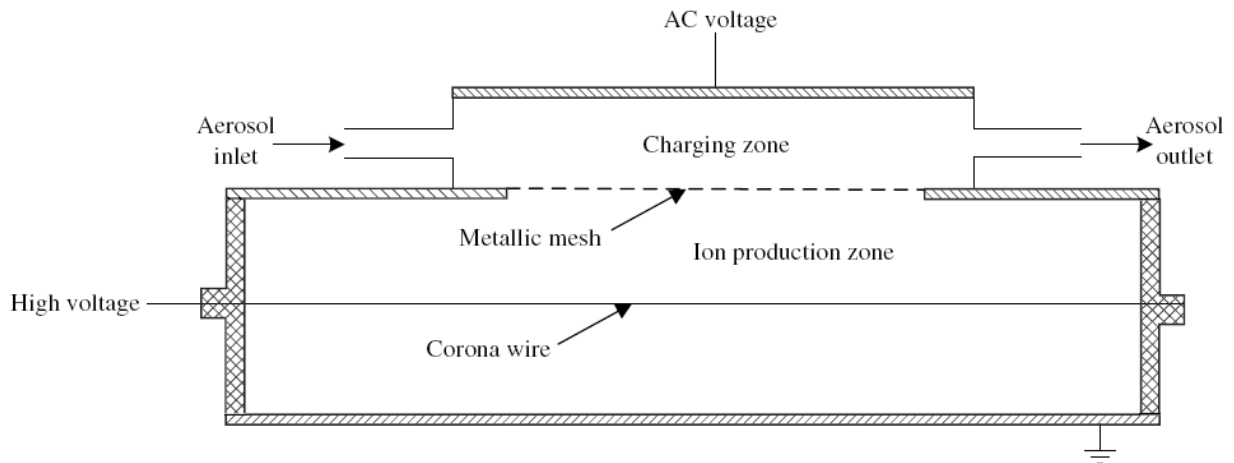
Figure 2.3 Schemataic diagram of the corona-wire charger developed by Hewitt (1957). (from Intra and Tippayawong 2009)
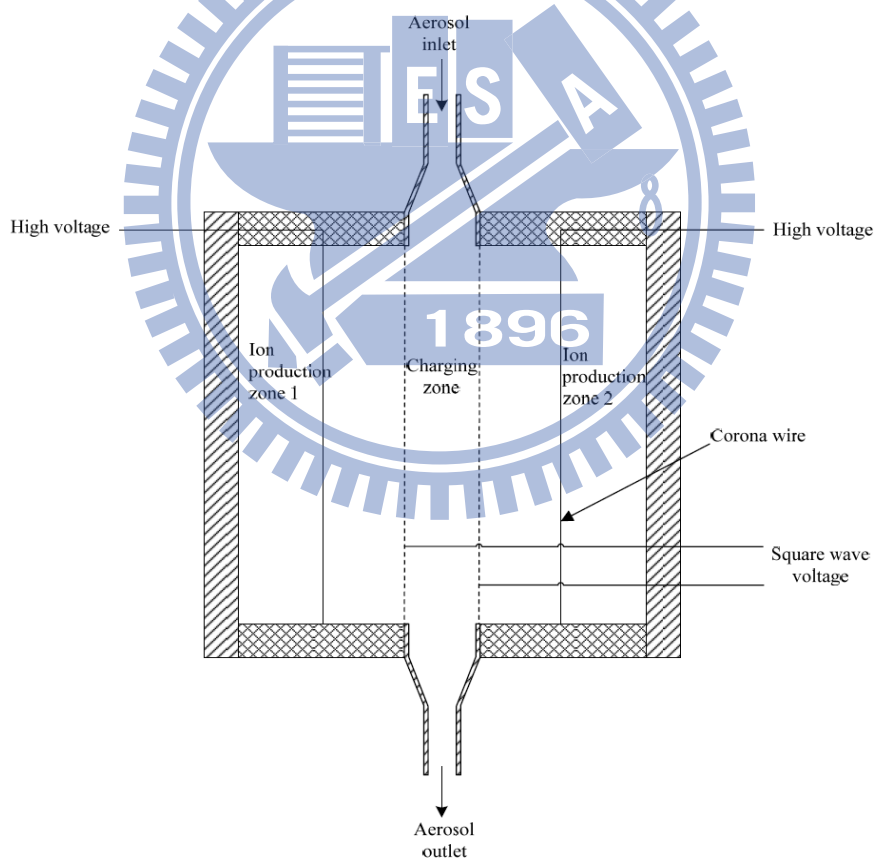
Figure 2.4 Schemataic diagram of the twin Hetwitt charger developed by Kruis and Fissan (2001). (from Intra and Tippayawong 2011)

10

Biskos et al. (2005a) later developed a Hewitt-type corona charger, shown in Figure 2.5, consisted of two concentric electrodes with a tungsten wire placed along the axis. The generated ions migrated toward the inner electrode due to the high electric field. The inner electrode was made of a metallic mesh to allow the ions to flow in the charging zone. An AC voltage was applied on the outer electrode forced ions to enter the charging zone without causing charged particles to deposit on the wall of the charger while the perforated inner electrode was grounded. No extrinsic charging efficiency was reported for this charger.
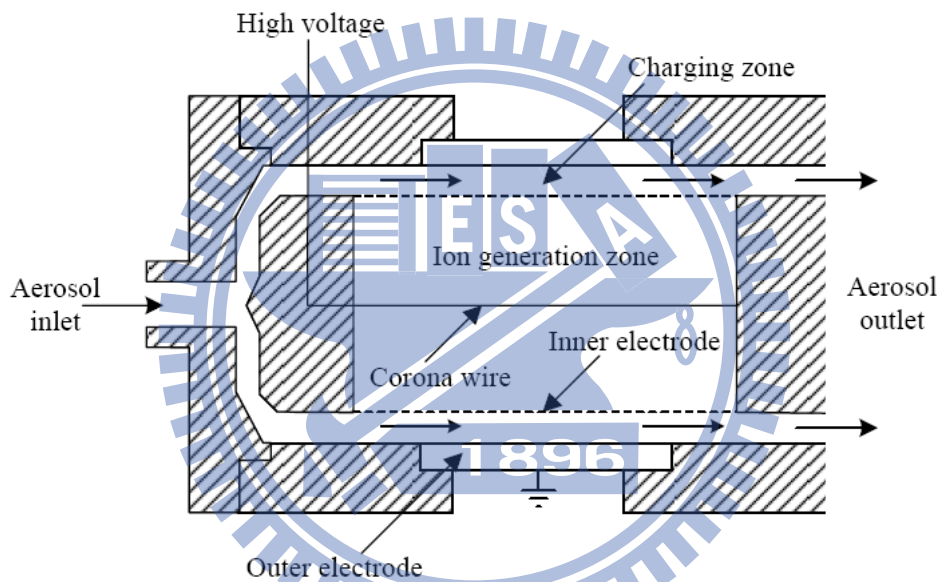
Figure 2.5 Schemataic diagram of the corona-wire unipolar charger developed by Biskos (2005a). (from Intra and Tippayawong 2011)

In the corona-wire chargers with sheath air, the unipolar charger used in the commercial electrical aerosol analyzer (EAA, model 3030, TSI Inc.) was designed by Liu and Pui (1975). As shown in Figure 2.6, the charger consisted of two concentric metal cylinders with a tungsten wire placed along the axis of the cylinders. A high voltage was applied to the wire to produce a corona discharge from the wire. The ions were forced through the coaxial screen opening on the inner cylinder into the annular

gap region between the cylinders. The aerosol stream flowing in the annular gap was exposed to the unipolar ions. Axial sheath air was used to minimize particles from entering the corona cylinder. The performance of this charger in the nanoparticle range was reported by Pui et al. (1988). Significant charged particle loss was found below 10 nm. An improvement on this charger was designed by Büscher et al. (1994). As shown in Figure 2.7, an AC electric field was applied in the charging zone to reverse the direction of the charged particles before they deposit on the wall. Axial sheath air was also used to prevent particles from entering the corona discharge zone. With this improvement, the charger achieves a 4% extrinsic charging efficiency for 5 nm particles.
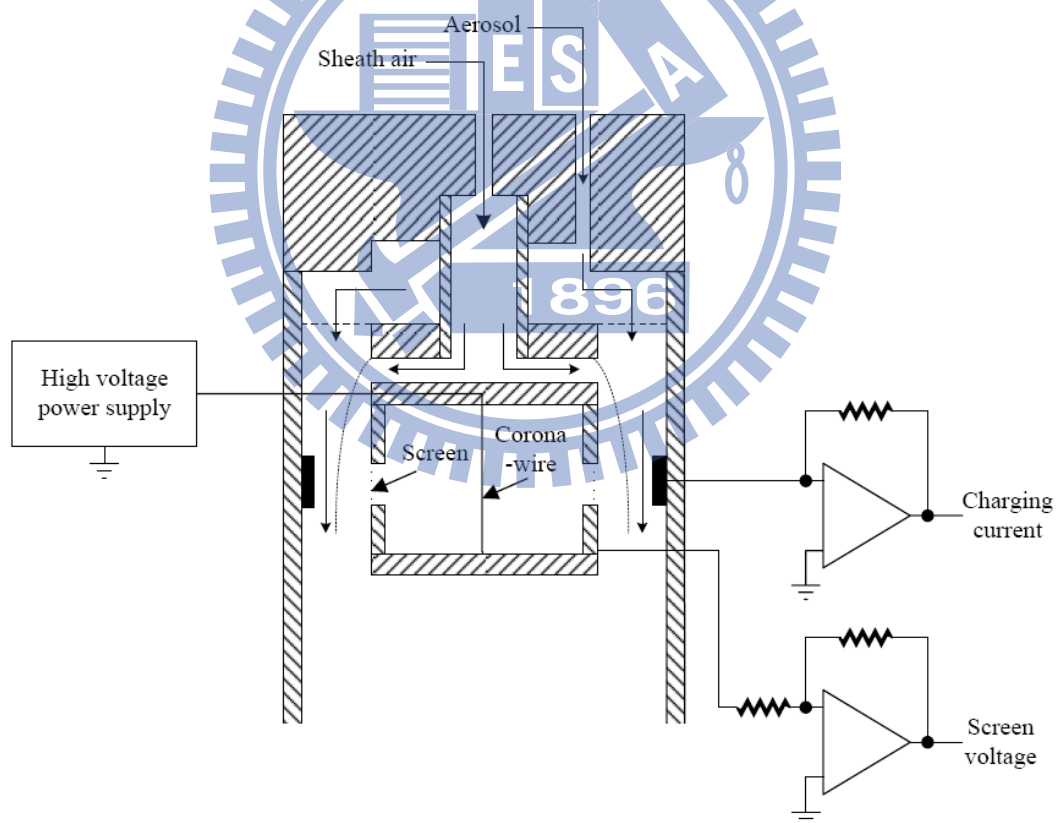
Figure 2.6 Schemataic diagram of the corona-wire unipolar charger developed by Liu and Pui (1975). (from Intra and Tippayawong 2011)
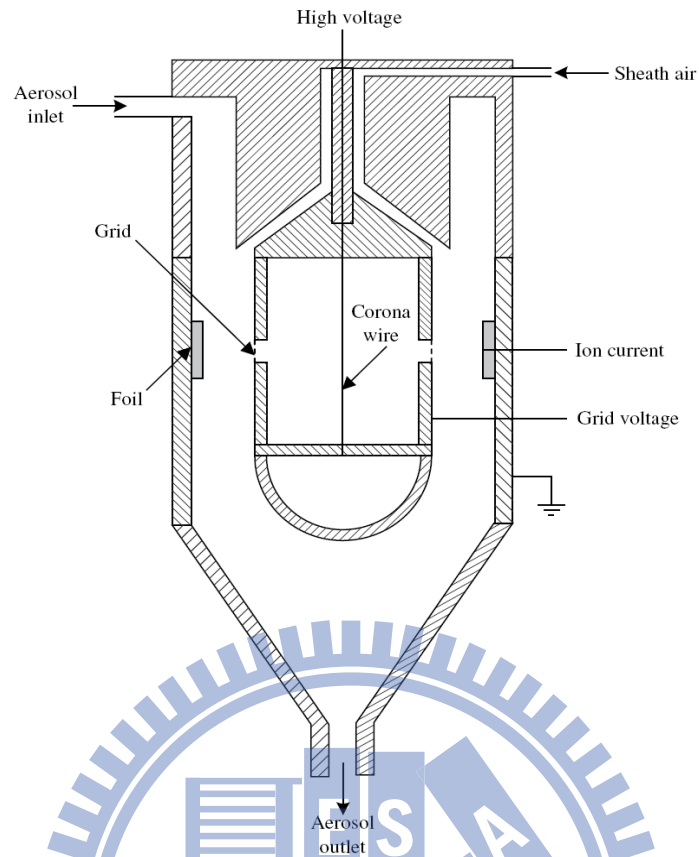
Figure 2.7 Schemataic diagram of the corona-wire charger developed by Büscher et al. (1994). (from Intra and Tippayawong 2009)

Cheng et al. (1997) developed a high-volume corona charger, shown in Figure 2.8, having flow rate of 0.6–6.0 m³/s with radial sheath air through the grounded porous wall of the metal tube to minimize the electrostatic loss, while the annulus aerosol flow was parallel to the six discharge wires mounted around a Teflon rod holder in the axial direction of the charger. The loss of charged particles in the submicron size range in the charger can be reduced by using radial sheath air at the flow rate of 2.4 m³/s or greater, but the extrinsic charging efficiency was not reported.
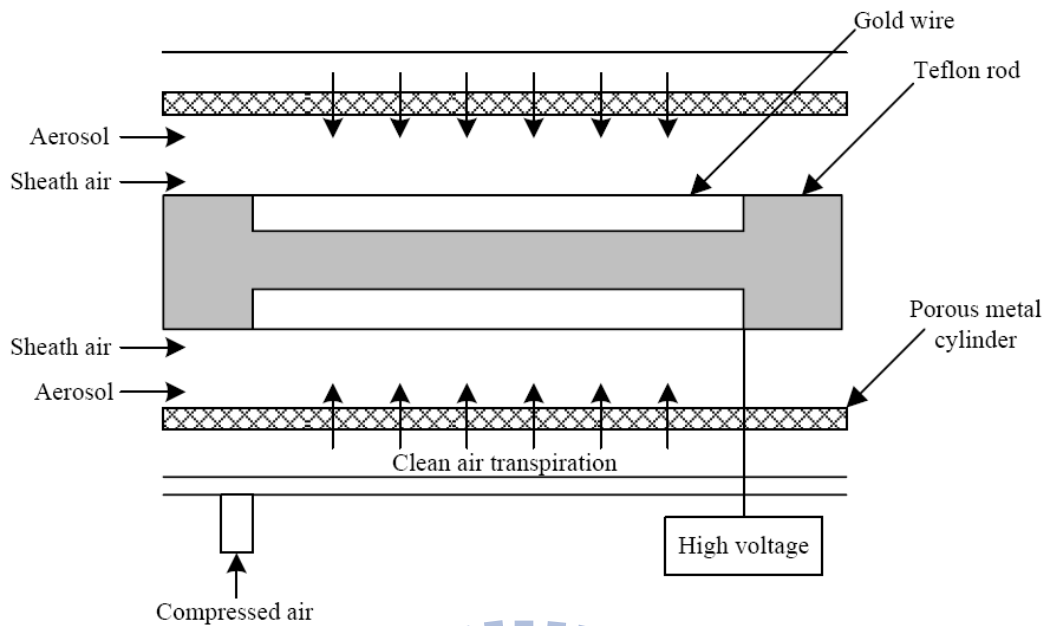
Figure 2.8 Schemataic diagram of the corona-wire unipolar charger developed by Cheng et al. (1997). (from Intra and Tippayawong 2011)

As shown in Figure 2.9, Biskos et al. (2005b) improved the design of Biskos et al. (2005a) with axial sheath air to achieve a high aerosol penetration and laminar flow inside the charger. The extrinsic charging efficiency of this charger was reported as high as about 24.9% for 10 nm particles. Recently, Tsai et al. (2008, 2010) developed a unipolar with multiple discharge wires to enhance the extrinsic charging efficiency by using axial sheath air near the wall of the charger to reduce the electrostatic loss of nanoparticles. This charger is shown schematically in Figure 2.10. The charger had a Teflon core to fix four gold wires and the outer stainless steel casing was grounded. To reduce charged particle loss in the charging zone, a clean sheath air was introduced from the 0.1 mm annular slit formed by the aluminum shroud and the outer casing. The performance of the charger was evaluated under different operating conditions including sheath air flow rates, corona voltages, and particles sizes. The highest extrinsic charging efficiency was 2.8%–86.3% for particles of 2.5–50 nm in diameter at the applied voltage of +9 kV, aerosol flow rate of 10 L/min, and sheath air flow rate of 20 L/min.
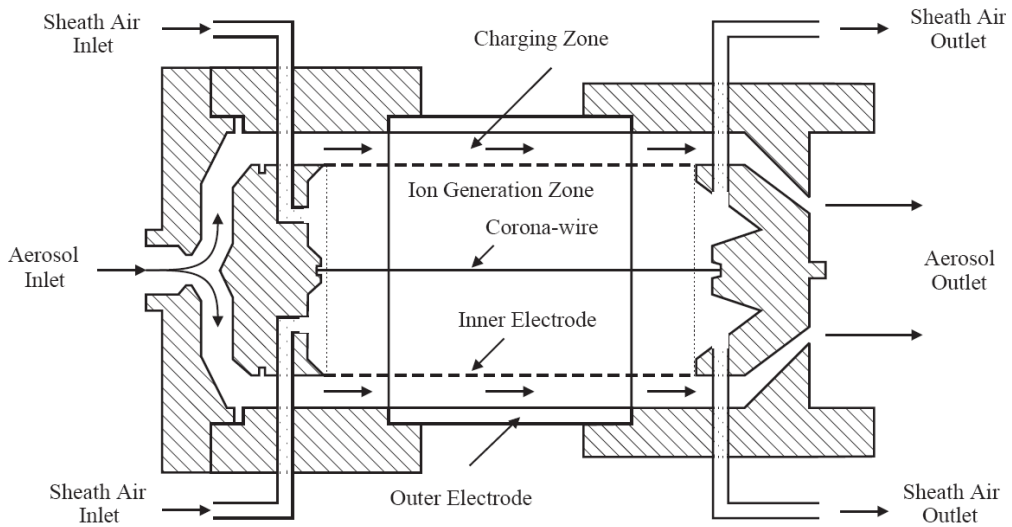
Figure 2.9 Schemataic diagram of the corona-wire unipolar charger developed by Biskos (2005b).
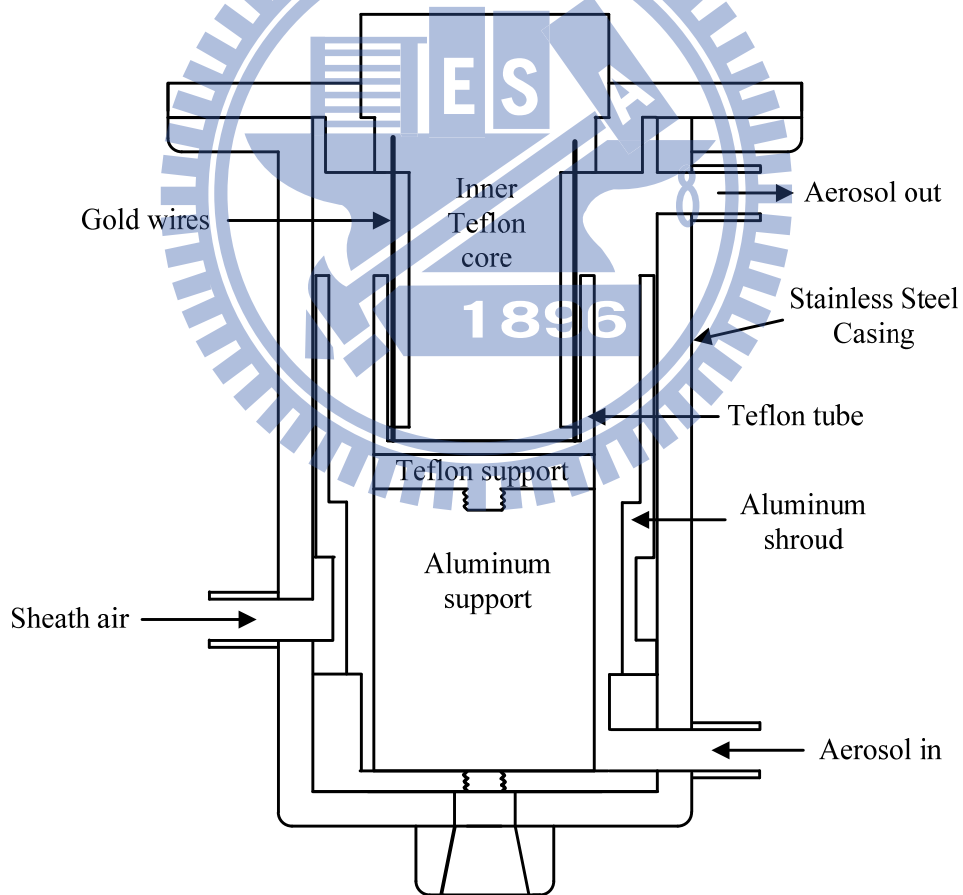
Figure 2.10 Schemataic diagram of the corona-wire unipolar charger developed by Tsai et al. (2008, 2010).

In the corona-needle chargers, Whitby (1961) developed the first needle-type corona charger, shown in Figure 2.11, which consisted of an arrangement of a sharp needle at high voltage upstream of a sonic orifice to generate the ions within a non-conductive housing. Clean air entered at the inlet then passed through the orifice. It was reported that the ion concentration can be up to 10^{17} ions/m^3 in the charging zone. A simple corona-needle charger for charging nanoparticles was proposed by Hernandez-Sierra et al. (2003), as shown in Figure 2.12. The design was a cylinder tube with tapered ends and divided into three sections. The first and second sections were made of methacrylate and the third (outlet) section of aluminum. A circular piece made of Teflon, placed between the two methacrylate sections, contained a series of orifices through the aerosol flows. The central piece was used to hold a stainless steel needle electrode, ending in a sharp tip coaxial with the cylinder. The outlet metallic section was grounded. It was reported that the extrinsic charging efficiency of this charger as high as about 2.1% for 2.7 nm particles.
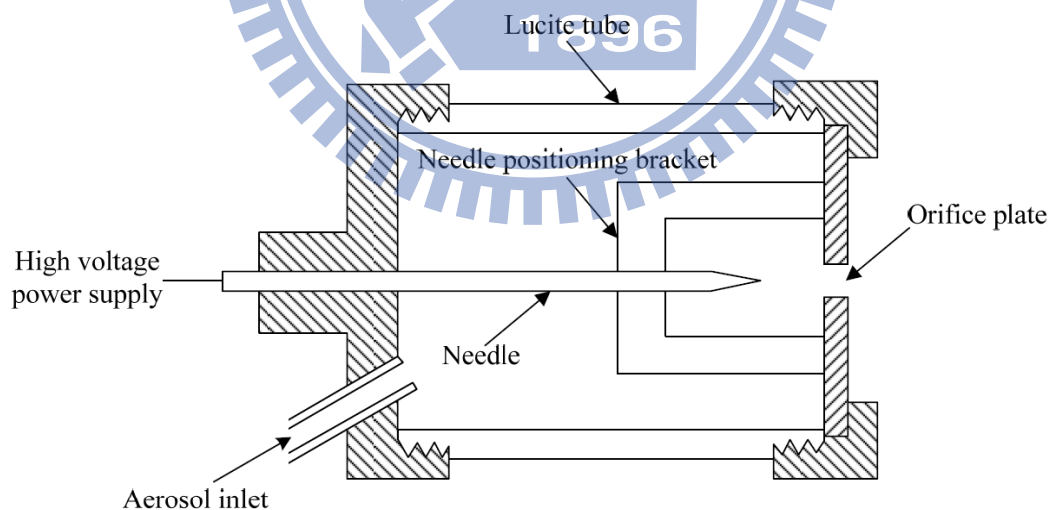
Figure 2.11 Schemataic diagram of the corona-needle unipolar charger developed by Whitby (1961). (from Intra and Tippayawong 2011)
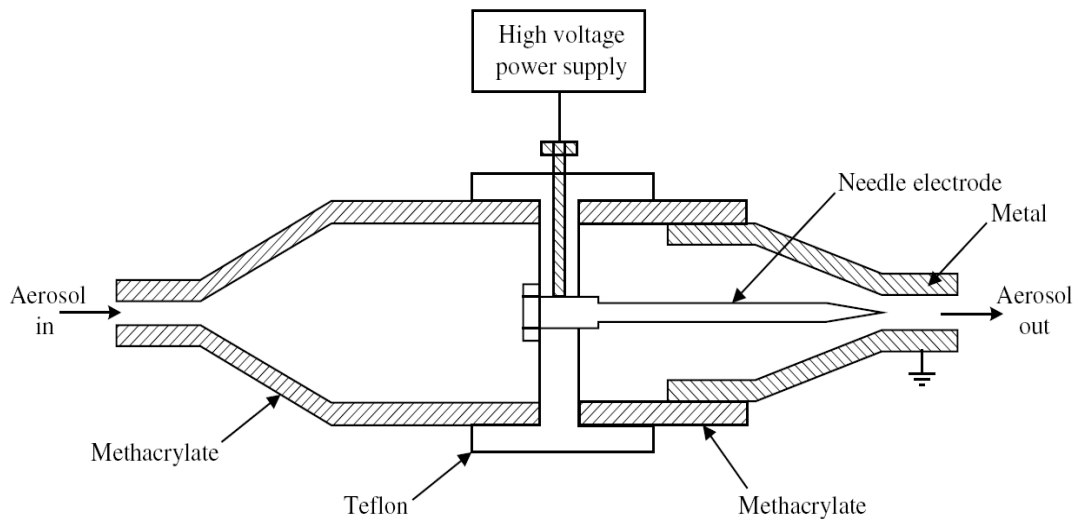
Figure 2.12 Schemataic diagram of the corona-needle unipolar charger developed by Hernandez-Sierra et al. (2003). (from Intra and Tippayawong 2009)

Later on, an improvement on the charger of Hernandez-Sierra et al. (2003) was made by Alonso et al. (2006) by modifying aerosol inlet geometry as well as the manner holding the discharge electrode shown schematically in Figure 2.13. It consisted of an inner stainless steel electrode ending in a sharp tip. The electrode is coaxial with a grounded metal cylinder which inner wall has a conical shape. The extrinsic charging efficiency of the charger of Alonso et al. (2006) was 1.8% for 3 nm particles.
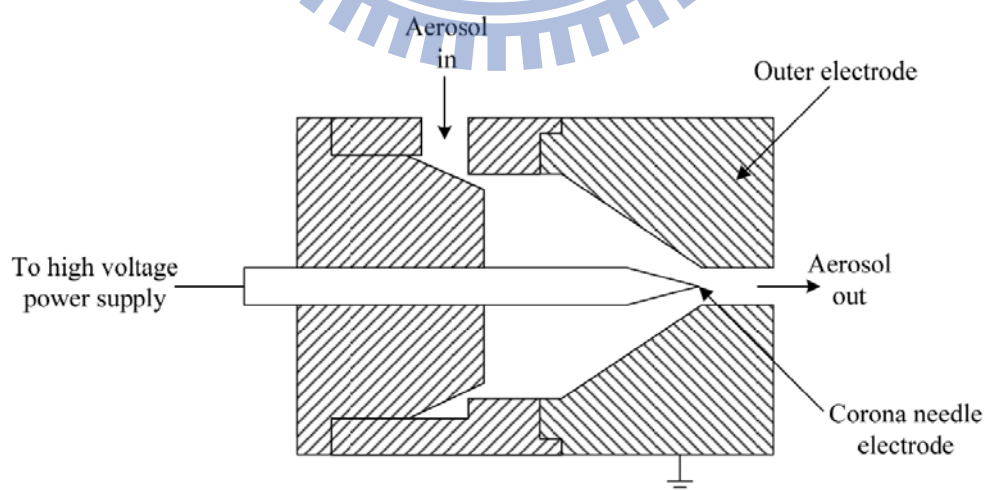
Figure 2.13 Schemataic diagram of the corona-needle unipolar charger developed by Alonso et al. (2006). (from Intra and Tippayawong 2009)

A corona-needle miniature unipolar charger for a personal particle sizer was proposed by Qi et al. (2008). As shown in Figure 2.14, the charger consisted of two major components. The outer included a radial inlet tube and axial outlet tube. The second was the corona discharge module, consisting of a pointed tungsten needle electrode placed coaxially in the outer tube capped with a perforate dome. The corona discharge module was installed in the case at the end opposite the axial exit tube. It was reported that the extrinsic charging efficiency of this charger was 4% for 5 nm particles.
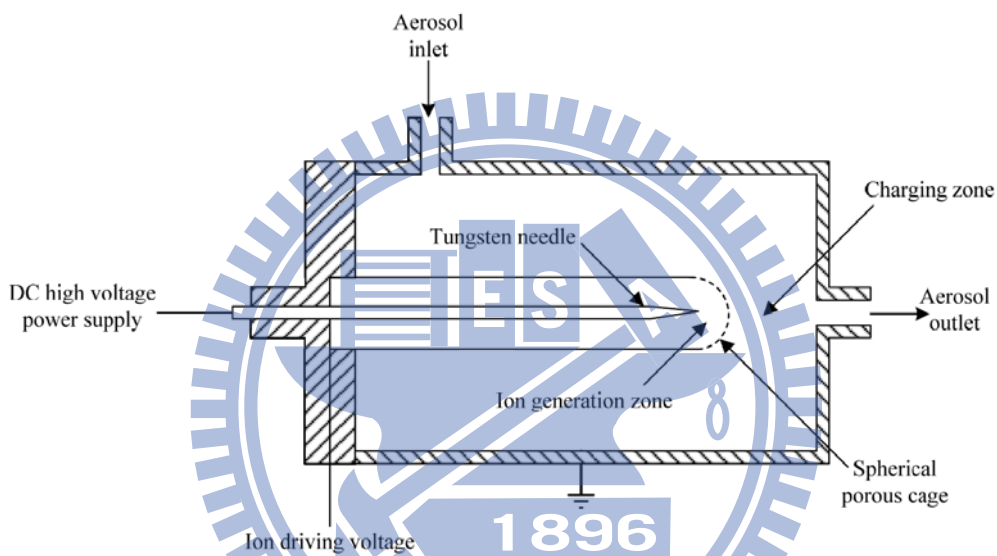
Figure 2.14 Schemataic diagram of the corona-needle unipolar charger developed by Qi et al. (2008). (from Intra and Tippayawong 2009)

Similar to the configuration of the charger of Qi et al. (2008), Li and Chen (2011) developed a corona-needle unipolar charger consisted of an outer metal case and a corona discharger tube module capped with a metal screen at one end, as shown in Figure 2.15. A pointed tungsten needle was used in the tube module to produce ions. The corona discharge tube module case was on the ion-driven voltage which was much lower than that applied to the needle. Ions produced in the tube module were driven through the metal screen by a weak electric field into the charging zone. The

geometrical arrangement of the tube module and the aerosol exit section allowed establishing the ion-driving field approximately in the longitudinal direction, which achieved the implementation of parallel electric and aerosol flow fields. The ion concentration in the charging zone can be controlled by varying the strength of the ion-driving field. It was reported that the extrinsic charging efficiency of this charger as high as about 8.8% for 5 nm particles.
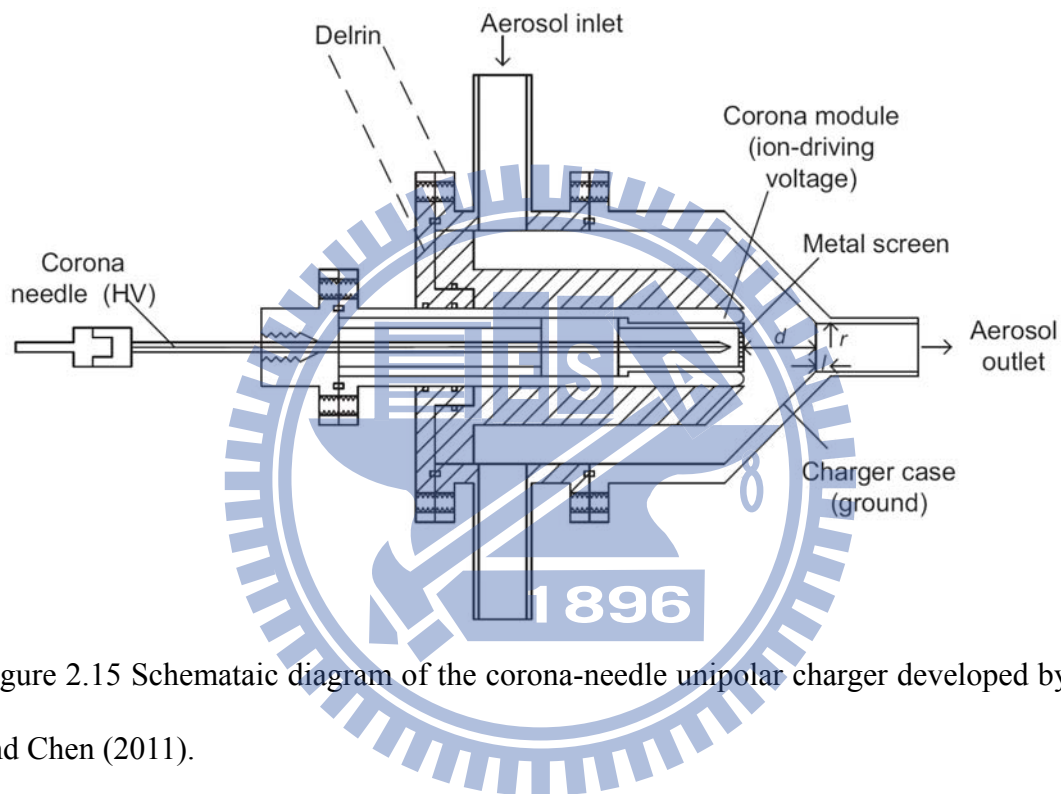
Figure 2.15 Schemataic diagram of the corona-needle unipolar charger developed by Li and Chen (2011).

Whitby (1961) first introduced the concept of applying a sonic jet flow to direct unipolar ions out from the corona discharge zone in the development of an ion generator. Medved et al. (2000) used a similar principle in the design of a unipolar charger, shown in Figure 2.16, which was later modified and used in the electrical aerosol detector (EAD, model 3070A, TSI Inc.) and nanoparticle surface area monitor (NSAM, model 3550, TSI Inc.). Ions were generated at a corona needle tip in a small ion-genetration chamber connected to a mixing chamber via an orifice. An air flow transferred the ions

into the mixing chamber and an opposing aerosol flow promoted mixing the aerosol and the ions. However, the issue of particle loss in ion-particle flow mixing was often encountered in the above chargers.
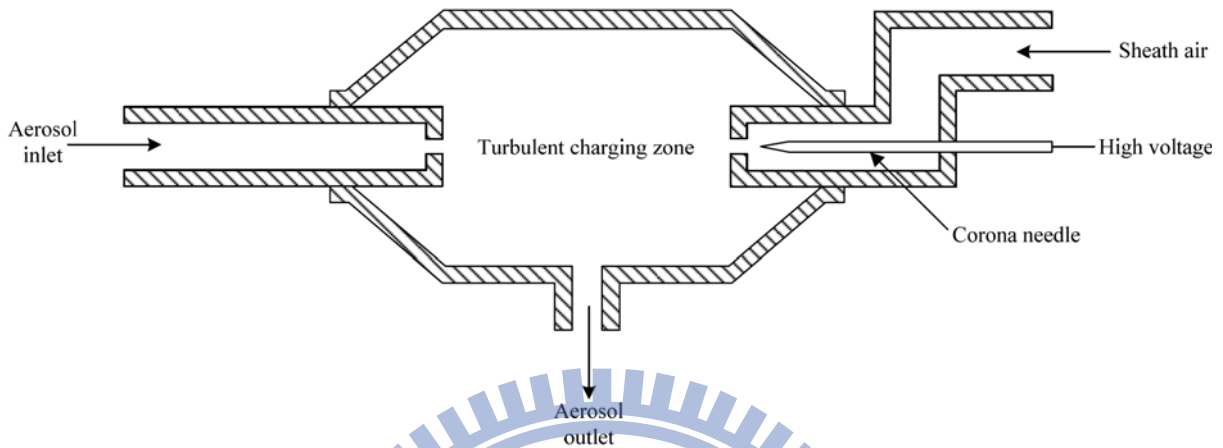
Figure 2.16 Schemataic diagram of the corona-needle unipolar charger developed by Medved et al. (2000). (from Intra and Tippayawong 2009)

With a careful flow mixing arrangement, Qi et al. (2007) developed a mixing-type unipolar charger consisted of completely separated corona ionization and charging chambers, as shown in Figure 2.17. Sonic-jet flow was also used to inject unipolar ions into the charging chamber. Instead of injecting ions perpendicular to or against the aerosol flow directions in the previous chargers of the same type (Medved et al., 2000; Marquard et al., 2006a), the charger injected sonic-jet flowed from each of the two ionizers into the charging zone at a 45° angle to the charger axis. The use of angular impingement of dual jet flows in the charger not only canceled the jet energy in the radial direction but also facilitated the exit of charged particles. The extrinsic charging efficiency of the charger of Qi et al. (2007) was reported as 5.7% for 4 nm particles. Recently, Kimoto et al. (2010) also developed a mixing-type unipolar charger, shown in Figure 2.18, consisted of a high-pressure corona ionizer to generate unipolar ions and a

small charging chamber (0.5 cm^3 volume) where the ions were mixed with nanoparticles without an external electric field at negative pressure. Up to now, the charger of Kimoto et al. (2010) showed the highest extrinsic charging efficiency among all existing corona-based unipolar chargers for particles smaller than 10 nm in diameter. The measured extrinsic charging efficiency was up to 59.7 % for 5 nm particles.
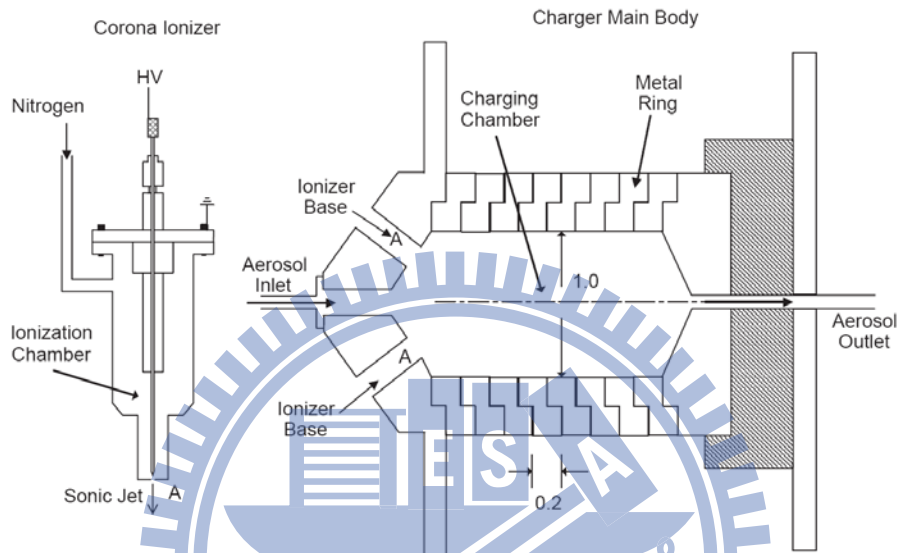
Figure 2.17 Schemataic diagram of the corona-needle unipolar charger developed by Qi et al. (2007).
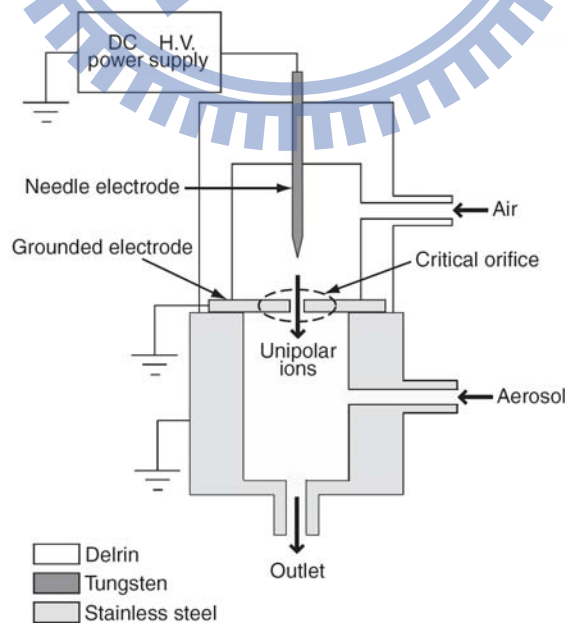
Figure 2.18 Schemataic diagram of the corona-needle unipolar charger developed by Kimoto et al. (2010).

2.2 Numerical studies of the corona unipolar chargers

Diffusion charging has been studied theoretically and various models are available. Detailed overview on the diffusion charging models in all aerosol regimes can be seen from the literature (Romay and Pui 1992a; Biskos et al. 2004; Marquard 2007). In the transition regime (Knudsen number $Kn \approx 1$), the birth-and-death charging model (Boisdron and Brock 1970) with the ion-particle combination coefficient estimated by Fuchs diffusion charging theory (Fuchs 1963) was used to predict the charge distribution for the unipolar charger, assuming $N_i t$ condition is given where N_i is the ion concentration (ions/m^3) and t is the charging time (sec) (Biskos et al. 2005b; Marquard et al. 2005; Qi et al. 2007, 2009; Vivas et al. 2008; Li and Chen 2011). The model assumes that ion concentration in the charging region is spatially uniform, considering neither the transport of ions and particles nor particle loss in the charger. These assumptions which are difficult to validate, especially for charging devices with complicated geometrical, electrical, and hydrodynamic conditions (Marquard et al. 2006b), could lead to inaccurate predictions. By considering the transport effects of ions and particles, some numerical models (Aliat et al. 2008, 2009; Alonso et al. 2009) were able to simulate unipolar diffusion charging based on Fuchs theory in a tube flow with the simple plug flow assumption for the flow field. However, the models are not applicable to other unipolar chargers with more complicated geometry. Huang and Alonso (2011) obtained particle trajectories through the combined mechanisms of diffusion and field charging to calculate nanoparticle electrostatic loss in the corona-needle unipolar charger for particles ranging from 3–30 nm in diameter. But the charging efficiency was not calculated. Kimoto et al. (2010) developed a theoretical model based on Fuchs theory to predict the extrinsic charging efficiency of an efficient small mixing-type unipolar charger. The measured charging efficiency for particles

smaller than 10 nm was much higher than the theoretical results due to the well-mixed flow assumption.

Table 2.1 and 2.2 summarize the charging performances and numerical studies of the above mentioned corona-based unipolar aerosol chargers, respectively. In summary, the charger performance depends on the extrinsic charging efficiency. An efficient unipolar charger should be further designed and developed for charging nanoparticles. In addition, an accurate numerical model which can be used to facilitate the design of an efficient unipolar nanoparticle charger and predict charging efficiency is needed to develop.
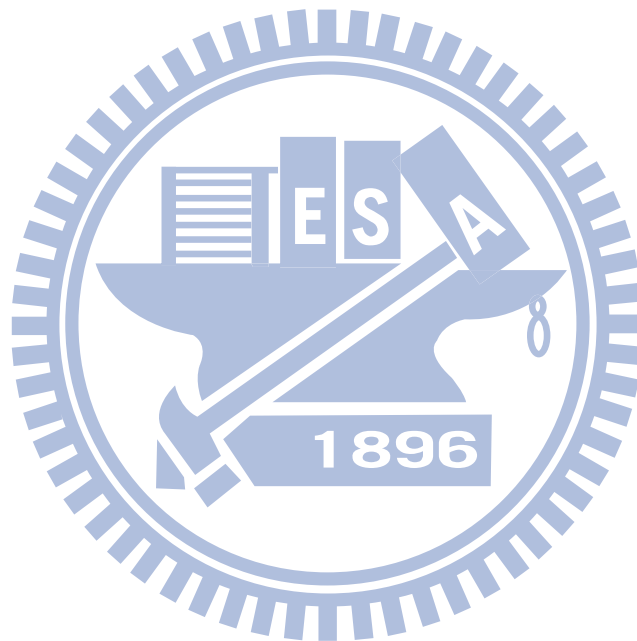
Table 2.1 Charging performances of corona-based unipolar aerosol chargers.

Investigator	Corona electrode	Sheath air	Ionized air flow	$N_i t$ product (s/m^3)	Charging efficiency
Hewitt (1957)	Wire	No	No	N.A.	N.A.
Liu and Pui (1975)	Wire	Yes	No	1.0×10^{13}	1.3% at 6 nm
Büscher et al. (1994)	Wire	Yes	No	1.1×10^{13}	4.0% at 5 nm
Cheng et al. (1997)	Wire	Yes	No	N.A.	N.A.
Kruis and Fissan (2001)	Wire	No	No	8.0×10^{13}	5% at 5 nm
Unger et al (2004)	Wire	No	No	N.A.	N.A.
Biskos et al. (2005a)	Wire	No	No	2.1×10^{13}	N.A.
Biskos et al. (2005b)	Wire	Yes	No	2.9×10^{13}	24.9% at 10 nm
Tsai et al. (2008)	Wire	Yes	No	5.4×10^{14}	10.6% at 10 nm
Tsai et al. (2010)	Wire	Yes	No	1.7×10^{15}	2.8% at 2.5 nm
Whitby (1961)	Needle	No	No	N.A.	N.A.
Medved et al. (2000)	Needle	No	Yes	N.A.	8% at 5 nm
Hernandez-Sierra et al. (2003)	Needle	No	No	N.A.	2.1% at 2.7 nm
Alonso et al. (2006)	Needle	No	No	3.7×10^{13}	1.8% at 3 nm
Marquard et al. (2006a)	Needle	No	Yes	N.A.	N.A.
Park et al. (2007)	Needle	No	Yes	N.A.	N.A.
Qi et al. (2007)	Needle	No	Yes	9.0×10^{12}	5.7% at 4 nm
Qi et al. (2008)	Needle	No	No	N.A.	4% at 5 nm
Kimoto et al. (2010)	Needle	No	Yes	4×10^{14}	59.7% at 5 nm
Li and Chen (2011)	Needle	No	No	1.1×10^{13}	8.8% at 5 nm

Table 2.2 Numerical studies of the corona-based unipolar aerosol chargers.

Researcher	Numerical method	Particle charging model	Assumption / Limit
Biskos et al. (2005b); Marquard et al. (2005); Qi et al. (2007, 2009); Vivas et al. (2008); Li and Chen (2011)	Birth-and-death charging model	Fuchs theory (1963)	The ion concentration in the charging region is spatially uniform.
Aliat et al. (2008, 2009); Alonso et al. (2009)	Eulerian method	Fuchs theory (1963)	Simple plug flow for the flow field in the charger.
Kimoto et al. (2010)	Lagrangian method	Fuchs theory (1963)	Complete mixing of particles with ions in the charging chamber.
Huang and Alonso (2011)	Lagrangian method	Combined charging model	The charging efficiency is not available.

CHAPTER 3
METHODS

3.1 Experimental method

3.1.1 Design of unipolar charger with axial sheath air

Figure 3.1 shows the schematic diagram of the unipolar charger with axial sheath air which is a modification of the nanoparticle charger with multiple discharging wires developed by Tsai et al. (2010). The charger consists of a gold wire of 50 μm in diameter and 2 mm in length as the discharge electrode, on which a high D.C. voltage is applied from the top of the charger. The outer stainless steel cylindrical casing of 30 mm in diameter is grounded. The space between the gold wire and the stainless steel casing is the charging zone where aerosol charging takes place. The aerosol flow was introduced into the charger from the bottom and a filtered high-speed sheath air flow with the velocity of 0.9–7.1 m/s was introduced from an annular slit of 0.1 mm gap formed by the Teflon shroud and the outer casing to minimize charged particle loss. The charged particles were accelerated to exit the charger quickly through another annular slit of 0.1 mm gap after the charging zone.

Ø 30

57

Gold wire

Aerosol out

Sheath air

Stainless steel

Teflon

Copper
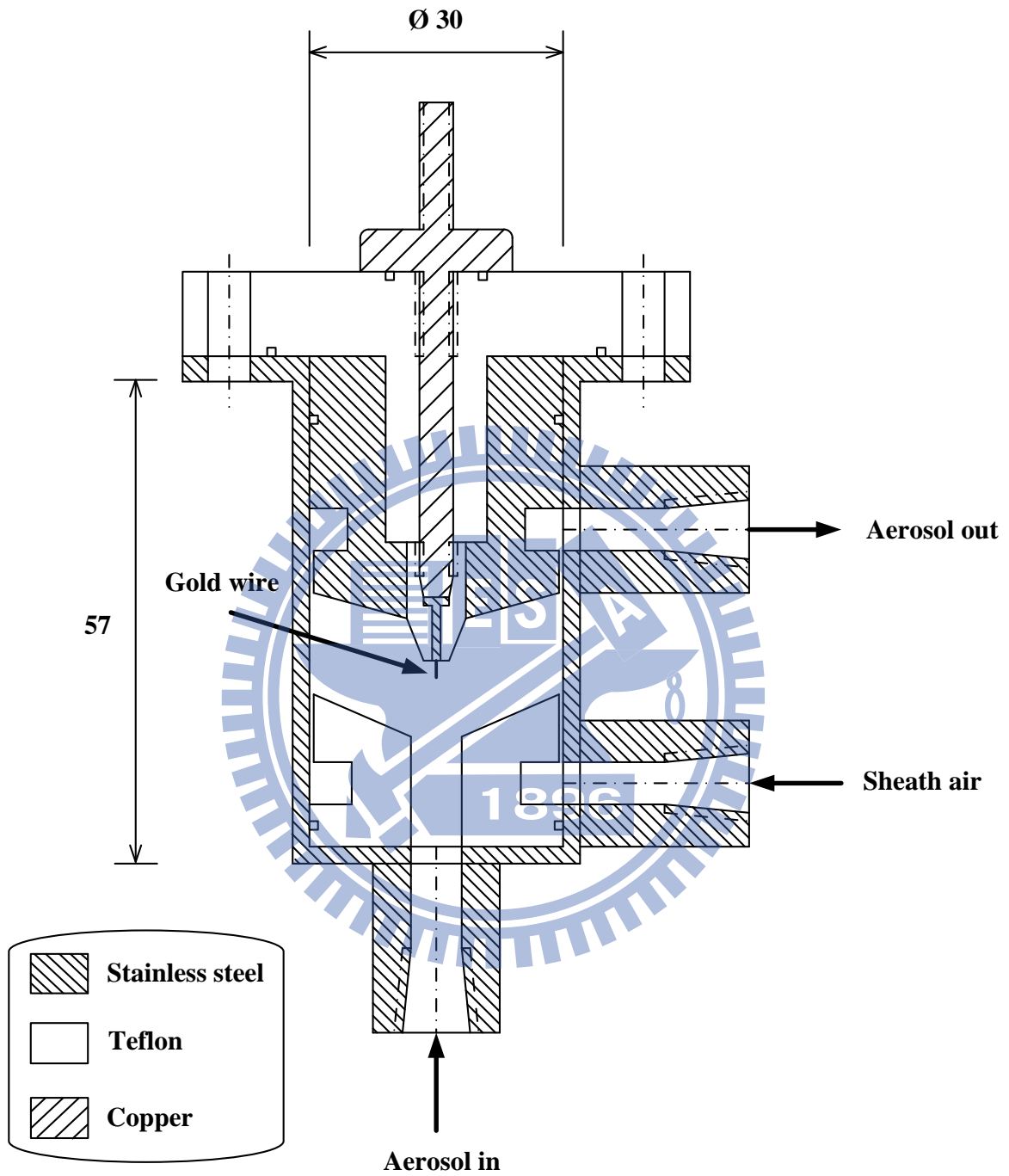
Aerosol in

Figure 3.1 Schematic diagram of the charger with axial sheath air (unit: mm).

3.1.2 Experimental setup

The experimental setup consisted of the aerosol generation section and performance evaluation section for measuring the charging efficiency and particle loss in the charger is shown in Figure 3.2 and similar to that described in Tsai et al. (2010). In the aerosol generation section, monodisperse Ag particles ranging from 2.5 to 20 nm in diameter were generated by the evaporation-condensation technique (Scheibel & Porstendorfer, 1983). First, silver powder was loaded in a ceramic boat placed in a tube furnace (Sunrise Co. Ltd., New Taipei City, Taiwan). Generated vapor was carried by clean air out of the furnace where polydisperse nanoparticles of high concentration were produced by quenching the hot vapor in a water-based cooler. The particles were neutralized by a TSI 3077A electrostatic charge neutralizer before being introduced into a Nano-DMA for classifying monodisperse test particles. Singly charged monodisperse particles were then neutralized and passed through a wire-in-tube electrostatic precipitator to remove all charged particles, allowing only uncharged particles to enter the unipolar charger for the charging efficiency experiments (performance evaluation section).

To generate the electric field and corona ions, high positive/negative voltage was supplied to the corona wire using a high-voltage D.C. power supplier (model SL P150/SL N30, Spellman High Voltage Electronic Corporation, NY, USA). The grounded stainless steel casing was connected to a picoammeter (model 6485, Keithley Instruments Inc., Cleveland, OH, USA) for measuring the corona current. The high-speed sheath air from the annular slit near the casing wall helped accelerate charged particles exit the charger. After charged aerosol flow to exit the charger, it passed through the second ESP for removing charged particles if the voltage was turned on. An ultrafine condensation particle counter (UCPC, model 3786, TSI Inc.) was used

to measure particle concentration downstream after the second ESP. For the experiment involving the measurement of particle charge distribution at the exit of the charger, the tandem-DMA method was used to measure the charge distribution of monodisperse particles of different sizes (Tsai et al. 2010).

Both particle charging efficiency and particle loss were measured at the sheath air flow rates (Q_{sh}) from 0.5 to 4 L/min while the aerosol flow (Q_a) was fixed at 1 L/min. There are four parameters used for the performance evaluation of unipolar electrical aerosol chargers (Marquard et al. 2006b), including intrinsic charging efficiency (η_{int}), extrinsic charging efficiency (η_{ext}), electrostatic loss (L_{el}), and diffusion loss (L_d^0). The superscript "0" represents uncharged particles. The intrinsic charging efficiency, which is defined as the fraction of initial uncharged particles acquiring charge inside the charger regardless of charged particle loss, can be calculated as (Tsai et al. 2010):

$$\eta_{int} = \frac{f}{P_{ESP}} \frac{C_{out,OFF} - C_{out}^0}{C_{in}} \tag{3.1}$$

where the dilution factor f is equal to the ratio of the total outlet aerosol flow rate to that at the inlet of the charger, P_{ESP} is the penetration of uncharged particles through the second ESP, C_{in} is the particle number concentration (particles/m³) measured upstream of the charger, $C_{out,OFF}$ is the particle number concentration measured downstream of the second ESP when no voltage is applied on the charger and the second ESP, and C_{out}^0 is the particle number concentration measured downstream of the charger when the charger is on and sufficiently high voltage is applied on the second ESP to remove all charged particles.

The extrinsic charging efficiency is defined as the fraction of particles exiting the

charger which carries at least one elementary unit of charge:

$$\eta_{ext} = \frac{f}{P_{ESP}} \frac{C_{out,ON} - C_{out}^0}{C_{in}}$$ (3.2)

where $C_{out,ON}$ is the particle number concentration measured downstream of the charger when the charger is on and the second ESP is off.

Experimental particle electrostatic loss, L_{el}, and diffusion loss, L_d^0, inside the charger can be calculated as

$$L_{el} = \frac{f}{P_{ESP}} \frac{C_{out,OFF} - C_{out,ON}}{C_{in}}$$ (3.3)

$$L_d^0 = 1 - \frac{f}{P_{ESP}} \frac{C_{out,OFF}}{C_{in}}$$ (3.4)
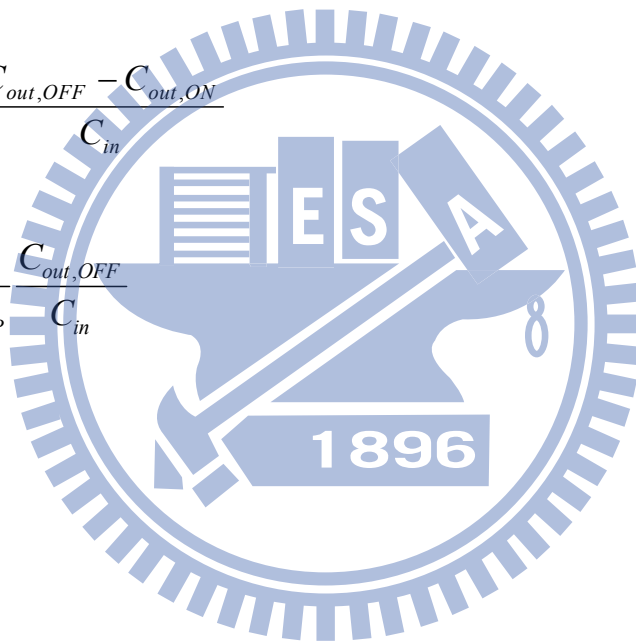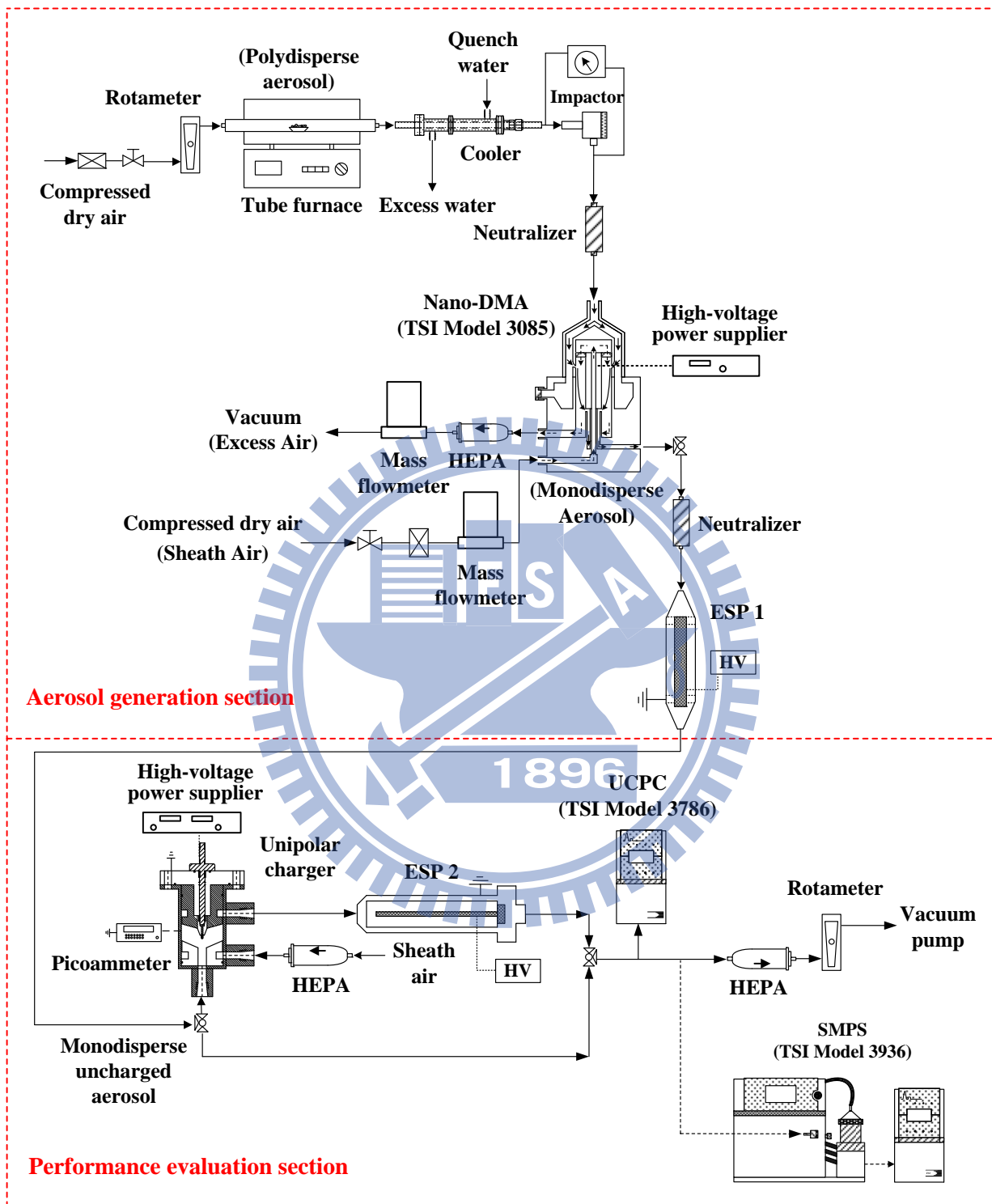
Figure 3.2 Schematic diagram of the experimental setup.

3.2 Numerical method

3.2.1 Flow field

A 2-D numerical simulation was conducted in this study. The calculation domain of 35 mm in length and 15 mm in width is shown in Figure 3.3, in which the hatched areas represent the solid region. The gap between the charger body and the wall is 0.1 mm for both sheath air and exiting aerosol flows.

The laminar flow field model was used since the maximum flow Reynolds number based on the hydrodynamic diameter is 235.8, which is much smaller than 2000. The flow field in the charger was simulated by solving the following 2-D Navier-Stokes equations and continuity equation in the cylindrical coordinates:

$$\rho_{air}\left(u_r\frac{\partial u_r}{\partial r}+u_z\frac{\partial u_r}{\partial z}\right)=-\frac{\partial P}{\partial r}+\mu_{air}\left[\frac{1}{r}\frac{\partial}{\partial r}\left(r\frac{\partial u_r}{\partial r}\right)+\frac{\partial^2 u_r}{\partial z^2}\right]-\frac{\mu_{air}u_r}{r^2} \tag{3.5}$$

$$\rho_{air}\left(u_r\frac{\partial u_z}{\partial r}+u_z\frac{\partial u_z}{\partial z}\right)=-\frac{\partial P}{\partial z}+\mu_{air}\left[\frac{1}{r}\frac{\partial}{\partial r}\left(r\frac{\partial u_z}{\partial r}\right)+\frac{\partial^2 u_z}{\partial z^2}\right] \tag{3.6}$$

$$\frac{1}{r}\frac{\partial}{\partial r}\left(ru_r\right)+\frac{\partial u_z}{\partial z}=0 \tag{3.7}$$

where u_r and u_z is the air velocity in r and z direction (m/s), respectively, ρ_{air} is the air density (kg/m^3), P is the pressure (Pa), and μ_{air} is the air viscosity (kg/m·s). The governing equations were discretized using the finite volume method and solved by the SIMPLER algorithm (Semi-Implicit Method for Pressure Linked Equations) (Patankar 1980). When dealing with the boundary at the inclined wall surface, the concept of blocked-off region was applied to divide the control volumes into active and inactive regions, the later of which represent solid regions. At the inlets of aerosol and sheath flows, the boundary conditions for the calculation of flow field were assigned based on

the experimental values. The outflow velocity at the exit of the charger was calculated based on the continuity equation.

A total of 49,600 (248 in r–direction $\times$ 200 in z–direction) non-uniform rectangular grids were used in the calculation domain. The average grid size was about 60.5 and 175 μm in r (radial) and z (axial) direction, respectively, while the smallest size of 0.54 and 1.34 μm was assigned near the wire and the wall surfaces, respectively. The shape of the wire tip was flat. In the test run, the number of grids was either 12,400 (124 $\times$ 100), 49,600 (248 $\times$ 200) or 198,400 (496 $\times$ 400). As the number of grids was increased from 12,400 to 49,600 or 198,400, the accuracy for the numerical diffusion loss of 5 nm particles at $Q_{sh} = 3$ L/min was also changed from 20.1% to 18.6% or 18.4%. With the number of grids of 49,600 and the computation time for the flow field of about 3 hours, the calculated diffusion loss of 5 nm particles at $Q_{sh} = 3$ L/min was found to be close to the experimental data of 17.9%. Further increase in the number of grids to 198,400, the diffusion loss only changed by about 0.2 % but the computation time for the flow field was increased to about 48 hours. Therefore, 49,600 grids were used in the simulation. The total number of iterations to reach convergence was about 10,000 for solving the flow field.
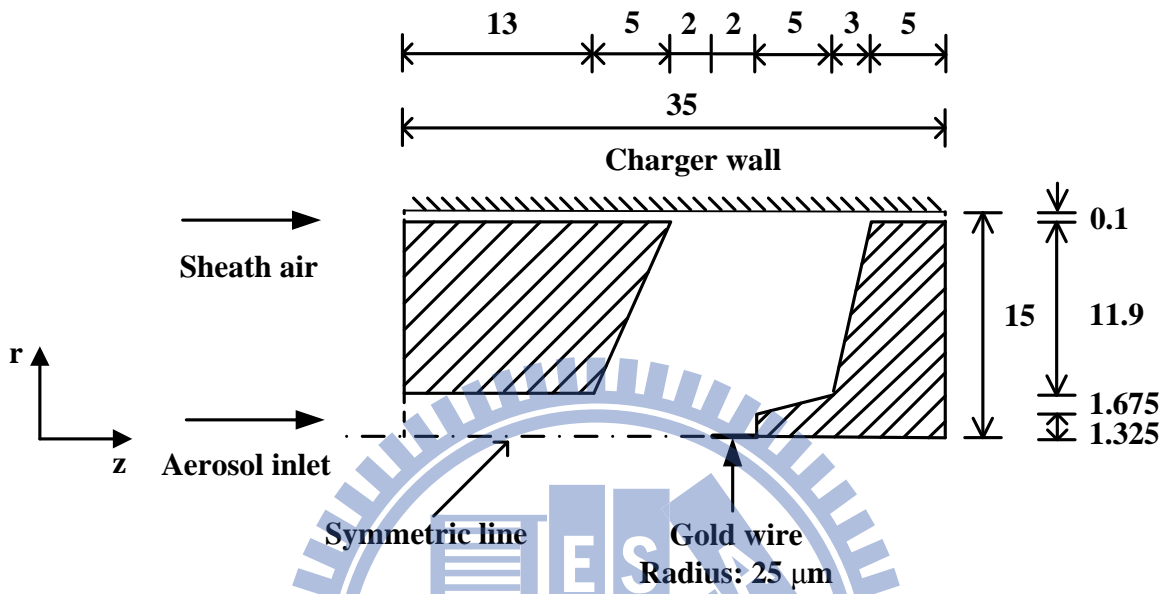
Figure 3.3 Calculation domain in the numerical simulation of the charger with axial sheath air (unit: mm).

3.2.2 Electric potential and ion concentration fields

The present methods for calculating corona discharge and ion concentration field were based on the work of Lin and Tsai (2010). The governing equation, Poisson's equation, for the electric potential field in the charger can be written as

$$\frac{1}{r}\frac{\partial}{\partial r}\left(r\frac{\partial V}{\partial r}\right)+\frac{\partial^2 V}{\partial z^2}=-\frac{\rho_i}{\varepsilon_0} \tag{3.8}$$

where V is the electric potential (Volt), ρ_i is the space charge density (C/m^3), and ε_0 is the permittivity of air (A·s/Volt·m).

The space charge density, ρ_i, in Equation (3.8) was calculated by the following convection-diffusion equation as

$$\frac{\partial(u_r\rho_i+E_r Z_i\rho_i)}{\partial r}+\frac{\partial(u_z\rho_i+E_z Z_i\rho_i)}{\partial z}=D_i\left[\frac{1}{r}\frac{\partial}{\partial r}\left(r\frac{\partial\rho_i}{\partial r}\right)+\frac{\partial^2\rho_i}{\partial z^2}\right] \tag{3.9}$$

where D_i is the ion diffusion coefficient (m^2/s), Z_i is the ion mobility (m^2/s·V), E_r and E_z are the local electric field strengths in r and z direction (Volt/m), respectively, which can be calculated as

$$-\frac{\partial V}{\partial r}=E_r \tag{3.10}$$

$$-\frac{\partial V}{\partial z}=E_z \tag{3.11}$$

In Equation (3.8), ion quenching by particles was neglected because the predicted ion concentration was much higher than the particle number concentration in this study. For example, when the applied voltage was +2.1 and -2.1 kV, the average ion number concentration was calculated to be 9.0×10^{14} and 9.3×10^{14} ions/m^3, respectively,

which was five orders of magnitude higher than the measured particle concentration. In Equation (3.9), the source term of the corona current generated by charged particles was neglected either. For the ion mobility, a value of 1.15×10^{-4} m^2/s·V for positive ions and 1.35×10^{-4} m^2/s·V for negative ions as suggested by Lin and Tsai (2010) was used in the simulation. To solve Equations (3.8) and (3.9), the ion density, $\rho_{i,0}$, at the discharge wire surface was calculated by the following equation:

$$\rho_{i,0} = \frac{I}{2\pi r_w E_w Z_i}$$
(3.12)

where I is the corona current (A) and r_w is the radius of the discharge wire (m). The boundary condition at the wire surface followed the work of Aliat et al. (2009), in which the electric field on the corona wire surface, E_w, was assumed to be constant (Kaptzov 1947) and the value was calculated from the following formula (Peek 1929):

$$E_w = 30\delta\left[1 + \frac{0.3}{(\delta r_w)^{1/2}}\right]$$
(3.13)

where E_w is in kV/cm, r_w is in cm, and $\delta\,(=T_0 P/T P_0)$ is the relative density of the air, in which $T_0\,(=298\ K)$ and $P_0\,(=1\ atm)$ is the reference temperature and pressure, respectively.

3.2.3 Charged particle concentration field and particle charging efficiency

The governing equation for the concentration of particles carrying q elementary charges, $N_{p,q}$, is

$$\frac{\partial(u_r N_{p,q} + E_r Z_p N_{p,q})}{\partial r} + \frac{\partial(u_z N_{p,q} + E_z Z_p N_{p,q})}{\partial z} = D_B \left[\frac{1}{r} \frac{\partial}{\partial r} \left(r \frac{\partial N_{p,q}}{\partial r} \right) + \frac{\partial^2 N_{p,q}}{\partial z^2} \right] + S_c + S_p$$

(3.14)

where Z_P is the particle electrical mobility (m^2/s·V), which is defined by

$Z_p = qeC_c / 3\pi\mu_{air}d_p$, q is the number of elementary units of charge, e is the elementary

charge (1.6×10^{-19} C), C_c is the slip correction factor, D_B is the Brownian diffusion

coefficient for particles (m^2/s), and S_c is the source term, which represents the

generation of particles with q elementary charges. In equation (3.10), the boundary

condition at the charger wall was assumed to be perfect absorption. The source term S_c

and sink term S_p are given by (Adachi et al. 1985; Aliat et al. 2009)

$$S_c = \alpha_{q-1} N_{p,q-1} N_i$$

(3.15)

$$S_p = -\alpha_q N_{p,q} N_i$$

(3.16)

where α_q is the combination coefficient of ions for particles carrying q elementary

charges (m^3/s) and can be calculated as (Fuchs 1963)

$$\alpha_q = \frac{\pi \overline{c}_i \xi \delta_r^2 \exp\left(\frac{-\phi(\delta_r)}{k_b T} \right)}{1 + \exp\left(\frac{-\phi(\delta_r)}{k_b T} \right) \frac{\overline{c}_i \xi \delta_r^2}{4 D_i a} \int_0^{a/\delta_r} \exp\left(\frac{\phi(a/x)}{k_b T} \right) dx}$$

(3.17)

where $\overline{c}_i$ is the mean thermal velocity of ions (m/s), δ_r is the radius of the limiting

sphere (m), ξ is the striking probability, k_b is the Boltzmann's constant (J/K), ϕ is the

electric potential between the particle and the ion (Volt) (Adachi et al. 1985), and a is

the radius of particles (m). The ξ values shown in Table 1 of Hoppel and Frick (1986)

were adopted to calculate the ion-particle combination coefficients. The parameters used in Equation (3.17) can be calculated as follows:

$$x = a/r \tag{3.18}$$

$$\phi(r) = \int_r^\infty F(r)dr = \frac{e^2}{4\pi\varepsilon_0}\left[\frac{q}{r} - \frac{\varepsilon_p - 1}{\varepsilon_p + 1}\frac{a^3}{r^2 - a^2}\right] \tag{3.19}$$

$$\delta_r = \frac{a^3}{\lambda_i^2}\left[\frac{1}{5}\left(1 + \frac{\lambda_i}{a}\right)^5 - \frac{1}{3}\left(1 + \frac{\lambda_i^2}{a^2}\right)\left(1 + \frac{\lambda_i}{a}\right)^3 + \frac{2}{15}\left(1 + \frac{\lambda_i^2}{a^2}\right)^{5/2}\right] \tag{3.20}$$

$$\xi = \left[\frac{r_a^2\left(1 + \frac{2}{3k_bT}(\phi(\delta_r) - \phi(r_a))\right)}{\delta_r}\right]^2 \tag{3.21}$$

$$D_i = \frac{k_bTZ_i}{e} \tag{3.22}$$

$$\bar{c}_i = \sqrt{\frac{8k_bT}{\pi(M_i/N_a)}} \tag{3.23}$$

$$\lambda_i = 1.329\frac{Z_i}{e}\sqrt{\frac{k_bTM_iM_{air}}{(M_i + M_{air})N_a}} \tag{3.24}$$

where r is the distance between particles and ions center (m), ε_p is the dielectric constant of particles (for Ag, $\varepsilon_p = \infty$), λ_i is the mean free path of ions (m), r_a is the apsoidal distance (m), M_i is the molecular weight of ions (kg/mol), M_{air} is the molecular weight of air (kg/mol), and N_a is the Avogadro number (6.023×10^{23} #/mol).

The theory of Marlow and Brock (1975), which was found to be more appropriate

than Fuchs theory for predicting particle charging for particles with $d_p \leq 20$ nm (Pui et al. 1988; Romay and Pui 1992a; Lin and Tsai 2010), was applied to predict the charging efficiency in the present simulation. The combination coefficient between an ion and an uncharged particle, α_0, was calculated as

$$\alpha_0 = \frac{\pi a^2 \overline{c}_i \left[1 + \sqrt{\pi h}\right]}{1 + \left[\lambda_d G_{IN} / 1 + \sqrt{\pi h}\right]} \tag{3.25}$$

where

$$h = \frac{\varepsilon_p - 1}{\varepsilon_p + 1} \frac{e^2}{2ak_bT} \tag{3.26}$$

$$\lambda_d = \sqrt{\pi}(a/\lambda_i)(\frac{M_i + M_{air}}{M_i}) \tag{3.27}$$

In Equation (3.25), G_{IN} is the first iteration correction to the flux, which was calculated to be 0.26 (Marlow and Brock 1975).

The charging theory of Fuchs (1963) requires five ion properties including the mobility, molecular weight, diffusion coefficient, mean thermal velocity, and mean free path to calculate the combination coefficient of ions for particles. Only two of these five properties are independent. The ion mobility and molecular weight are used to derive the other three properties (Romay and Pui 1992a). A wide range of the values of the ion mobility and molecular weight in the aerosol charging literature summarized in Table 1 of Lin and Tsai (2010) is a constraint for the use of the present model. Moreover, at the negative applied voltage charging contribution from electrons was ignored in the simulation because of their lower concentration than negative ions. Some researchers speculated that electrons might play an important role in the negative charging for

nanoparticles because of high combination coefficient as compared with that of negative ions (Romay and Pui 1992b; Marquard et al. 2007; Aliat et al. 2008, 2009). However, this issue remains to be studied when the theory of Marlow and Brock (1975) is considered for particles with $d_p \leq 20$ nm.

Equations (3.8), (3.9), and (3.14) were also discretized by using the finite volume method and solved by the same computer code used in the flow field simulation. The extrinsic charging efficiency, electrostatic loss, and convection-diffusion loss ($L_{con-dif}^{c}$) of charged particles in the charger were then calculated as (Marquard et al. 2006b):

$$\eta_{ext} = \frac{N_{out}^{c}}{N_{in}} \tag{3.28}$$

$$L_{el} = \frac{N_{el}}{N_{in}} \tag{3.29}$$

$$L_{con-dif}^{c} = \frac{N_{con-dif}^{c}}{N_{in}} \tag{3.30}$$

where N_{in}, N_{out}^{c}, N_{el}, and $N_{con-dif}^{c}$ are the rate of uncharged particles entering the inlet of the charger, the rate of charged particles exiting the charger, electrostatic deposition rate of charged particles, and convection-diffusion deposition rate of charged particles (number of particles/s), respectively. From the above equations, the simulated intrinsic charging efficiency can be calculated as follows:

$$\eta_{int} = \frac{N_{out}^{c} + N_{el} + N_{con-dif}^{c}}{N_{in}} = \eta_{ext} + L_{el} + L_{con-dif}^{c} \tag{3.31}$$

In the above equations, the superscript "c" in the variables represents charged particles.

CHAPTER 4

RESULTS AND DISCUSSION

4.1 Experimental results for the charging efficiency of the charger with axial sheath air

4.1.1 Characteristics of the V-I curve

Figure 4.1 shows the corona current as a function of applied voltage in the charger with axial sheath air. The corona current varies from 0.001 to 1.817 and -0.004 to -2.087 µA at the applied voltage of +1.6 to + 2.4 and -1.6 to -2.4 kV, respectively. For an aerosol charger based on the ion attachment technique, the $N_i\,t$ product is the key parameter when the charging mechanism is dominated by ion diffusion. A greater $N_i\,t$ product will lead to higher intrinsic charging efficiency. Numerical results show that the maximum ion concentration occurs at the discharge wire surface, which ranged $1.10 \times 10^{13} \sim 1.49 \times 10^{16}$ ions/m^3 at the positive applied voltage of +1.6 ~ +2.4 kV and $3.04 \times 10^{13} \sim 1.47 \times 10^{16}$ ions/m^3 at the negative applied voltage of -1.6 ~ -2.4 kV, respectively. The average charging time in the charging zone is calculated to be 0.222 to 0.067 sec when the sheath air flow rate varies from 0.5 to 4 L/min at the fixed aerosol flow rate of 1 L/min. Therefore, both sheath air flow rate and applied voltage will influence the intrinsic charging efficiency. A smaller flow rate and higher applied voltage will lead to a higher $N_i\,t$ product and hence a higher intrinsic charging efficiency. But for the extrinsic charging efficiency, the loss of charged particles inside the charger also has to be considered.
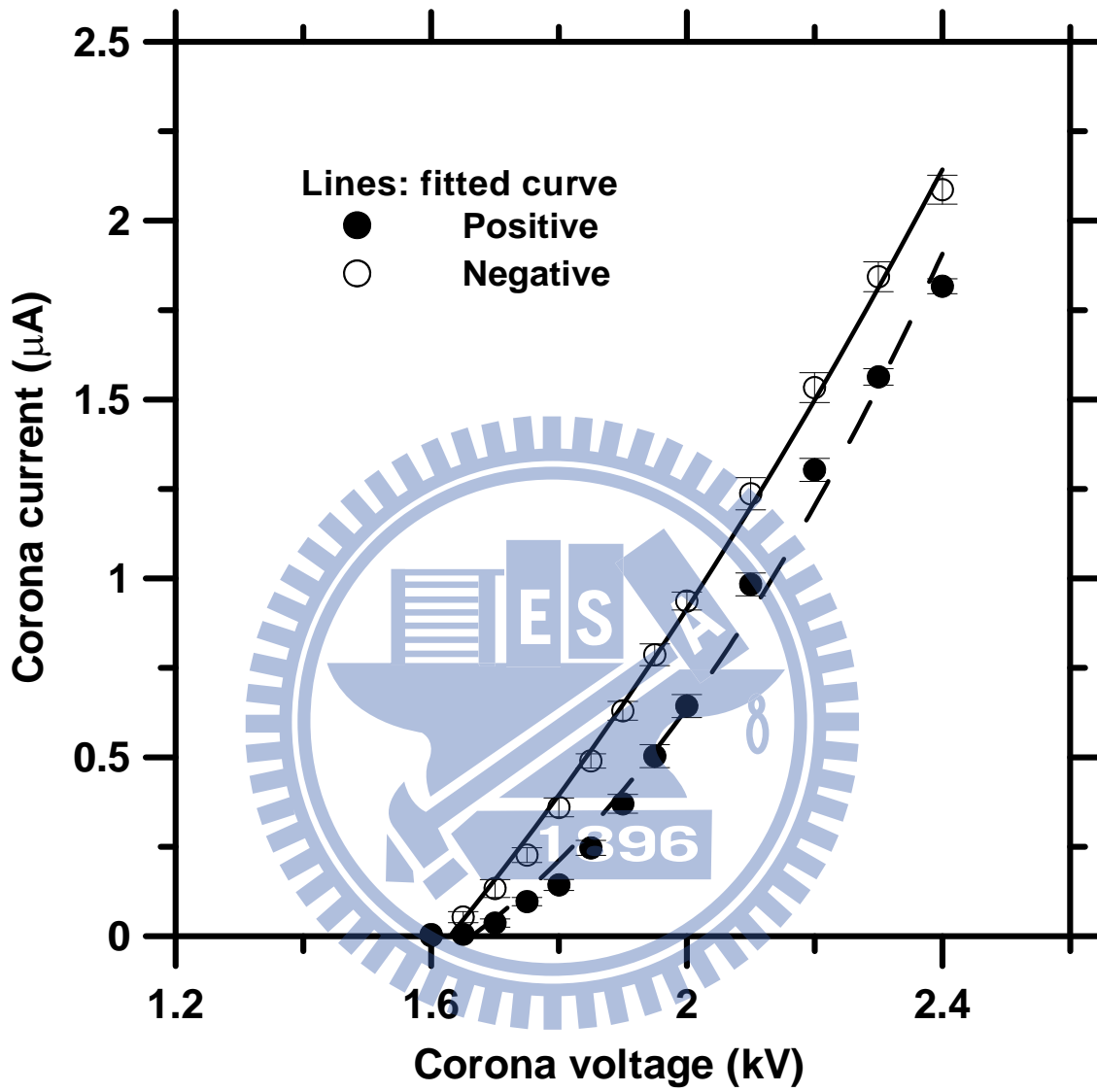
Figure 4.1 Corona current versus applied voltage.

4.1.2 Effect of sheath air flow rate

The effect of the sheath air flow rate on the extrinsic charging efficiency was obtained experimentally. Figure 4.2a shows the experimental extrinsic charging efficiency of 20 nm particles as a function of corona voltage and sheath air flow rate. At all sheath air flow rates, there is a corresponding maximum extrinsic charging efficiency occurs at +1.8kV. In general, the extrinsic charging efficiency of 20 nm particles increases with increasing sheath air flow rate from 0.5 to 3 L/min due to a decrease in the charging time and the reduction of charged particle loss. For example, at the applied voltage of +1.8 kV, the extrinsic charging efficiency of 20 nm particles increases from 61.2% to 71.1% when Q_{sh} is increased from 0.5 to 3 L/min. However, further increase of Q_{sh} from 3 to 4 L/min does not increase the extrinsic charging efficiency any further. For example, at +1.8 kV, the extrinsic charging efficiency is 70.1% at Q_{sh} = 4 L/min, which is very close to 71.1% at Q_{sh} = 3 L/min. As also shown in Figure 4.2b, the electrostatic loss of 20 nm charged particles is decreased with an increasing Q_{sh} from 0.5 to 3 L/min at the applied voltage from +1.7 to +2.2 kV. The electrostatic loss in the charger is effectively reduced at Q_{sh} = 3 L/min, but does not change very much when Q_{sh} is increased to 4 L/min. However, by increasing Q_{sh} to 4 L/min, electrostatic loss does not decrease further for the applied voltage below +1.9 kV. The loss is increased instead when the applied voltage is greater than +1.9 kV. The highest extrinsic charging efficiency for 20 nm particles is thus obtained at 3 L/min.

The maximum extrinsic charging efficiency of the charger with axial sheath air operating at Q_{sh} = 3 L/min is compared with that of the previous corona-based chargers and shown in Figure 4.3. The best extrinsic charging efficiency of the charger with axial sheath air is 3.1%–71.1% (d_p = 2.5–20 nm) at the positive applied voltages of +1.8 to

+2.1 kV, and 14.7%–66.4% (d_p = 5–20 nm) at the negative applied voltages of -1.8 to

-2.1 kV. The extrinsic charging efficiency of the charger with axial sheath air is seen to

be higher than that of other corona-based unipolar chargers, but lower than that of

Kimoto et al. (2010) for particles smaller than 10 nm in diameter. The charger

developed by Kimoto et al. (2010) consisted of a high-pressure corona ionizer to

generate unipolar ions and a small charging chamber (0.5 cm^3 volume) where the ions

were mixed with nanoparticles without an external electric field.
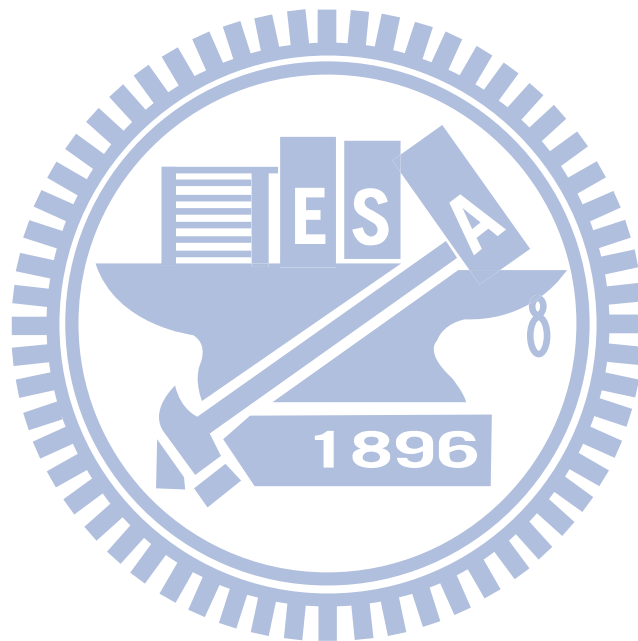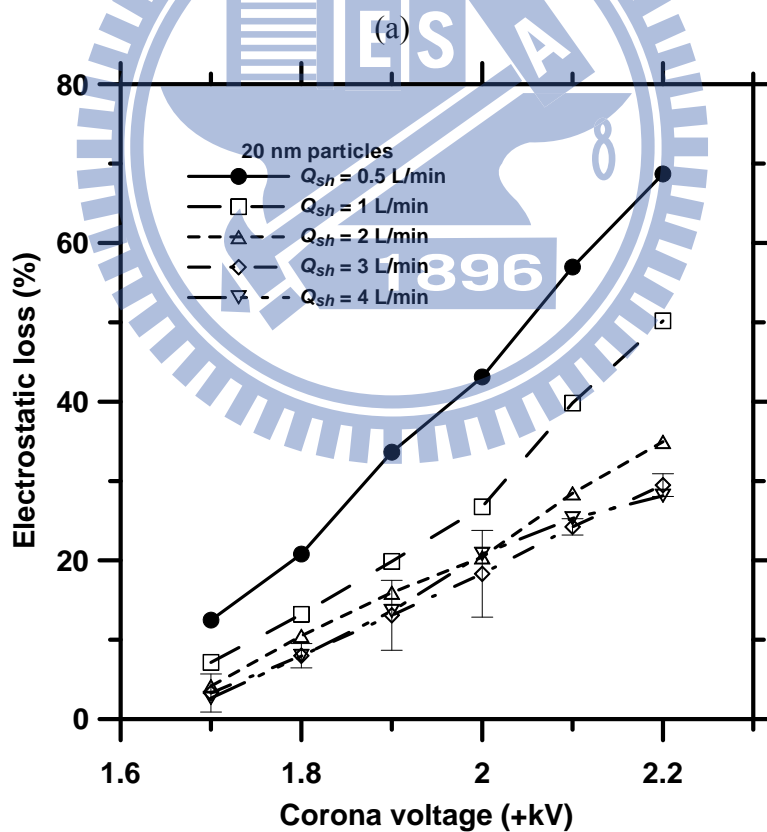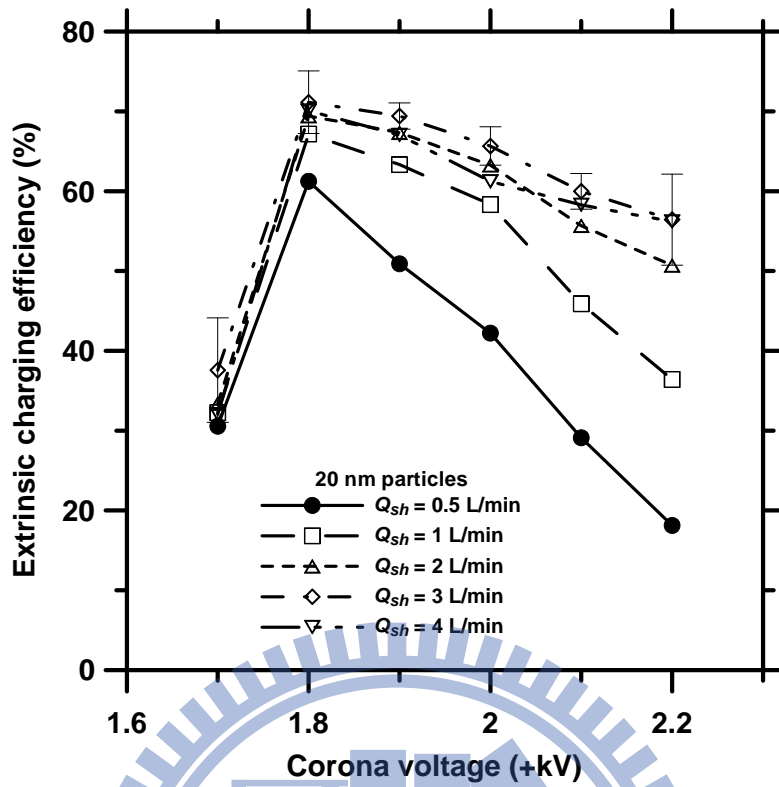
Figure 4.2 (a) Experimental extrinsic charging efficiency and (b) electrostatic loss of 20

nm particles versus corona voltage at different sheath air flow rates.
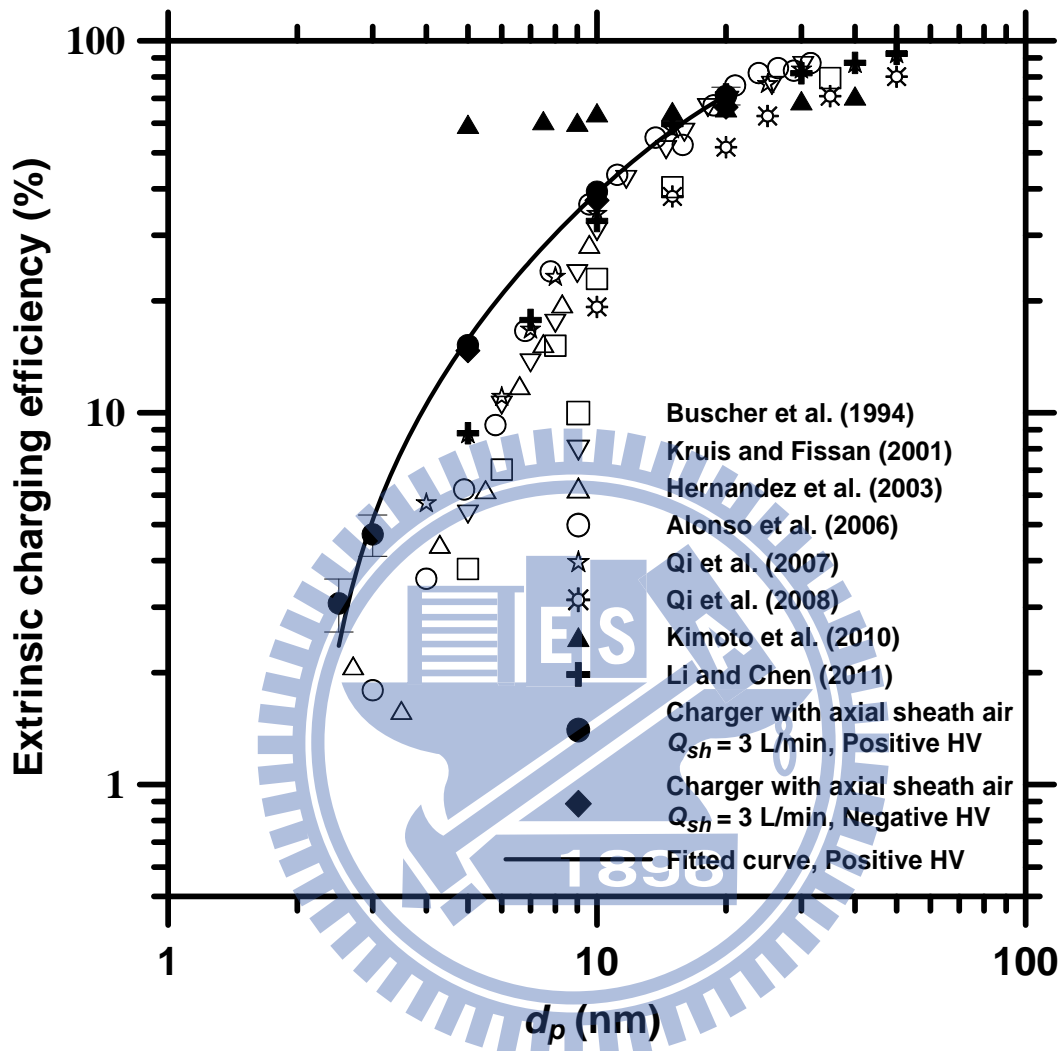
Figure 4.3 Comparison of the experimental extrinsic charging efficiency of the charger with axial sheath air with that of previous corona-based chargers.

4.2 Numerical results for the charging efficiency of the charger with axial sheath air

4.2.1 Flow streamlines, electric potential, ion concentration, and charged particle concentration fields

The flow, electric potential and ion concentration fields were calculated first before the charged particle concentration could be calculated. An example of the calculated flow filed (plotted as flow streamlines), electric potential, and ion number concentration fields is shown in Figure 4.4 for the charger with axial sheath air at Q_{sh} = 3 L/min and at the applied voltage of -2.1 kV. Figure 4.4a shows two main flow recirculation regions exist in charging zone of the charger, which have a great influence on the spatial distribution of charged particles as will be shown later. Both calculated electric potential and ion concentration are seen to be the highest near the wire but decay very rapidly away from the wire. The equipotential lines are also seen to be close to each other near the wire where the electric field is the strongest. Without considering the transport effect of flow field, ions and charged particles will move along the electric field lines, which are perpendicular to the equipotential lines in the charger, and then attach to the charger wall. The ion number concentration is the maximum at the wire surface, which is 8.7×10^{15} ions/m^3 at the axial distance of 0.02 ~ 0.022 m and decays to about 2.5×10^{15} ions/m^3 at the radial distance of 0.003 m and 3.4×10^{14} ions/m^3 near the wall at the same axial position.

Based on the flow, electric potential and ion concentration fields, the spatial distribution of charged particles in the charger was calculated. An example is shown for 20 nm particles carrying 0–2 charges at the applied voltage of -2.1 kV in Figures 4.5a–c. In Figure 4.5, the ion molecular weight was assumed to be 0.050 kg/mol (Adachi at el. 1985) and the inlet particle concentration, 2×10^9 particles/m^3, was taken from the

experimental data. As shown in the figure, the concentration of particles with 0 charge decreases with an increasing axial distance from the entrance of the charging zone, where some particles are charged to 1–2 charges. The pattern of the charged particle concentration field resembles that of the flow field shown in Figure 4.4a and most charged particle loss is seen to occur on the inclined wall surface on the right-hand side where the charged particle concentration is gradually decreased due to electrostatic deposition, leading to a lower charged particle concentration at the charger outlet than that in the charging zone. That is, the extrinsic charging efficiency will be lower than the intrinsic charging efficiency. The numerical results show that flow field in the charger is important to the electrostatic loss of charged particles. Further improvement of the charger to minimize the recirculation regions is an important consideration to reduce the electrostatic loss and increase the extrinsic charging efficiency.

(a)

(b)

(c)
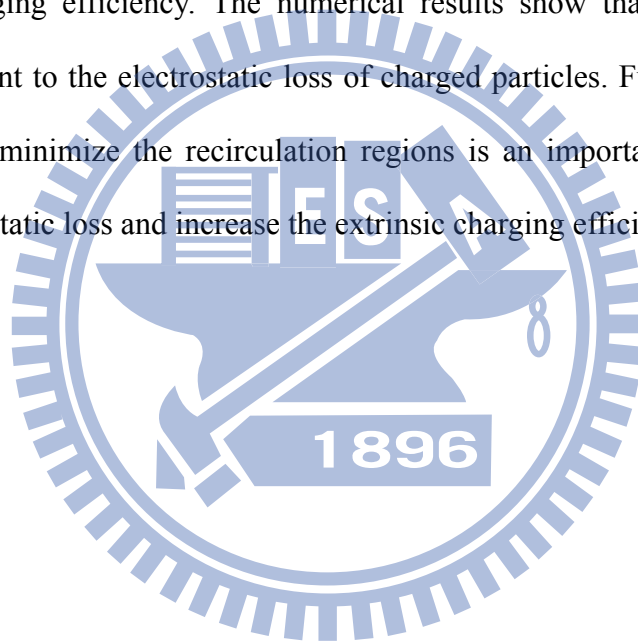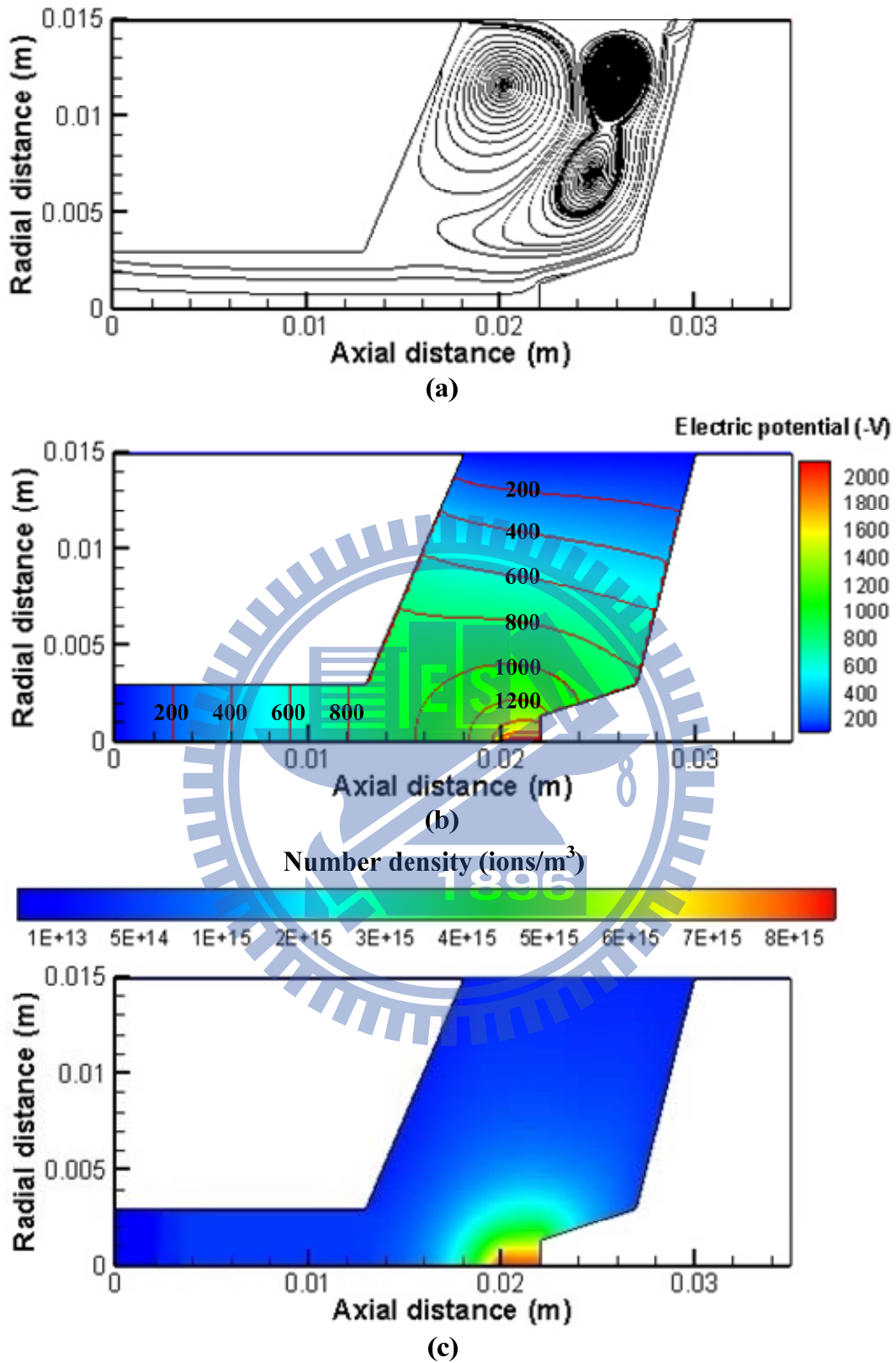
Figure 4.4 (a) Flow streamlines, (b) electric potential field, and (c) ion concentration field at Q_{sh} = 3 L/min in the charger with axial sheath air. The applied voltage was -2.1 kV.

Uncharged particle concentration distribution (particles/m³)

(a)

Charged particle concentration distribution (particles/m³)

(b)

Charged particle concentration distribution (particles/m³)

(c)
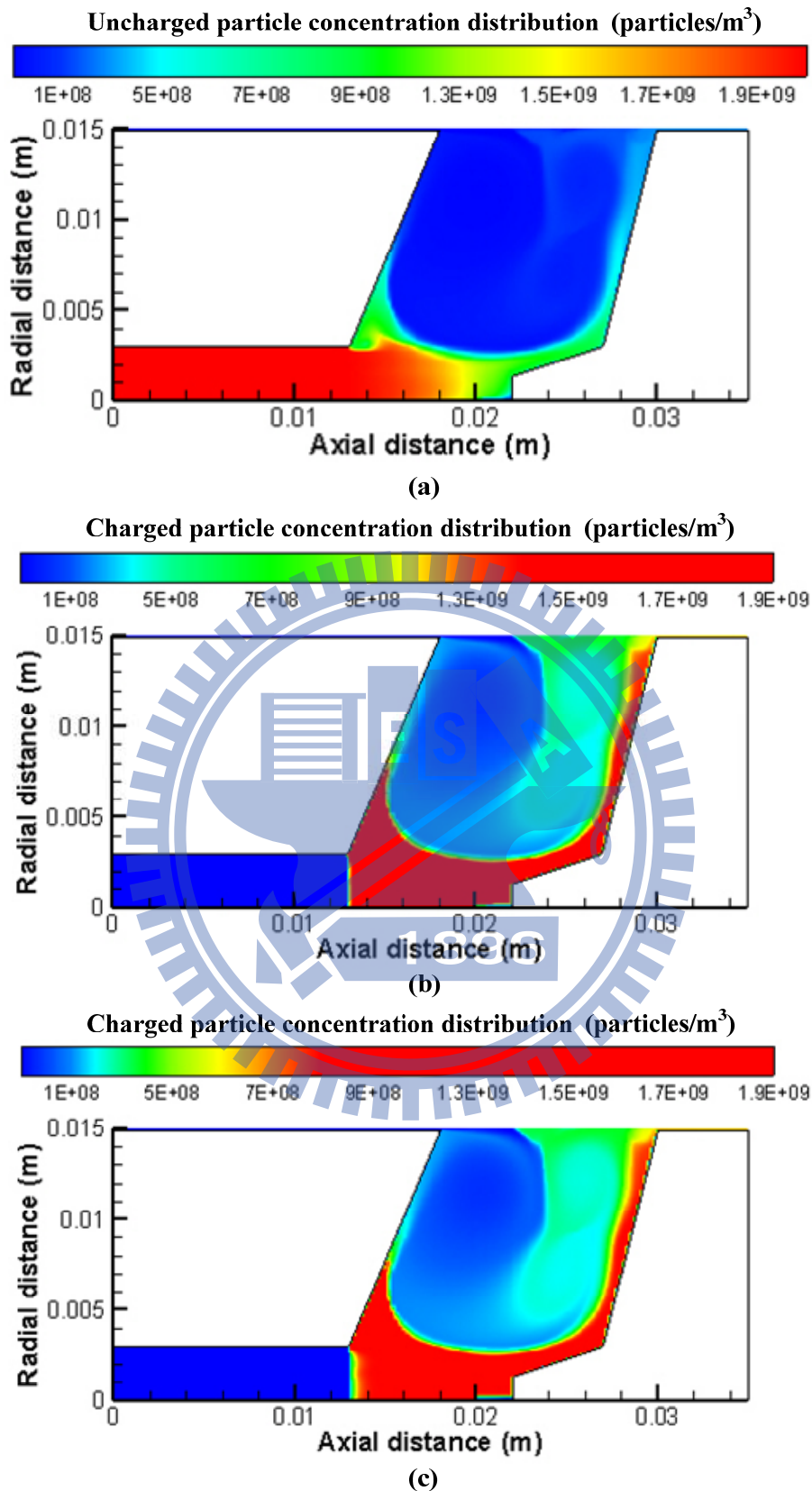
Figure 4.5 Number concentration field of 20 nm particles carrying 0–2 charges in the charger with axial sheath air when the applied voltage was -2.1 kV at Q_{sh} = 3 L/min. (a) 0 charge, (b) 1 charge, (c) 2 charges.

4.2.2 Charging efficiency and electrostatic loss

Figures 4.6a and b show the comparison of the extrinsic charging efficiency between the numerical results and experimental data of the charger with axial sheath air at $Q_{sh} = $ 3 L/min. The values of ion molecular weights of positive and negative ions in the open literature shown in Table 1 of Lin and Tsai (2010) were also used to examine the effect of the ion molecular weight on the charging efficiency and electrostatic loss in the present simulation. It is seen that the extrinsic charging efficiency increases with an increasing particle diameter for both positive and negative applied voltages. However, a higher applied voltage does not result in a higher extrinsic charging efficiency for a given particle diameter. For example, when the applied voltage is increased from +1.9 to +2.0 kV, the experimental extrinsic charging efficiency increases from 29.7% to 39.3% for 10 nm particles but decreases from 69.4% to 65.7% for 20 nm particles. When the applied voltage is increased from +2.0 to +2.1 kV, the experimental extrinsic charging efficiency decreases from 39.3% to 34.1% for 10 nm particles and but decrease from 65.7% to 60.0% for 20 nm particles. Hence, there exists an optimum applied voltage depending on particle size, at which the extrinsic charging efficiency is the maximum.

In Figures 4.6a and b, the predicted extrinsic charging efficiency is shown to be in good agreement with the experimental data with a deviation of 0.4%–5.3% and 0.7%–7.0%, respectively, at positive and negative applied voltages. Within the range of positive ion molecular weight from 0.109 to 0.290 kg/mol, numerical results show that there are no significant differences in the extrinsic charging efficiency when different ion molecular weights were used. The calculated extrinsic charging efficiency ranges from 5.4% ~ 5.9% to 4.9% ~ 5.6% for 2.5 nm particles, from 5.8% ~ 8.2% to 5.4% ~ 7.8% for 3 nm particles, from 9.5% ~ 14.8% to 8.7% ~ 14.5% for 5 nm particles, from

34.5% ~ 40.0% to 32.8% ~ 36.8% for 10 nm particles, and from 64.0% ~ 67.4% to 62.7% ~ 65.7% for 20 nm particles, respectively, at the applied voltage of +1.9 ~ +2.1 kV. This is because a lower ion molecular weight leads to a higher charging level at a given ion mobility. Similar trend is also found at negative applied voltages, as shown in Figure 4.6b. Because of higher mobility of negative ions, the predicted charging efficiency is slightly higher for negative polarity than that for the positive polarity, which is to be expected.
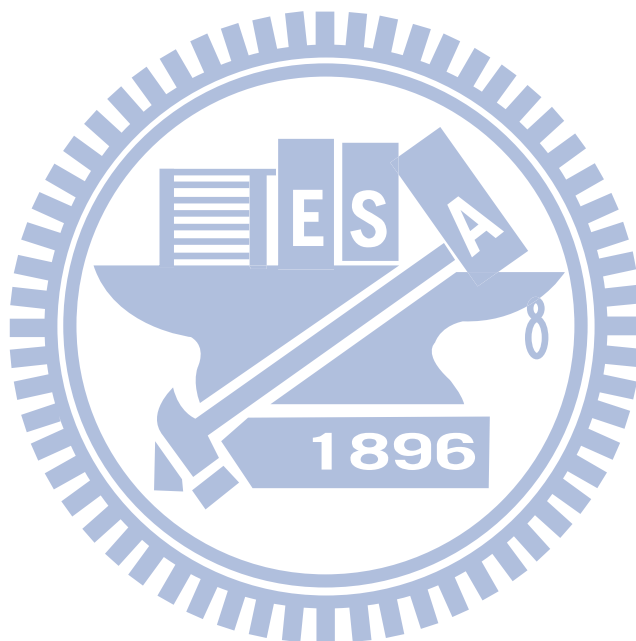
Figure 4.6 Comparison of the extrinsic charging efficiency of the charger with axial sheath air between the numerical results and experimental data at Q_{sh} = 3 L/min. (a) Positive voltage, (b) negative voltage.

Figures 4.7a and b show the comparison of the electrostatic loss of charged particles between the numerical values and experimental data at Q_{sh} = 3 L/min. The maximum electrostatic loss is seen to occur at c.a. 10 nm particles at both positive and negative applied voltages. It is because the charged fraction of particles smaller than 10 nm in diameter decreases with a decrease in particle diameter, while the electrical mobility of particles larger than 10 nm decreases as the particle size is increased (Alonso et al. 2006; Tsai et al. 2010). Again, no significant differences in the electrostatic loss are observed when different ion molecular weights are used. Besides, the simulated convection-diffusion loss of charged particles is insignificant compared to the electrostatic loss and thus it can be safely neglected (data not shown). This finding is consistent with that found by Alonso et al. (2006).

By Equation (3.31), the simulated intrinsic charging efficiency is calculated and compared with the experimental data as shown in Figures 4.8a and b. As shown in Figure 4.8, the intrinsic charging efficiency increases with an increasing corona voltage and particle diameter. The present numerical results agree well with the experimental intrinsic charging efficiency at both positive and negative applied voltages. The experimental intrinsic charging efficiency of 20 nm particle reaches up to 84.2% and 83.7% at the applied voltage of +2.1 and -2.1 kV, respectively. However, for particles with $d_p < 10$ nm, the intrinsic charging efficiency of the charger with axial sheath air is not high enough to achieve a higher extrinsic charging efficiency even if the charged particle loss is minimized. In this case, increasing the intrinsic charging efficiency is also essential to the improvement of the extrinsic charging efficiency for particles smaller than 10 nm in diameter.

Figure 4.7 Comparison of the electrostatic loss of the charger with axial sheath air between the numerical results and experimental data at Q_{sh} = 3 L/min. (a) Positive voltage, (b) negative voltage.
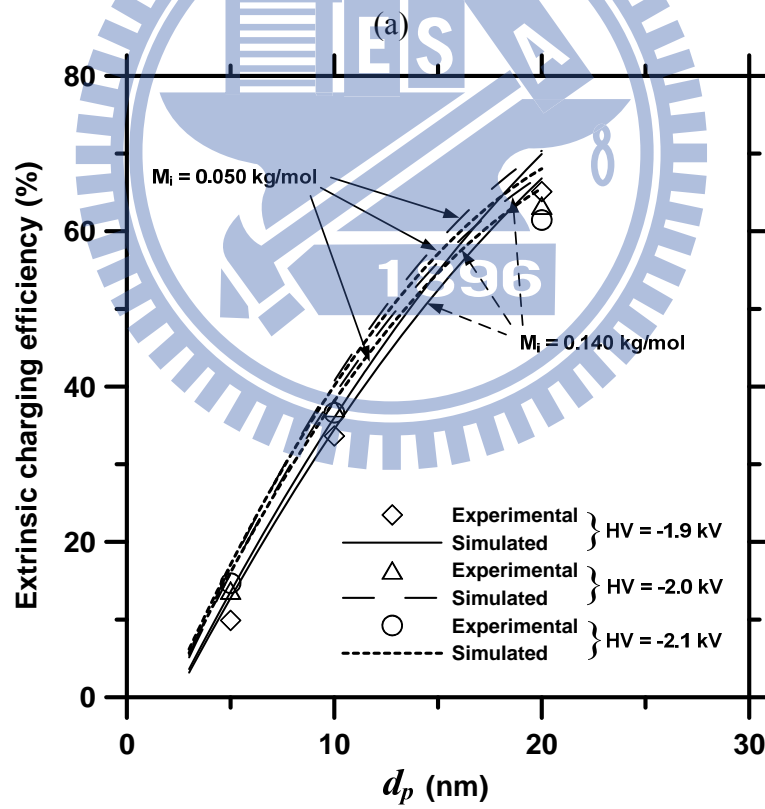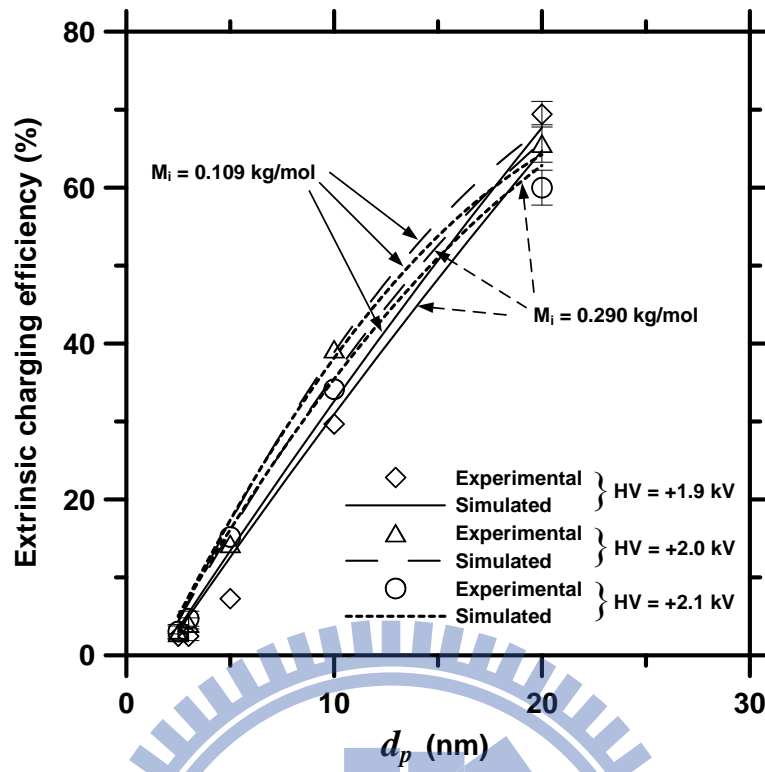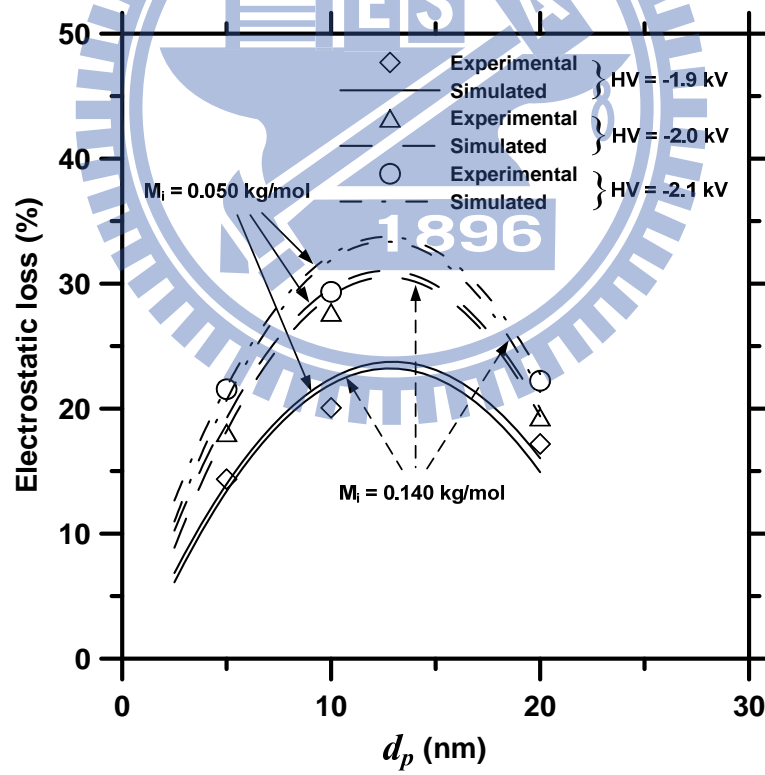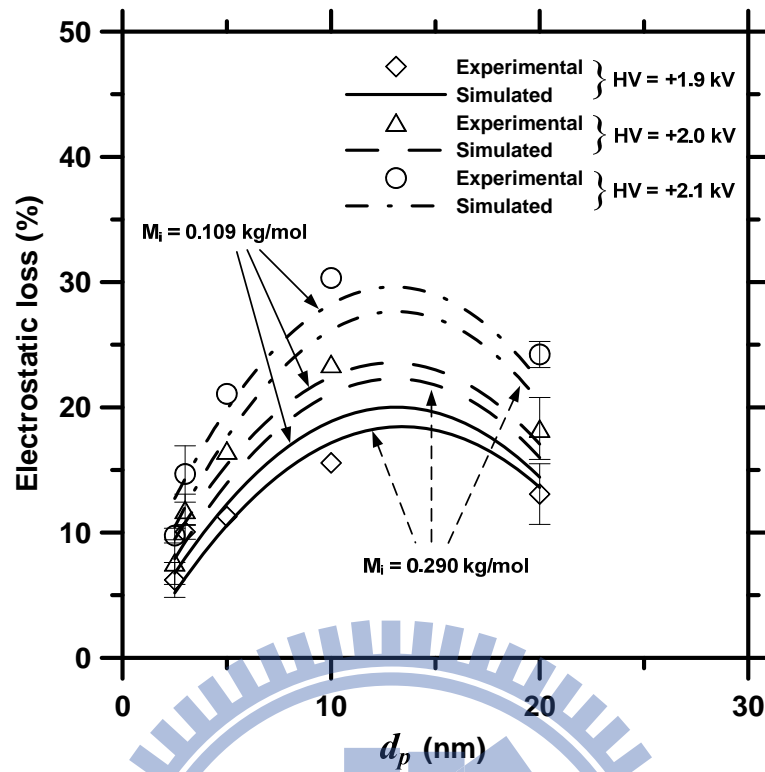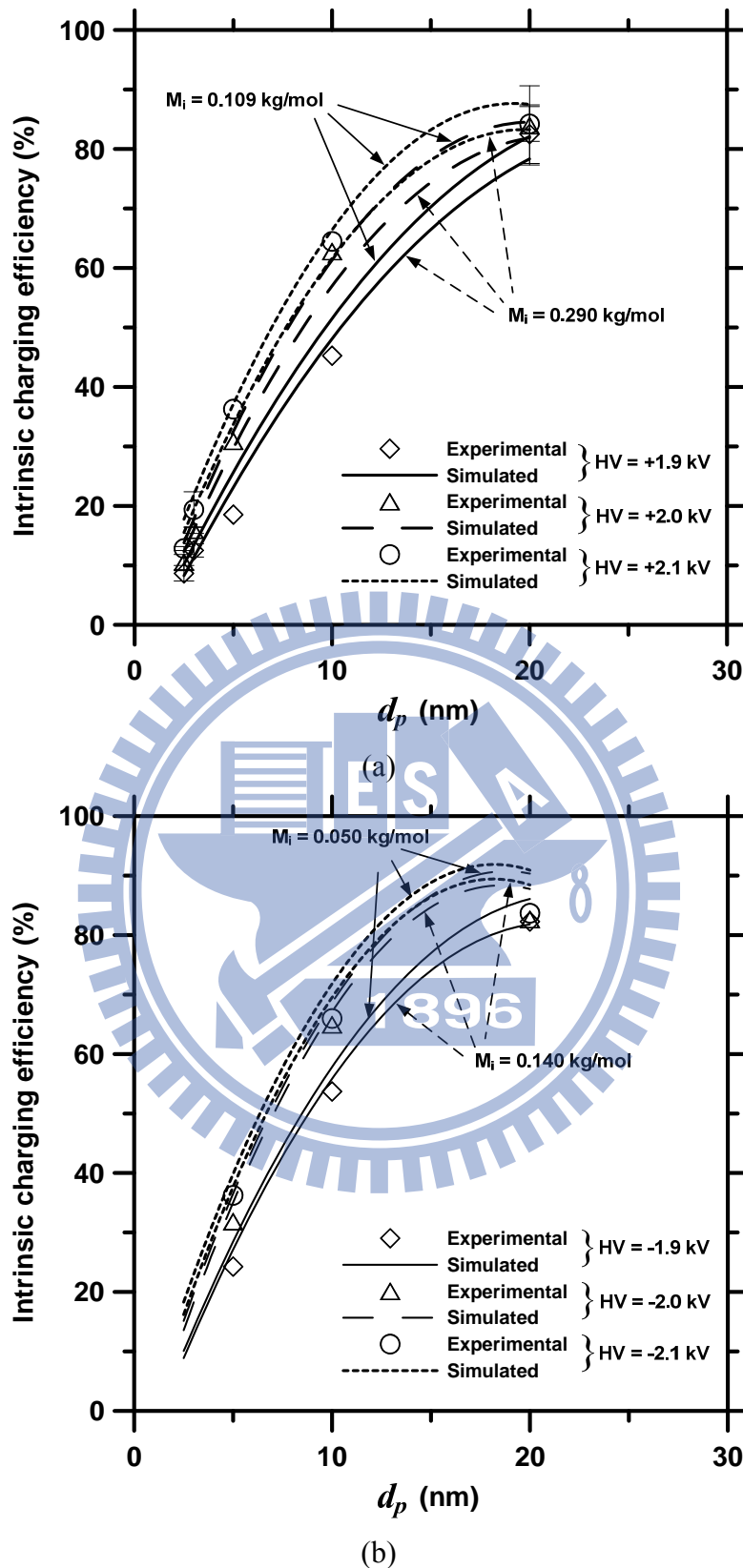
Figure 4.8 Comparison of the intrinsic charging efficiency of the charger with axial sheath air between the numerical results and experimental data at Q_{sh} = 3 L/min. (a) Positive voltage, (b) negative voltage.

4.2.3 Particle charge distribution

In addition to the extrinsic charging efficiency, the charge distributions at the exit of the charger for monodisperse particles of different sizes were measured and simulated. An example of the measured charge distribution for particles of 5, 10, and 20 nm at the exit of the charger with axial sheath air is shown in Figures 4.9a and b at Q_{sh} = 3 L/min and the applied voltage of +2.1 and -2.1 kV, respectively. It is seen that particles are either singly charged or uncharged for d_p < 10 nm. Multiply charged particles with up to two charges are observed for 20 nm particles. For example, at the applied voltage of -2.1 kV, the fraction of 20 nm particles carrying 0, 1, and 2 charges at the exit is 0.15, 0.56, and 0.29, respectively, which is very close to 0.14, 0.54, and 0.32 calculated from the numerical number concentration field shown in Figure 4.5.
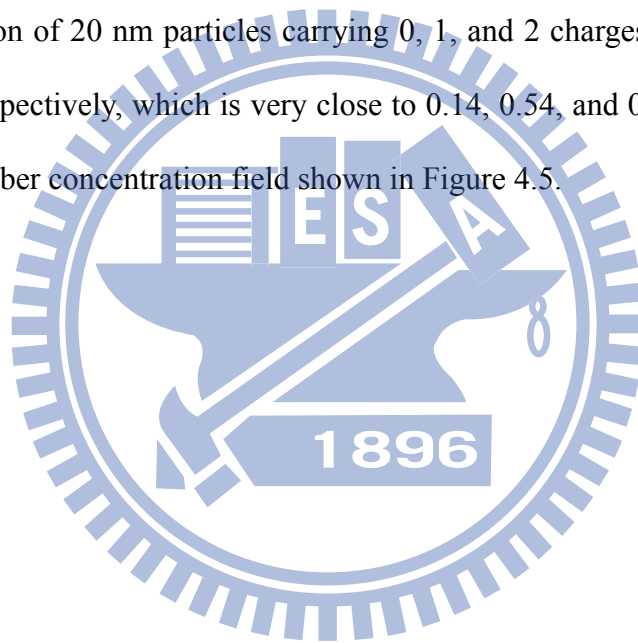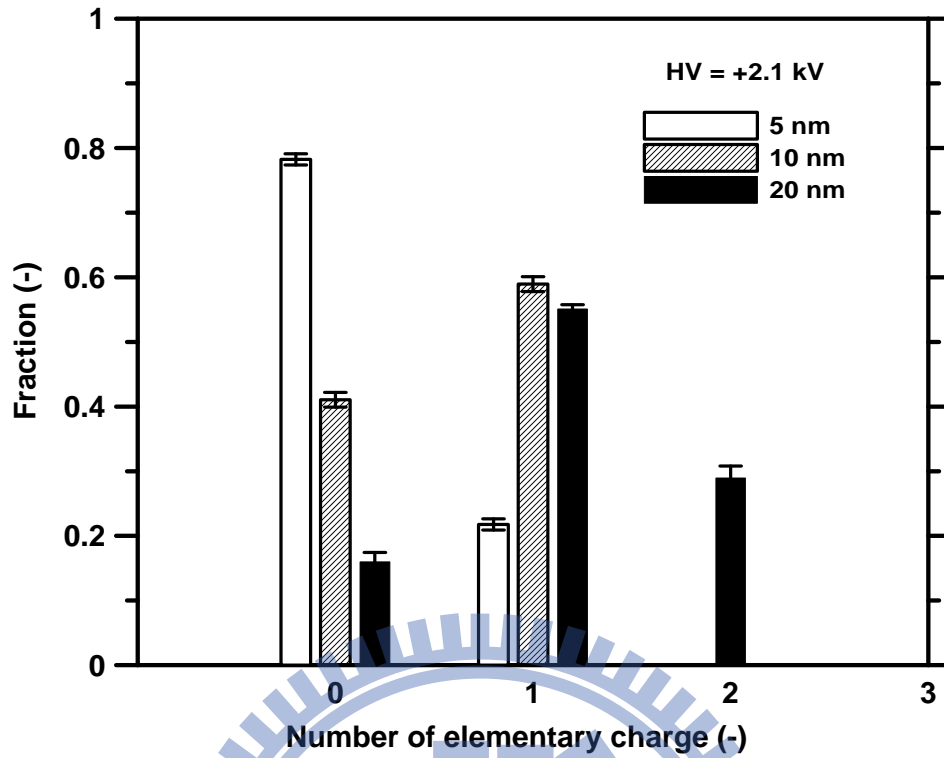
(a)
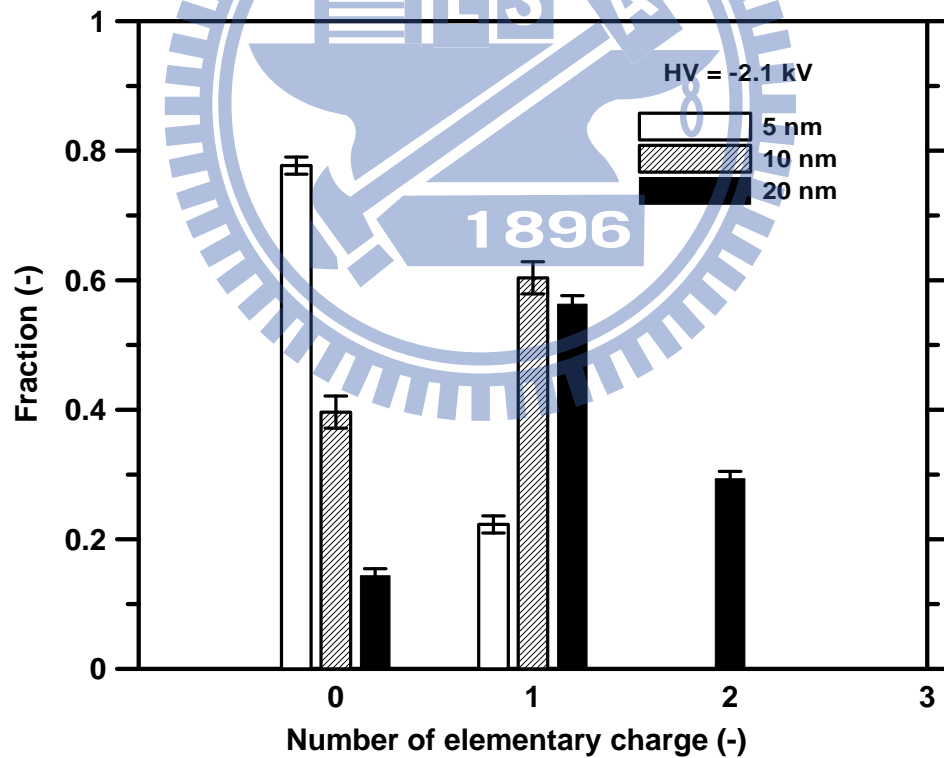
(b)

Figure 4.9 Measured charge distribution at the exit of the charger with axial sheath air at Q_{sh} = 3 L/min at the applied voltage of (a) +2.1 kV and (b) -2.1 kV.

4.3 Performance evaluation of the charger with radial sheath air

As mentioned above, further improvement of the charger with axial sheath air is needed to minimize the recirculation regions to reduce the electrostatic loss and increase the intrinsic charging efficiency to enhance the extrinsic charging efficiency for particles smaller than 10 nm in diameter. For the charger with radial sheath air, charged particle loss was reduced but the charging efficiency was not reported (Cheng et al. 1997). Therefore, the effect of radial sheath air on the charging efficiency and the optimization of the charger remain to be studied. In the last section, the present numerical model is shown to be able to predict the experimental nanoparticle charging efficiency in the single-wire corona unipolar charger with axial sheath air very well for particles smaller than 20 nm in diameter. It is therefore possible to use this model to optimize the charging efficiency for the charger with radial sheath air, which is also the main objective of this study.

In addition to the charger with axial sheath air, a single-wire corona unipolar charger with radial sheath air was proposed to enhance the charging efficiency of nanoparticles. The performance of the charger was evaluated numerically at different aerosol and sheath air flow rates and corona voltages to determine an optimum operating condition. The extrinsic charging efficiency of the charger was then compared with that of the chargers of Chen and Pui (1999) and Kimoto et al. (2010). In the course of study, the relative position between the discharge wire and the sheath air opening was found to be important in reducing charged particle loss. A design with shifted position of the sheath air opening relative to the leading edge of the wire was proposed to further minimize charged particle loss.

Figure 4.10 shows the schematic diagram and calculation domain for the charger with radial sheath air. The charger consists of an insulated Teflon tube (inner diameter ID =

6.35 mm) with a 6 mm long grounded porous metal tube inserted at the center (pore diameter: 10 μm, Mott Corp., Farmington, CT, USA) from which radial sheath air is introduced, and a discharge gold wire of 50 μm in ID and 6 mm in effective length. The effective length refers to the length of the wire exposed to the grounded porous metal tube, where the filtered sheath airflow at the flow rate of 0.7–2.1 L/min is introduced radially into the charger. The aerosol flow from 0.5 to 1 L/min is introduced in the axial direction parallel to the discharge wire. Two designs were studied for the effect of the position of the sheath air opening on reducing the loss of charged particles. As shown in Figure 4.10b, both ends of the sheath air opening are aligned with the ends of the discharge wire in design 1, while in design 2 the sheath air opening is shifted 2 mm toward the left of the leading edge of the wire. In design 2, the 6 mm long grounded region includes 4 mm in the porous tube and 2 mm in the Teflon tube inside which it is coated with conducted material.

A 2-D numerical simulation was conducted to evaluate the performance of the charger with radial sheath air and determine the optimum operating condition. The calculation domain of 20 mm in length and 3.175 mm in width is shown in Figure 4.10b, in which the dotted lines represent the sheath air opening (grounded) of 6 mm in length which is exactly equal to the length of the wire.
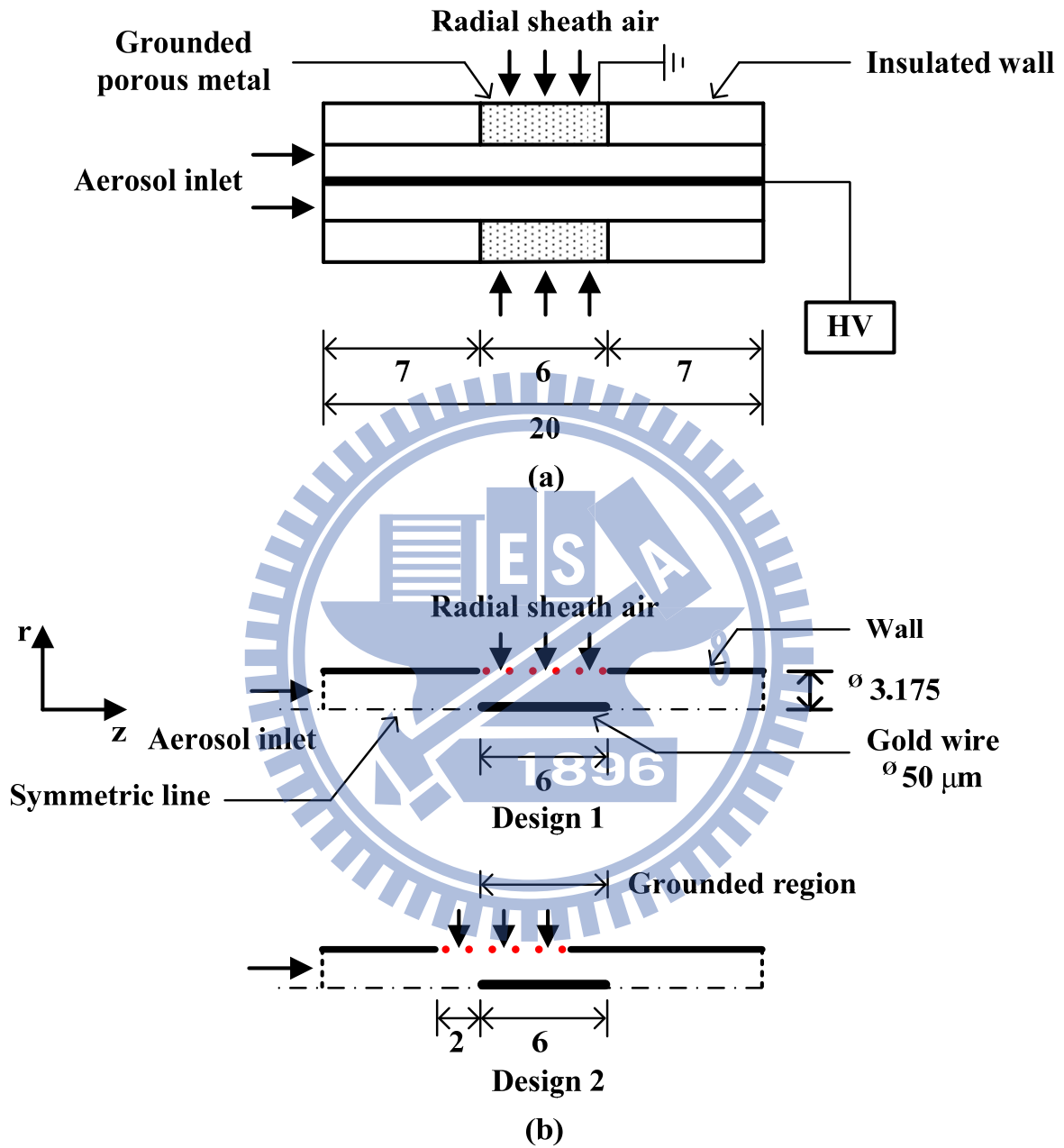
Figure 4.10. (a) Schematic diagram and (b) calculation domains of design 1 and design

2 for the charger with radial sheath air (unit: mm; HV: high voltage).

4.3.1 Characteristic of the V-I curve

The corona voltage with the corresponding corona current in the charger with radial sheath air was calculated by the wire-in-tube electrostatic precipitator (ESP) theory (Tsai et al. 2008). The critical voltage, V_c, for the corona generation in the wire-in-tube ESP was calculated as:

$$V_c = E_b \, r_w \ln(r_t / r_w) \tag{4.1}$$

where $E_b = 3000 + 127 \, d_w^{-\frac{1}{2}}$ is the breakdown voltage (kV/m), d_w is the diameter of the discharge wire (m), and r_t is the radius of the tube (m). The ion concentration, N_i, in the wire-in-tube ESP was estimated by the following equation:

$$N_i = \frac{I}{eEZ_i A} \tag{4.2}$$

where E is the electric field strength (V/m) and A is the cross area of ions (m^2). The corona voltage V is given by

$$V = V_c + E_b \, r_w \left[\sqrt{1+\theta} - 1 - \ln\left(\frac{1 + \sqrt{1+\theta}}{2} \right) \right] \tag{4.3}$$

where θ is defined as

$$\theta = \frac{I \, r_t^2}{2\pi \, \varepsilon_0 \, Z_i \, E_b^2 \, r_w^2} \tag{4.4}$$

Figure 4.11a shows the corona current as a function of the applied voltage in the wire-in-tube ESP of 6 mm in length and 6.35 mm in diameter with the wire diameter of

50 μm. The corona current varies from 1×10^{-6} to 1.278×10^{-1} A/m at the applied voltage of +2.5 to +14.8 kV. The ion concentration variation with the applied positive voltage is shown in Figure 4.11b. When the applied voltage is increased from +2.5 to +14.8 kV, the ion concentration increases from 2.2×10^{14} to 7.8×10^{16} ions/m^3. These theoretical corona voltage and current values are used for the simulation of the electric potential and ion concentration fields as shown below.

(a)

(b)
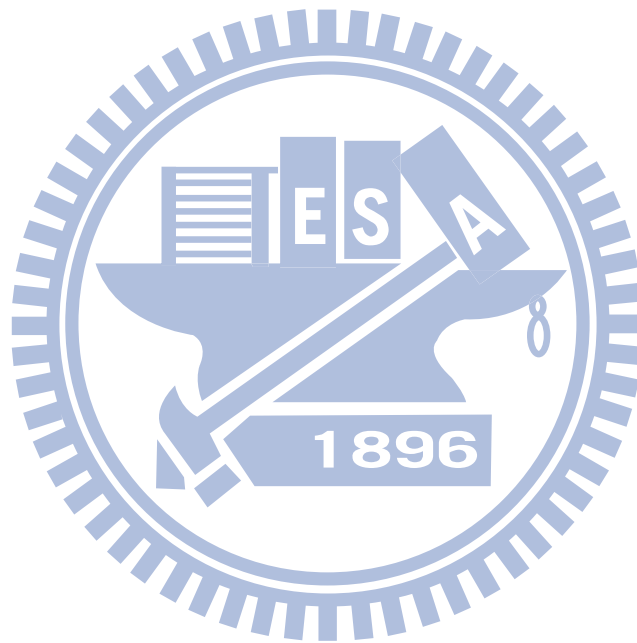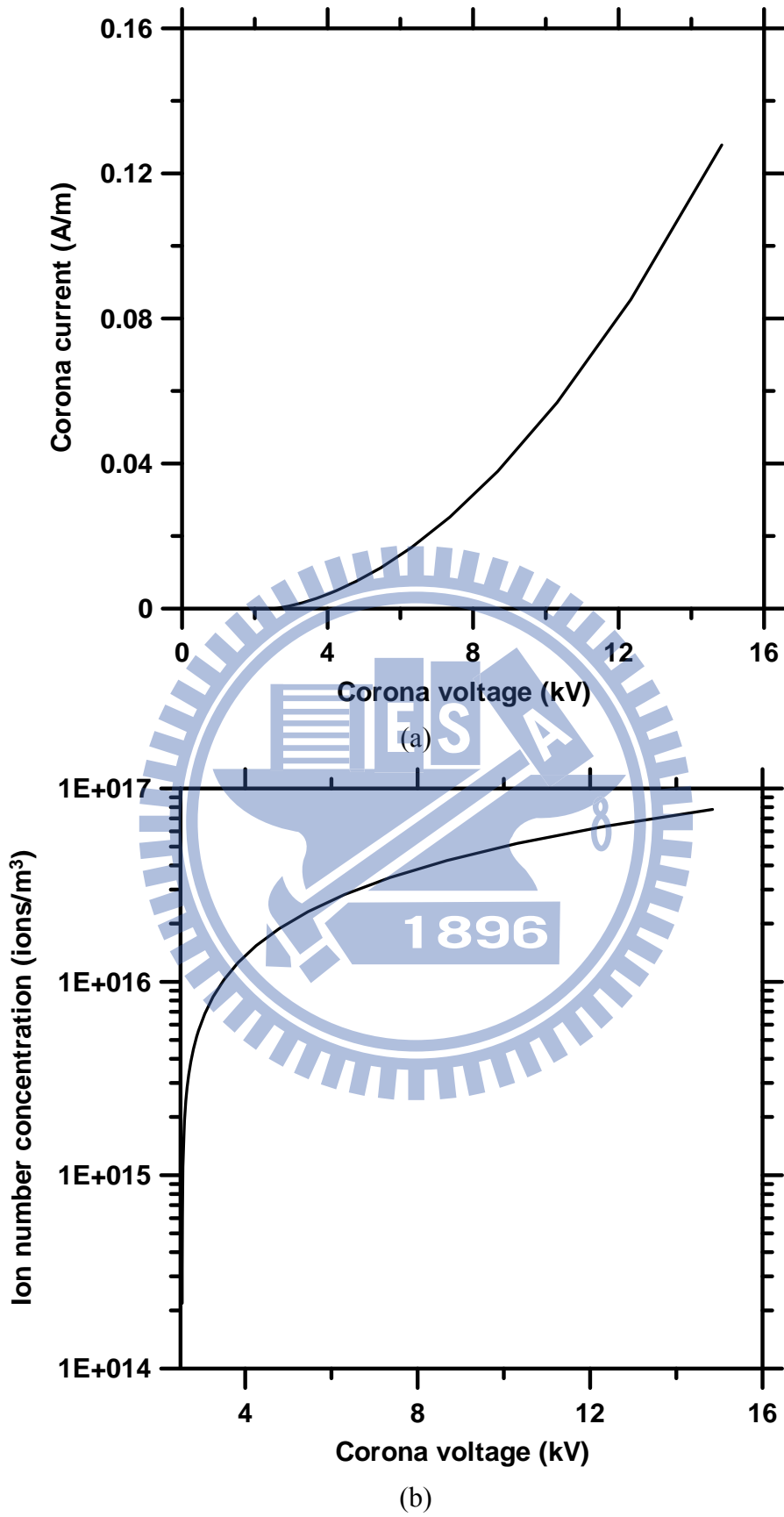
Figure 4.11 (a) Corona current versus the corona voltage and (b) ion number concentration versus with the corona voltage in the wire-in-tube ESP.

4.3.2 Flow streamlines, electric potential, ion concentration, and charged particle concentration fields

The flow, electric potential, and ion concentration fields were calculated first before the charged particle concentration could be calculated. The simulation conditions for design 1 are: applied voltage = +2.9 kV, Q_a = 0.5 ~ 1 L/min, and Q_{sh} = 0 ~ 2.1 L/min; for design 2 are: applied voltage = +2.9 ~ +4.2 kV, Q_a = 0.5 L/min, and Q_{sh} = 0.7 L/min. An example of the calculated flow, electric potential, and ion number concentration fields is shown in Figure 4.12 for design 1 at the applied voltage of +2.9 kV, Q_a = 1 L/min, and Q_{sh} = 0.7 L/min. For the other operating conditions, the patterns of flow, electric potential, and ion concentration field are similar. Compared to the charger with axial sheath air, no recirculation region for aerosol flow is observed near the wall of the charging zone as shown in Figure 4.12a. With the use of radial sheath air, the streamlines associated with aerosol flow are pushed away from the wall of the charging zone where charged particle loss would otherwise likely occur. Therefore, the reduction of charged particle loss is expected. Both electric potential and ion concentration are seen to be the highest near the wire but decay from the wire rapidly (Figures 4.12b and c). In Figure 4.12c, the ion number concentration is also at its maximum at the wire surface, which is 1.1×10^{16} ions/m^3 at the axial distance of 0.007 ~ 0.013 m and decays to about 7.9×10^{15} ions/m^3 at the radial distance of 0.015 m and 5.2×10^{15} ions/m^3 near the wall at the same axial position. The ion concentration also exists in the region before the leading edge of the wire where particle charging also takes place, and charged particle deposition on the wall would likely occur without the protection of radial sheath air flow.

Figure 4.12 (a) Flow streamlines, (b) electric potential field, and (c) ion concentration field at Q_a = 1 L/min and Q_{sh} = 0.7 L/min in design 1. The applied voltage was +2.9 kV.

At the same applied voltage and flow rates, the pattern of the flow filed of design 2 is different from design 1, while the patterns of the electric potential and ion concentration fields of design 2 are similar (figures not shown). In addition to the applied voltage of +2.9 kV, simulation for design 2 at +3.5 and 4.2 kV was also conducted. An example for the flow, electric potential, and ion number concentration fields in design 2 at the applied voltage of +3.5 kV, Q_a = 0.5 L/min, and Q_{sh} = 0.7 L/min is shown in Figure 4.13. When shifting the sheath air opening 2 mm relative to the left of the leading edge of the discharge wire, the effective region of inward radial sheath air where aerosol flow are pushed way from the wall is seen to be also extended to the left, where charged particle loss would otherwise occur (Figure 4.13a). Compared to the patterns shown in Figures 4.12b and c, with an increasing corona voltage from +2.9 kV to +3.5 kV, both electric field strength and ion concentration are increased. The ion concentration at the wire surface is increased from 1.1×10^{16} to 3.6×10^{16} ions/m^3 at the axial distance of 0.007 ~ 0.013 m, which will lead to a higher intrinsic charging efficiency.
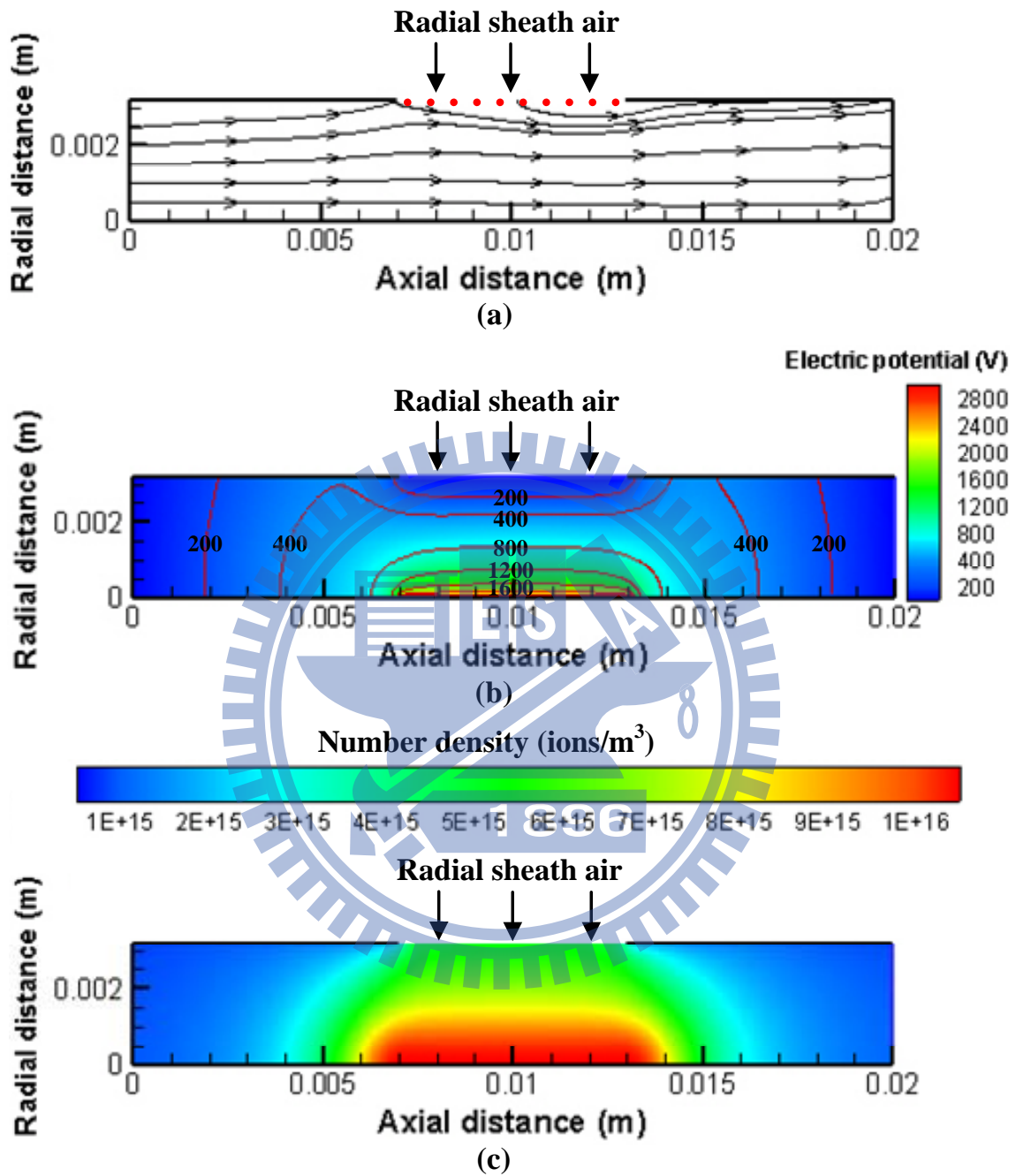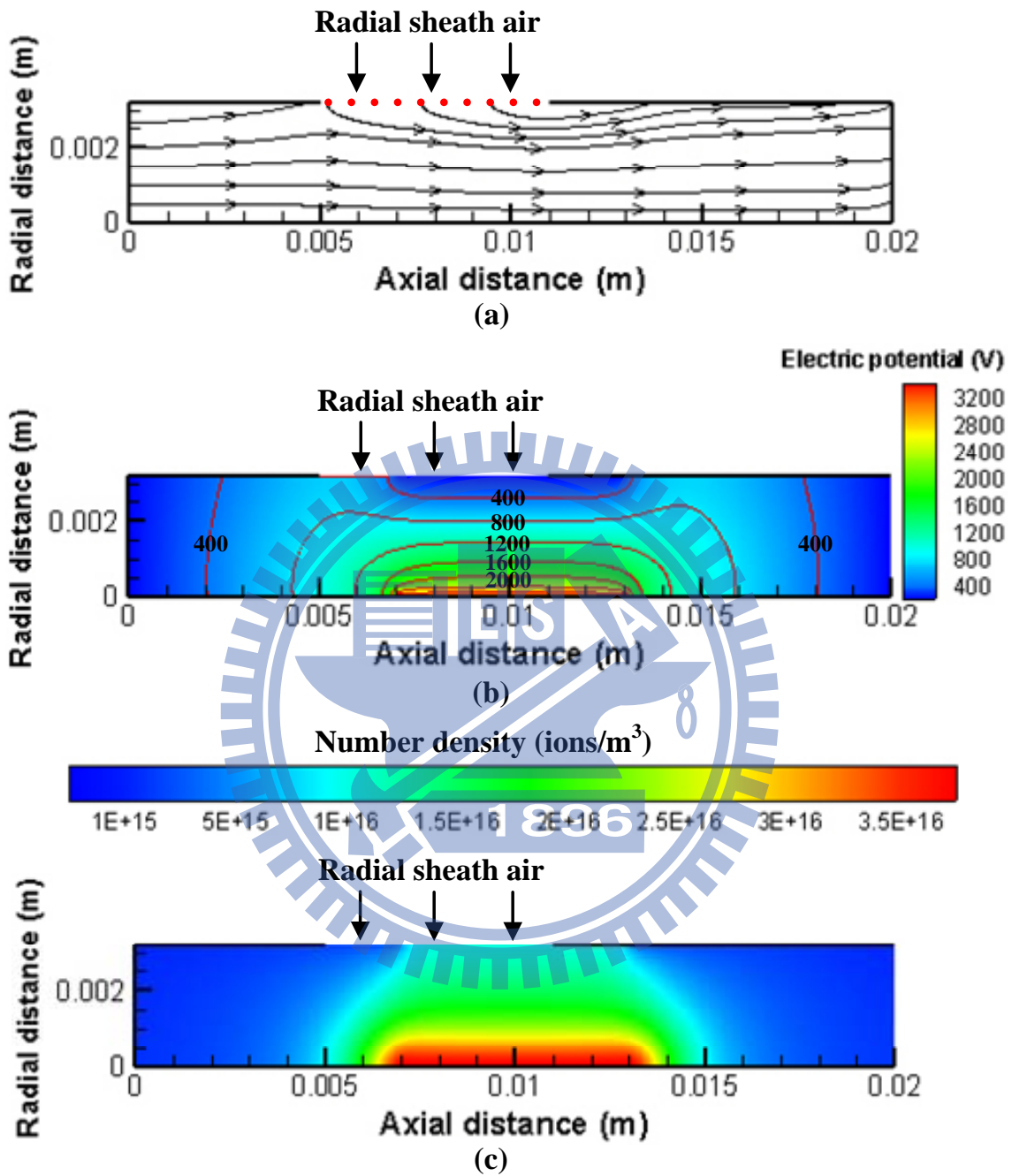
Figure 4.13 (a) Flow streamlines, (b) electric potential field, and (c) ion concentration field at Q_a = 0.5 L/min and Q_{sh} = 0.7 L/min in design 2. The applied voltage was +3.5 kV.

On the basis of the flow, electric potential, and ion concentration fields, the spatial distribution of charged particles was calculated. An example for 20 nm particles carrying 0–2 charges in design 1 at the applied voltage of +2.9 kV, Q_a = 1 L/min, and Q_{sh} = 0.7 L/min is shown in Figures 4.14a–c. The ion molecular weight and the inlet particle concentration were assumed to be 0.109 kg/mol (Adachi et al. 1985) and 2×10^9 particles/m^3 in the simulation, respectively. The concentration of particles with 0 charge decreases with an increasing axial distance from the entrance of the charger, where some particles are charged to 1–2 charges. With the use of radial sheath air, the charged particles migrating toward the wall are seen to be pushed toward the core of the tube and the electrostatic loss is reduced. Zero deposition region of charged particles is also observed near the wall surface on the right-hand-side of the porous tube. Major charged particle loss occurs on the wall surface on the left-hand-side of the sheath air opening (or porous tube).

The effect of the position of the sheath air opening on reducing the loss of charged particles was studied. The simulated number concentration field of 20 nm particles carrying 0–2 charges in design 2 at the applied voltage of +3.5 kV, Q_a = 0.5 L/min, and Q_{sh} = 0.7 L/min is shown in Figure 4.15. Compared to the pattern of the charged particle concentration field shown in Figure 4.14, with increasing corona voltage from +2.9 to + 3.5 kV and decreasing aerosol flow rate from 1 to 0.5 L/min, the starting position in axial direction where particles acquire charge was found to shift toward the left. Zero deposition region of charged particles was also extended 2 mm to the left, meaning more effective reduction of charged particle loss. That is, at the same operating condition design 2 will have less electrostatic loss than design 1 because of its smaller deposition region of charged particles.

Uncharged particle concentration distribution (particles/m³)

(a)

Charged particle concentration distribution (particles/m³)

(b)

Charged particle concentration distribution (particles/m³)

(c)
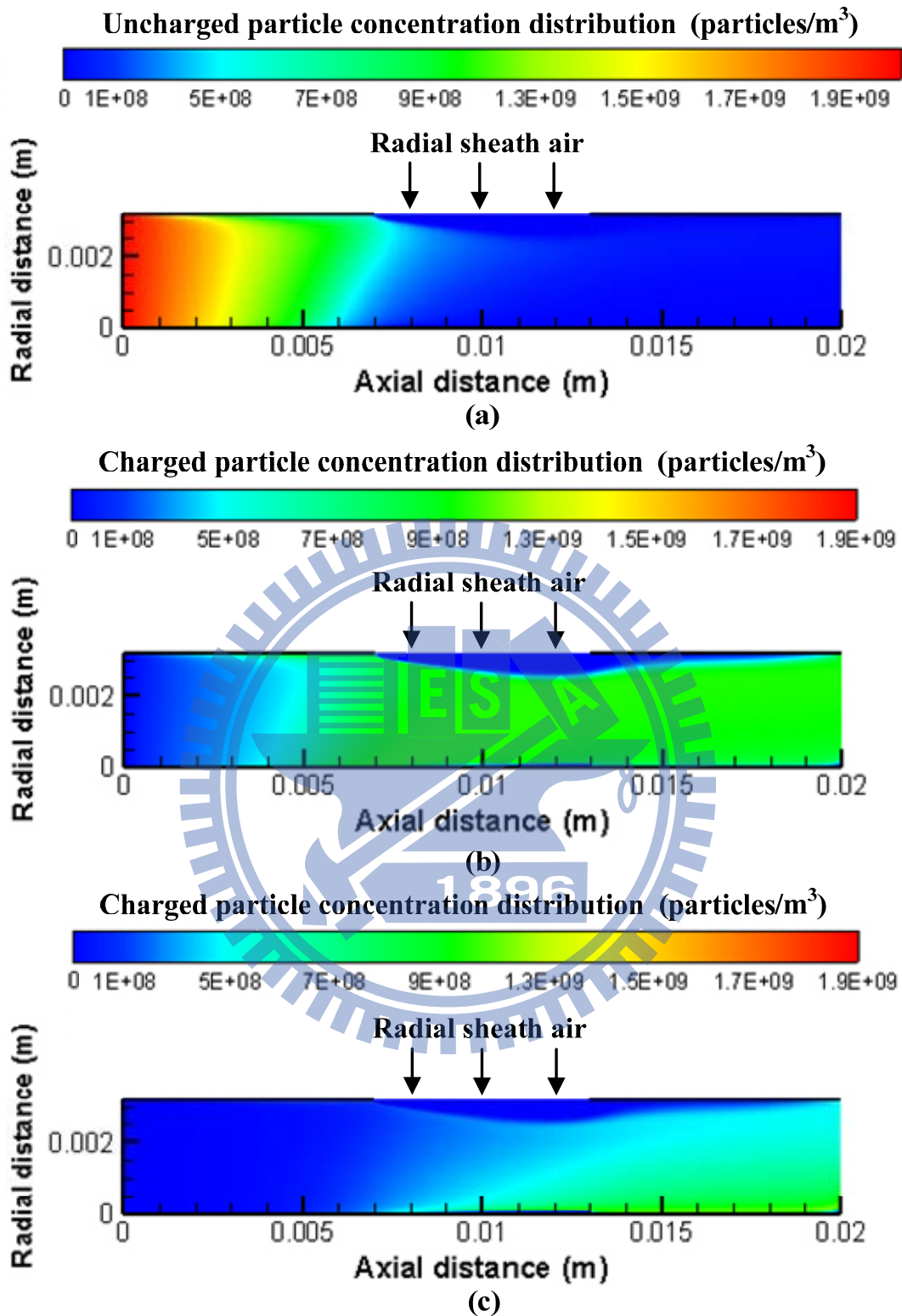
Figure 4.14 Number concentration field of 20 nm particles carrying 0–2 charges in design 1 when the applied voltage was +2.9 kV at Q_a = 1 L/min and Q_{sh} = 0.7 L/min. (a) 0 charge, (b) 1 charge, (c) 2 charges.
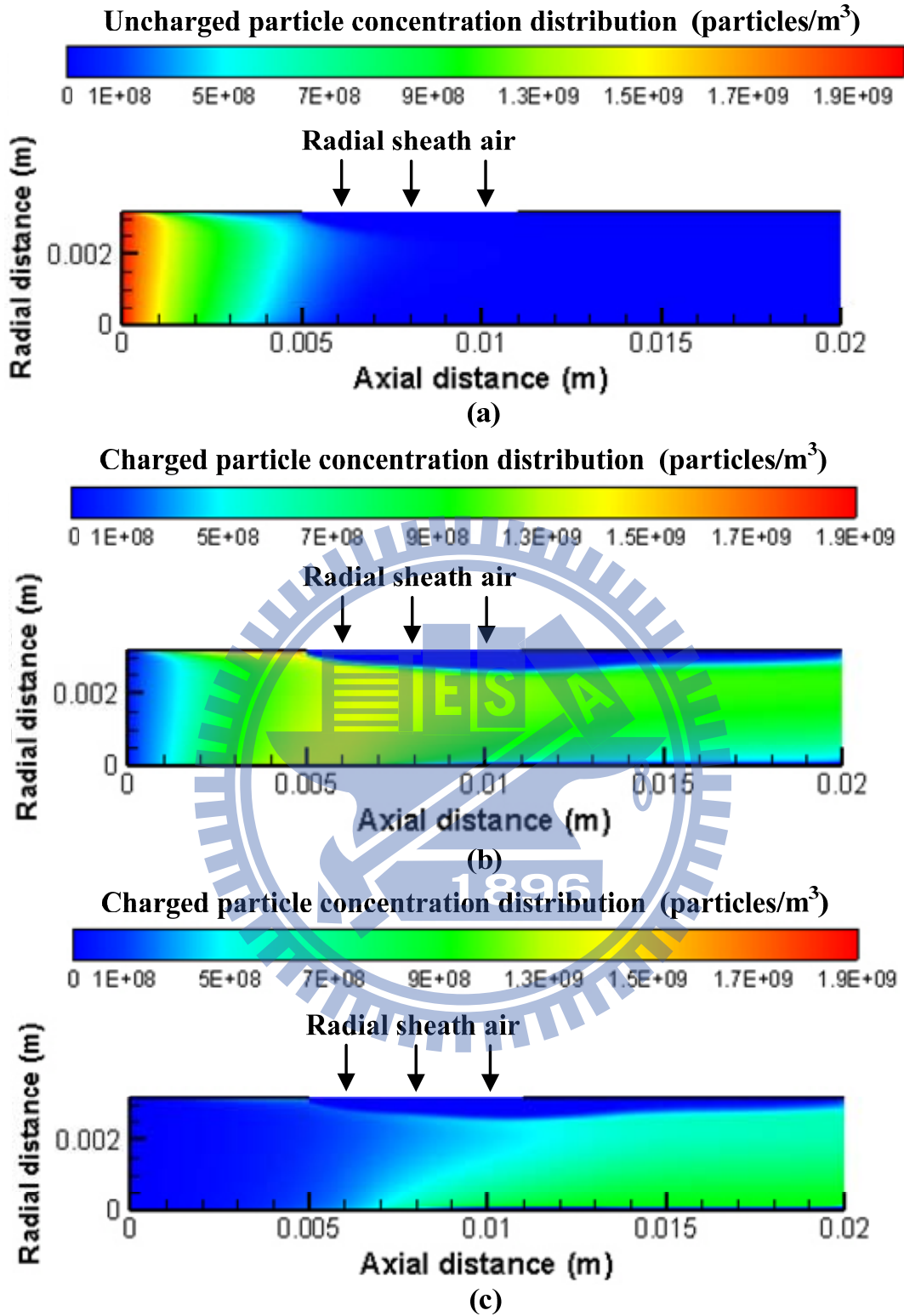
Figure 4.15 Number concentration field of 20 nm particles carrying 0–2 charges in design 2 when the applied voltage was +3.5 kV at Q_a = 0.5 L/min and Q_{sh} = 0.7 L/min. (a) 0 charge, (b) 1 charge, (c) 2 charges.

4.3.3 Simulated extrinsic charging efficiency

In practical applications, the extrinsic charging efficiency is the most important index of the performance of the unipolar charger. The predicted extrinsic charging efficiency is shown in Figure 4.16a for design 1 at different aerosol and sheath air flow rates at the applied voltage of +2.9 kV. In general, the extrinsic charging efficiency of design 1 increases with decreasing Q_a from 1 to 0.5 L/min at the applied voltage of +2.9 kV. At a given aerosol flow rate, the extrinsic charging efficiency increases with increasing Q_{sh} from 0 to 0.7 L/min due to the reduction of charged particle loss. For example, the extrinsic charging efficiency of design 1 for particles with d_p = 2.5–40 nm increases from 0.6%–83.7% to 7.2%–92.2% and from 0.8%–90.1% to 6.8%–94.5% at Q_a = 0.5 and 1 L/min, respectively, when Q_{sh} is increased from 0 to 0.7 L/min at the applied voltage of +2.9 kV. At Q_a = 1 L/min, further increase of Q_{sh} from 0.7 to 2.1 L/min does not increase the extrinsic charging efficiency any further. The extrinsic charging efficiency is 6.6%–90.6% at Q_{sh} = 2.1 L/min, which is very close to that of Q_{sh} = 0.7 L/min. This is because that electrostatic loss in the charger is effectively reduced at Q_{sh} = 0.7 L/min but does not change very much at Q_{sh} = 2.1 L/min, as will be elucidated in the next section. Theses results also show that both aerosol and sheath air flow rates can be adjusted to maximize the extrinsic charging efficiency.

At the applied voltage of +2.9 kV, design 1 operating at Q_a = 0.5 L/min and Q_{sh} = 0.7 L/min shows the highest extrinsic charging efficiency among different flow rate combinations, but not high enough for particles smaller than 10 nm in diameter as compared to the chargers of Chen and Pui (1999) and Kimoto et al. (2010). It is therefore necessary to change the design and operating conditions to achieve a higher

extrinsic charging efficiency while keeping charged particle loss as small as possible. This is the intended purpose of design 2.

Figure 4.16b shows the predicted extrinsic charging efficiency as a function of particle diameter for design 2 at different applied voltages. At the same operating condition, the performance of design 2 is slightly higher than design 1 over the studied particle size range. The extrinsic charging efficiency of design 2 is 9.3%–98.7% (d_p = 2.5–40 nm) at the applied voltage of +2.9 kV, Q_a = 0.5 L/min, and Q_{sh} = 0.7 L/min, but the improvement is still limited for the charging efficiency of particles smaller than 10 nm in diameter. But if the applied voltage is increased from +2.9 to +3.5 kV, the extrinsic charging efficiency of design 2 is increased substantially to 15.2%–65.8% for particles with d_p = 2.5–10 nm, while it is slightly decreased to 75.3%–95.2% for particles with d_p = 20–40 nm. Further increase in the applied voltage from +3.5 to +4.2 kV results in the decrease in the extrinsic charging efficiency to 13.7%–92.3% (d_p = 2.5–40 nm) due to increasing charged particle loss as will be shown later. Thus under a proper operating condition, the maximum extrinsic charging efficiency for particles smaller than 10 nm in diameter of design 2 is comparable to that of the chargers of Chen and Pui (1999) and Kimoto et al. (2010) yet the design is simpler and more compact.
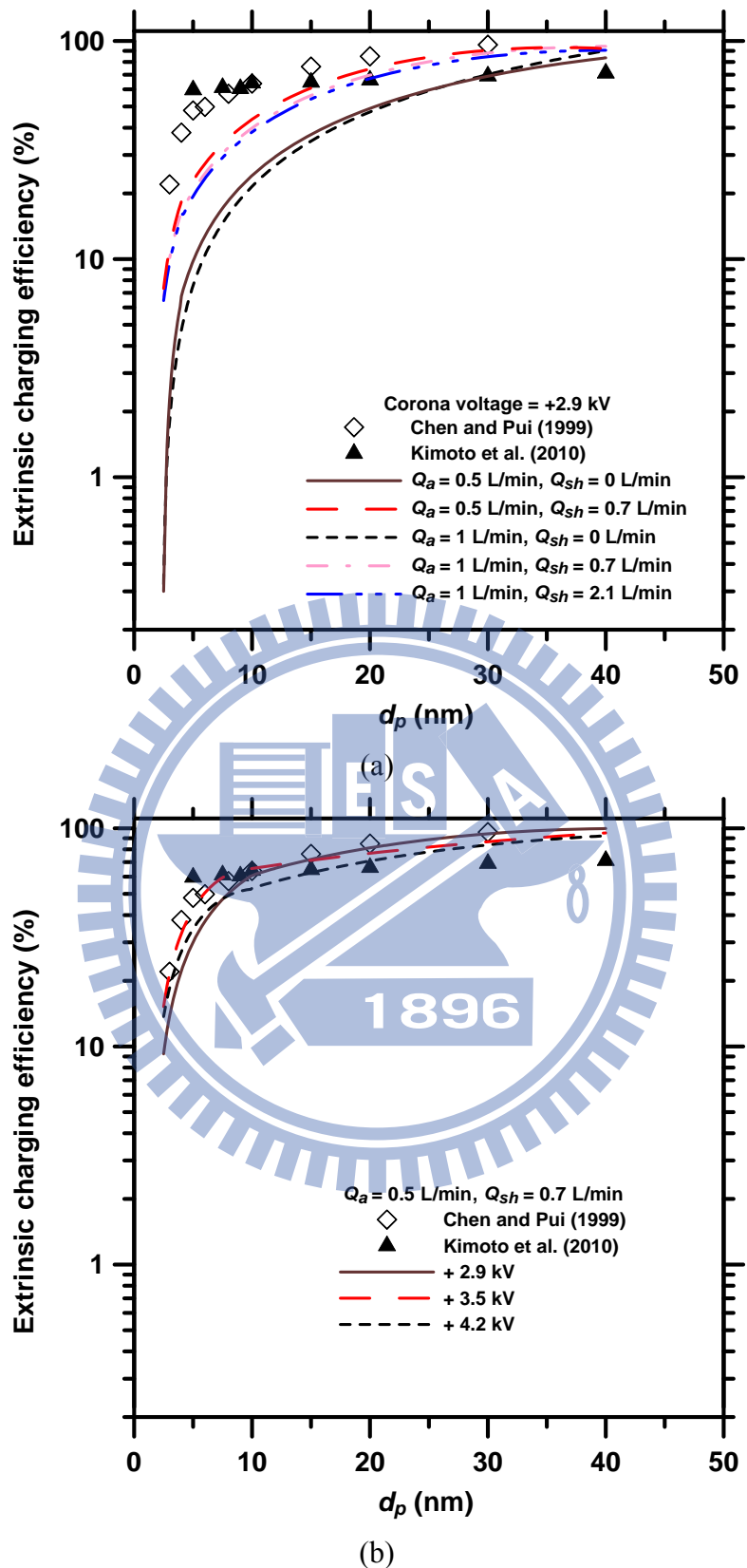
Figure 4.16 Comparison of the predicted extrinsic charging efficiency of the charger with radial sheath air with that of the unipolar chargers of Chen and Pui (1999) and Kimoto et al. (2010). (a) design 1, (b) design 2.

4.3.4 Electrostatic loss and intrinsic charging efficiency

The electrostatic loss and the intrinsic charging efficiency of the charger with radial sheath air were investigated at different operating conditions to elucidate the results of the extrinsic charging efficiency in the last section. Results are shown in Figure 4.17 for the electrostatic loss and Figure 4.18 for the intrinsic charging efficiency. Additional comparison of the simulated intrinsic charging efficiency with the theoretical results of a wire-in-tube ESP case can be seen in the Appendix. For design 1, significant improvement in the reduction of charged particle loss is shown in Figure 4.17a. An increase in the sheath air flow rate decreases the electrostatic loss of charged particles at the applied voltage of +2.9 kV. For example, at Q_a = 0.5 L/min, when Q_{sh} is increased from 0 to 0.7 L/min, the electrostatic loss of 2.5–10 nm particles is decreased from 12.1%–54.5% to 3.2%–23.6%. However, the intrinsic charging efficiency is also decreased from 12.8%–82.4% to 10.3%–77.4% (Figure 4.18a). This is the reason why the extrinsic charging efficiency of 2.5–10 nm particles is not as high as the chargers of Chen and Pui (1999) and Kimoto et al. (2010) as discussed before. Further increasing Q_a from 0.5 to 1 L/min results in the decreases in both the electrostatic loss (Figure 4.17a) and intrinsic charging efficiency (Figures 4.18a and A2) with or without radial sheath air. At Q_a = 1 L/min, increasing in Q_{sh} from 0.7 to 2.1 L/min only leads to a limited decrease in the electrostatic loss while the intrinsic charging efficiency decreases continuously because of shorter particle charging time. Therefore, the extrinsic charging efficiency is not improved at Q_a = 1 L/min.

Figures 4.17b and 4.18b show the electrostatic loss and the intrinsic charging efficiency as a function of particle diameter for design 2 at different applied voltages at Q_a = 0.5 L/min and Q_{sh} = 0.7 L/min. It is seen that the electrostatic loss is increased

with an increasing applied voltage at any particle size. The electrostatic loss is increased from 0.4%–12.3% to 3.6%–21.5% (d_p = 2.5–10 nm) when the applied voltage is increased from +2.9 to +3.5 kV. The intrinsic charging efficiency is also increased from 9.7%–74.2% to 18.8%–87.4% (d_p = 2.5–10 nm). Further increasing the applied voltage from +3.5 to +4.2 kV leads to the increase in the intrinsic charging efficiency to 25.3%–91.3% but the electrostatic loss is also increased to 11.6%–38.8%. As a result, the extrinsic charging efficiency is not increased.

By interpolating the data for the electrostatic loss and intrinsic charging efficiency of 2.5–10 nm particles at different applied voltage, it is found that the optimum voltage which has the maximum extrinsic charging efficiency occurs between +3.5 and +3.6 kV.
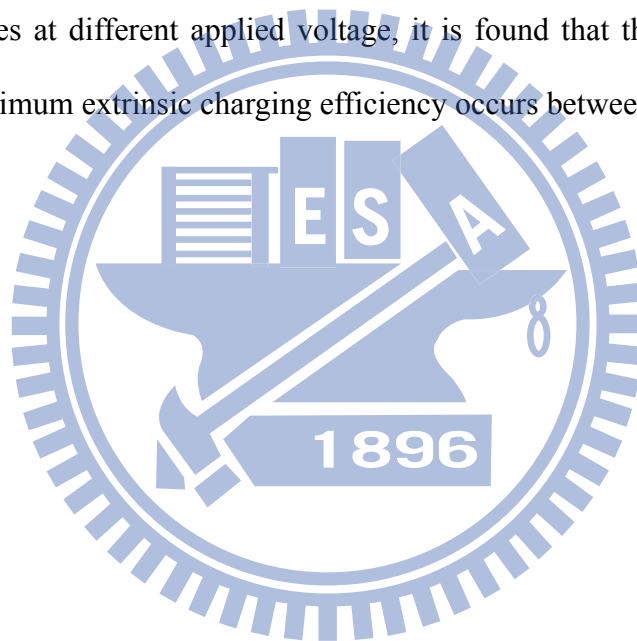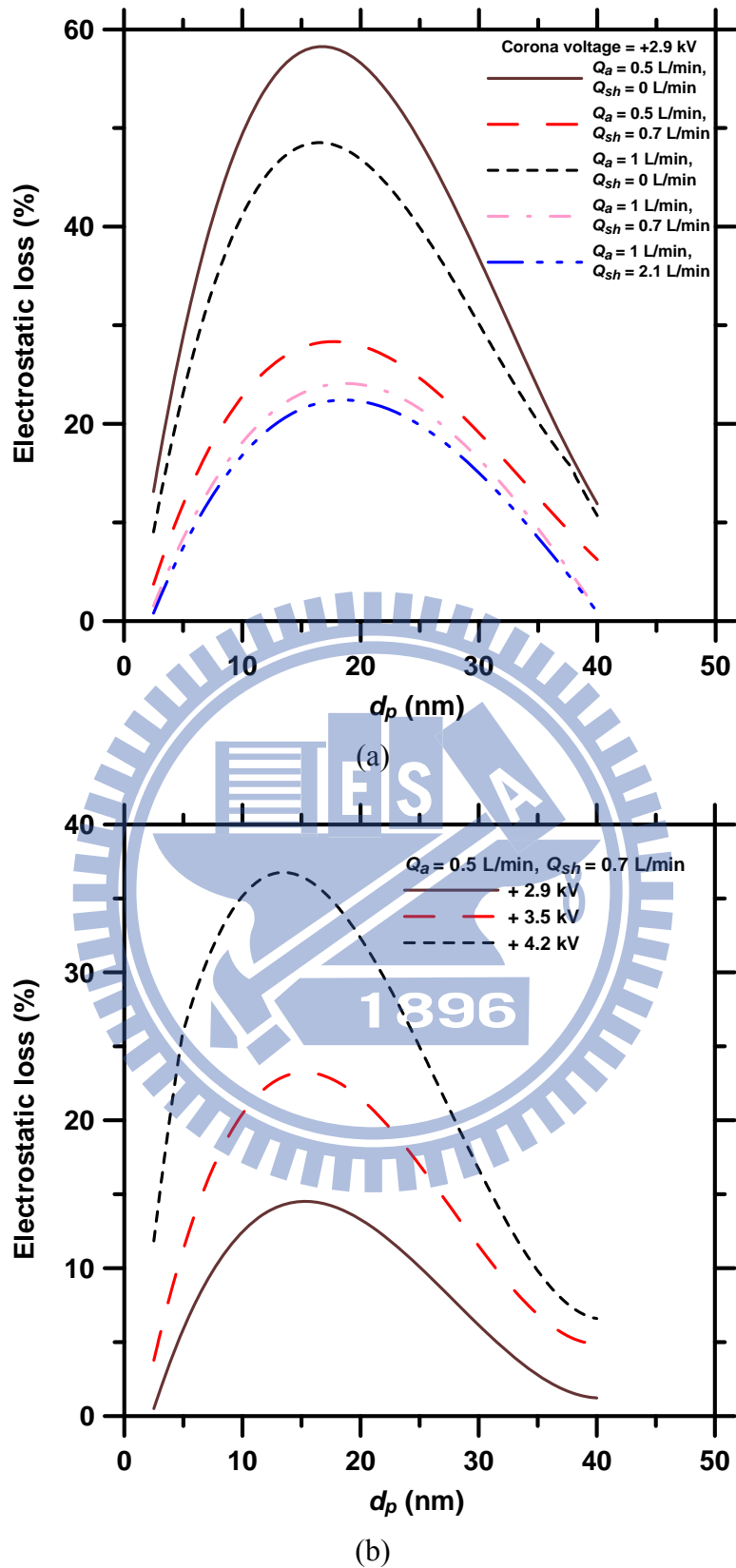
Figure 4.17 Electrostatic loss as a function of particle diameter of the charger with radial sheath air. (a) design 1, (b) design 2.

(a)

(b)
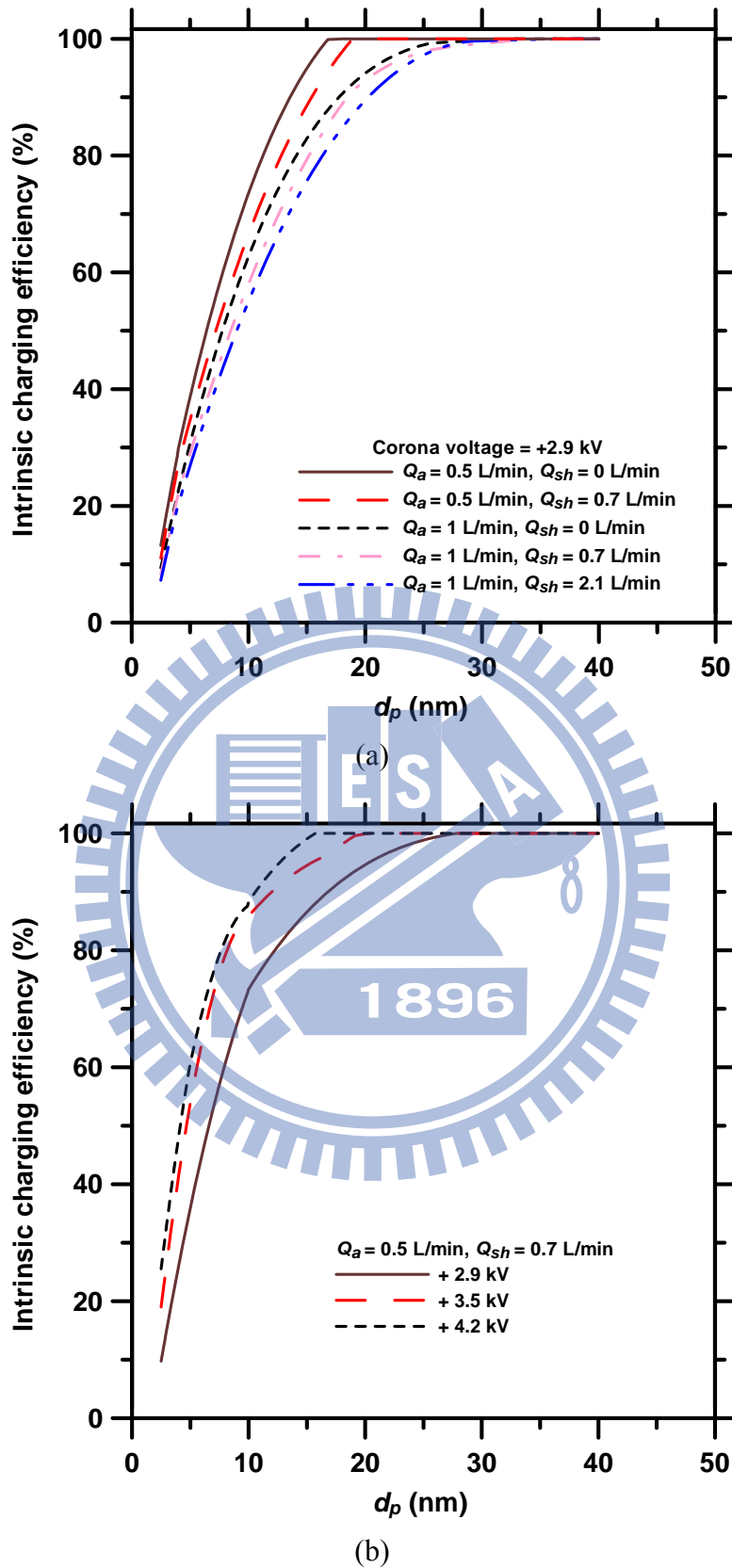
Figure 4.18 Intrinsic charging efficiency as a function of particle diameter of the charger with radial sheath air. (a) design 1, (b) design 2.

CHAPTER 5
CONCLUSIONS AND RECOMMENDATIONS
FOR FUTURE STUDY

5.1 Conclusions

This study designed a single-wire corona unipolar aerosol charger with axial sheath air to minimize charged particle loss. The charger consists of a cylindrical casing of 30 mm in inner diameter in which a gold wire of 50 μm in diameter and 2 mm in length is used as the discharge electrode. The experimental results show that the charger with axial sheath air has a good extrinsic charging efficiency of 3.1%–71.1% for particles ranging from 2.5 to 20 nm in diameter at the sheath air flow rate of 3 L/min.

A detailed 2-D numerical model was developed to predict the flow, electric potential, ion concentration, charged particle concentration fields, charged particle loss and charging efficiency in a single-wire corona unipolar charger. The predicted extrinsic charging efficiency is shown to be in good agreement with the experimental data of the charger with axial sheath air. Numerical results indicate the location where the major charged particle loss occurs inside the charger and further show that flow field is important to the electrostatic loss of charged particles. The present validated numerical model enables the design of an efficient corona-wire charger.

In order to improve the nanoparticle charging efficiency further, a single-wire corona unipolar charger with radial sheath air to minimize charged particle loss was proposed to enhance the charging efficiency of nanoparticles. The charger consists of an insulated Teflon tube of 6.35 mm in ID with a 6 mm long grounded porous metal tube inserted at the center from which radial sheath air is introduced, and a discharge gold wire of 50 μm in ID and 6 mm in effective length. The performance of the charger was evaluated and optimized by using the numerical model. The effect of the position of the sheath air

opening on reducing the loss of charged particles was found to be important and two different designs were studied. In design 1, both ends of 6 mm wide sheath air opening are aligned with the ends of 6 mm long discharge wire, while in design 2 the sheath air opening is shifted 2 mm toward the left of the leading edge of the wire.

Sheath air was found to have a considerable effect on reducing the loss of charged particles, especially when sheath air was introduced from the radial direction into the charging chamber. Compared to the charger with axial sheath air, no flow recirculation region for aerosol flow is observed near the wall of the charging zone of the charger with radial sheath air. For the effect of the position of the sheath air opening, design 2 has less electrostatic loss than design 1 because of its smaller deposition region of charged particles at the same operating condition. These results show the advantage of using radial sheath air with an appropriate position of the sheath air opening to minimize charged particle loss.

Design 2 operated at the applied voltage of +3.5 kV, Q_a = 0.5 L/min, and Q_{sh} = 0.7 L/min was found to have charging efficiency of 15.2%–65.8% for particles ranging from 2.5 to 10 nm in diameter, which is comparable to that of the charger of Chen and Pui (1999), 22%–65% for particles ranging from 3 to 10 nm in diameter, and that of the charger of Kimoto et al. (2010), 59%–64% for particles ranging from 5 to 10 nm in diameter. But there are no data available for comparison for particles below 3 nm in Chen and Pui (1999) and below 5 nm in Kimoto et al. (2010).

It is expected that the charger with radial sheath air designed in this study could be used as an efficient nanoparticle charger to improve the sensitivity of monitoring instruments for nanoparticles. In the future, the experiments will be conducted to validate the simulated results and to further enhance the feasibility of the charger.

5.2 Recommendations for future study

1. Variation in particle morphology and humidity can influence the charging efficiency (Kulkarni et al. 2011). Most aerosol particles, such as soot aggregates and dust particles, are non-spherical. Unipolar diffusion charging data for these non-spherical particles were shown to have higher charging efficiency than that for spherical particles (Ntziachristos et al. 2004; Jung and Kittelson 2005). Moreover, ion properties depend on the gas composition. For instance, water vapor, which is a primary clustering species in the atmosphere, may attach to the ions and lead to increased ion mass and decreased ion mobility (Davidson and Gentry 1984; Jung and Kittelson 2005). However, many investigators employ published values of the ion properties without considering the influence of humidity. Therefore, it is important to address the influence of particle morphology and humidity on the charging efficiency in the future.

2. In the current charger employing corona discharge, new particles may be generated by gas-to-particle conversion process if gas contaminants (such as NOx, SOx, and volatile organic vapors) are present (Liu et al. 1987; Murray et al. 1988; Hobbs et al. 1990). The potential particle deposition on the corona wire can result in unstable ion generation which requires investigation for possible solution.

3. The influence of discharge wire material on the operating time of the corona-wire charger has been studied (Asbach et al. 2004, 2005). Both gold and tungsten have been recommended as electrode material for continuous operation for more than three months. Future work should explore the use of other materials, such as tungsten wire for possible longer operation time.

APPENDIX: Comparison of the simulated intrinsic charging efficiency of the charger with radial sheath air with the theoretical results

The birth-and-death theory proposed by Boisdron and Brock (1970) was used to derive the theoretical intrinsic charging efficiency for the charger with radial sheath air. The basic equation for unipolar diffusion charging based on the birth-and-death theory can be written as (Adachi et al. 1985)

$$\frac{\partial N_{p,0}}{\partial t} = -\alpha_0 N_{p,0} N_i \tag{A1}$$

where $N_{p,0}$ is the number concentration of uncharged particles (particles/m³), t is the charging time (sec), α_0 is the combination coefficient of ions for uncharged particles (m³/s), and N_i is the ion concentration (ions/m³). The analytical solution of Equation (A1) can be derived as

$$\frac{N_{p,0}}{N_T} = \exp(-\alpha_0 N_i t) \tag{A2}$$

Equation (A2) can be rearranged as

$$1 - \exp(-\alpha_0 N_i t) = \frac{N_{p,T}}{N_T} \tag{A3}$$

where N_T is the number concentration of total uncharged particles at the inlet (particles/m³), $N_{p,T} (= N_T - N_{p,0})$ is the number concentration of total charged particles (particles/m³), and $\frac{N_{p,T}}{N_T}$ is the fraction of charged particles. Since the exponent $\alpha_0 N_i t$ in Equation (A3) is a dimensionless product, a charging parameter

α^* can be defined as

$$\alpha^* = \alpha_0 N_i t \qquad\qquad\qquad\qquad\qquad \text{(A4)}$$

That is, the fraction of charged particles (i.e., intrinsic charging efficiency) in the unipolar charger depends on the charging parameter α^*.

Theoretical Intrinsic Charging Efficiency

The theoretical fraction of charged particles curves as a function of the $Ni\ t$ product in the wire-in-tube ESP case are shown in Figure A1a. In general, the fraction of charged particles increases with the particle size and the $Ni\ t$ product. For example, the theoretical fraction of charged particles was 14.9–100% for particles ranging from 1 to 20 nm in diameter at the $Ni\ t$ product of 8.7×10^{14} ions-sec/m^3. Because of low charging probabilities, 1 nm particles are difficult to be charged even at high $Ni\ t$ product, which is to be expected. However, when these five fraction of charged particles curves were re-plotted using the charging parameter α^* as the abscissa, the curves of different particle sizes collapse into one, as shown in Figure A1b. Therefore, the parameter that governs the fraction of charged particles in the unipolar charger is the product of combination coefficient, ion concentration, and charging time. When $\alpha^* > 4.76$, the fraction of charged particles is found to be nearly 100%. Results show that the charging parameter α^* is better correlated to the curves of different particle sizes calculated based on the $Ni\ t$ product. The charging parameter α^* can be used as a critical parameter to characterize the performance of unipolar charger. For example, if the fraction of charged particles higher than 0.8 and 0.9 are used as the criteria for a high efficiency charging process, the optimum operating condition for the charger

should be $\alpha^* > 1.63$ and 2.45, respectively.

The relationship between the fraction of charged particles and charging parameter α^* in the charger with radial sheath air compared with the theoretical results of a wire-in-tube ESP case is shown in Figure A2. For design 1, the fraction of charged particles decreases with an increasing sheath air flow rate at a given aerosol flow rate. This is because a larger sheath air flow rate leads to a shorter charging time of particles in the charging zone. In addition, the curves of the fraction of charged particles of design 1 give similar agreement with the theoretical results, while the faction of charged particles curve of design 2 starts to deviate from the theoretical curve when $\alpha^* > 2$. For design 2, a relatively large discrepancy with the theoretical results was found for $2 < \alpha^* < 9$. It indicates that the position of the sheath air opening has an influence on the fraction of charged particles in the charger with radial sheath air. When shifting the position of the sheath air opening toward the left of the leading edge of the wire, its effect on the fraction of charged particles is not negligible.
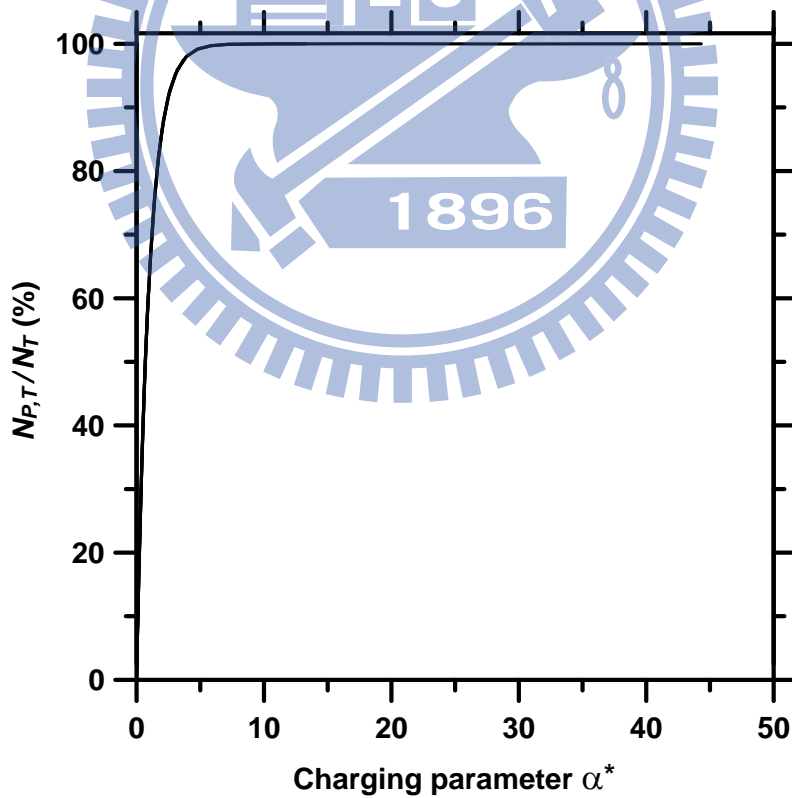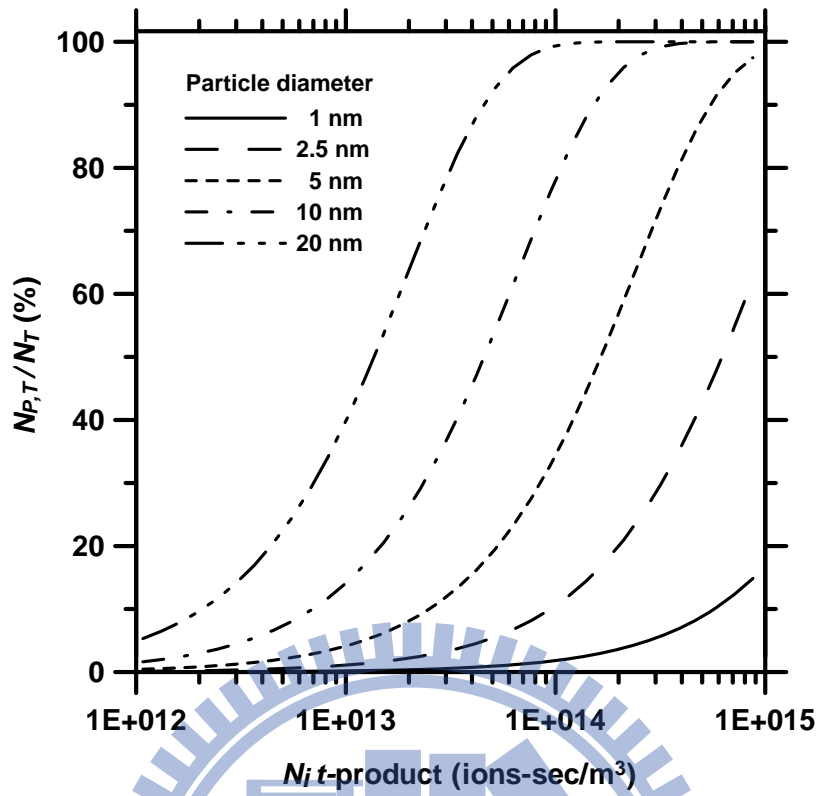
Figure A1 Fraction of charged particles in the wire-in-tube ESP. (a) $N_i\,t$ product as the abscissa, (b) charging parameter α^* as the abscissa.
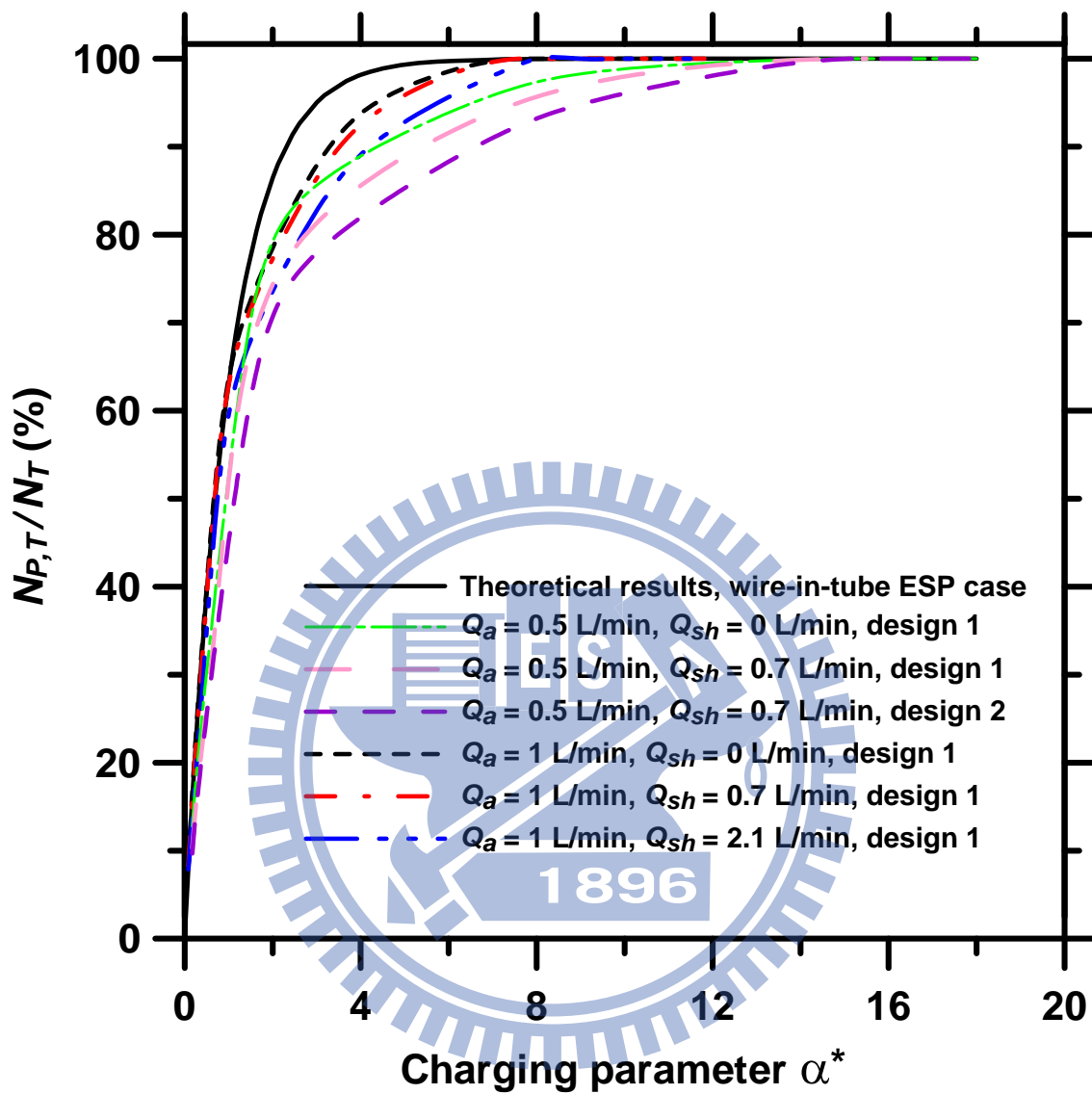
Figure A2 Fraction of charged particles as a function of charging parameter α^* in the charger with radial sheath air at the applied voltage of +2.9 kV.

REFERENCES

Adachi, M., Kousaka, Y., and Okuyama, K. (1985). Unipolar and Bipolar Diffusion Charging of Ultrafine Aerosol Particles. *J. Aerosol. Sci.* 16:109–123.

Adachi, M., Romay, F. J., and Pui, D. Y. H. (1992). High-efficiency Unipolar Aerosol Charger using a Radioactive Alpha Source. *J. Aerosol. Sci.* 23:123–137.

Aliat, A., Tsai, C. J., Hung, C. T., and Wu, J. S. (2008). Effect of Free Electrons on Nanoparticle Charging in a Negative Direct Current Corona Charger. *Appl. Phys. Lett.* 93:154103.

Aliat, A., Hung, C. T., Tsai, C. J., and Wu, J. S. (2009). Implementation of Fuchs' Model of Ion Diffusion Charging of Nanoparticles Considering the Electron Contribution in DC-Corona Chargers in High Charge Densities. *J. Phys. D: Appl. Phys.* 42:125206.

Alonso, M., Martin, M. I., and Alguacil, F. J. (2006). The Measurement of Charging Efficiencies and Losses of Nanoparticles in a Corona Charger. *J. Electrostat.* 64:203–214.

Alonso, M., Alguacil, F. J., and Borra, J. P. (2009). A Numerical Study of the Influence of Ion-aerosol Mixing on Unipolar Charging in a Laminar Flow Tube. *J. Aerosol. Sci.* 40:693–706.

Asbach, C., Kuhlbusch, T. A. J., and Fissan, H. (2004). Development of an Electrostatic Partitioner for Highly Efficient Partitioning of Gas and Particles with Minimal Effect on the Gas Phase. *Aerosol Sci. Technol.* 38:322–329.

Asbach, C., Kuhlbusch, T. A. J., and Fissan, H. (2005). Effect of Corona Discharge on the Gas Composition of the Sample Flow in a Gas Particle Partitioner. *J. Environ. Monit.* 7:877–882.

Biskos, G., Mastorakos, E., and Collings, N. (2004). Monte-Carlo Simulation of Unipolar Diffusion Charging for Spherical and Non-Spherical Particles. *J. Aerosol. Sci*. 35:707–730.

Biskos, G., Reavell, K., and Collings, N. (2005a). Electrostatic Characterisation of Corona-Wire Aerosol Chargers. *J. Electrostat.* 63:69–82.

Biskos, G., Reavell, K., and Collings, N. (2005b). Unipolar Diffusion Charging of Aerosol Particles in the Transition Regime. *J. Aerosol. Sci*. 36:247–265.

Boisdron, Y., and Brock, J. R. (1970). On the Stochastic Nature of the Acquisition of Electrical Charge and Radioactivity by Aerosol Particles. *Atmos. Environ.* 4:35–50.

Büscher, P., Schmidt-Ott, A., and Wiedensohler, A. (1994). Performance of a Unipolar "Square Wave" Diffusion Charger with Variable nt-Product. *J. Aerosol Sci.* 25:651–663.

Chen, D. R., Pui, D. Y. H., Hummes, D., Fissan, H., Quant, F. R., and Sem, G. J. (1998). Design and Evaluation of a Nanometer Aerosol Differential Mobility Analyzer (Nano-DMA). *J. Aerosol Sci.* 29: 497–509.

Chen, D. R., and Pui, D. Y. H. (1999). A High Efficiency, High Throughput Unipolar Aerosol Charger for Nanoparticles. *J. Nanopart. Res.* 1:115–126.

Cheng, S. H., Ranade, M. B., and Gentry. J. W. (1997). Experimental Design of High Volume Electrostatic Charger. *Aerosol Sci. Technol.* 26:433–446.

Davison, S. W., and Gentry, J. W. (1984). Modeling of Ion Mass Effects on the Diffusion Charging Process. *J. Aerosol. Sci*. 15:262–270.

Flagan, R. C. (1998). History of Electrical Aerosol Measurements. *Aerosol Sci. Technol.* 28:301–380.

Fuchs, N. A. (1963). On the Stationary Charge Distribution on Aerosol Particles in a Bipolar Ionic Atmosphere. *Geophys. Pura. Appl.* 56:185–193.

Hernandez-Sierra, A., Alguacil, F. J., and Alonso, M. (2003). Unipolar Charging of Nanometer Aerosol Particles in a Corona Ionizer. *J. Aerosol. Sci.* 34:733–745.

Hewitt, G. W. (1957). The Charging of Small Particles for Electrostatic Precipation. *AIEE Trans.* 76:300–306.

Hobbs, P. C. D., Gross, V. P., and Murray, K. K. (1990). Suppression of Particle Generation in a Modified Clean Room Corona Ionizer. *J. Aerosol. Sci.* 21:463–465.

Hoppel, W. A., and Frick, G. M. (1986). Ion-Aerosol Attachment Coefficients and the Steady-State Charge-Distribution on Aerosols in a bipolar Ion Environment. *Aerosol Sci. Technol.* 5:1–21.

Hinds, W. C. (1999). *Aerosol Technology*. John Wiley & Sons, New York.

Huang, C. H., and Alonso, M. (2011). Nanoparticle Electrostatic Loss within Corona Needle Charger during Particle-Charging Process. *J. Nanopart. Res.* 13:175–184.

Intra, P., and Tippayawong, N. (2009). Progress in Unipolar Corona Discharger Designs for Airborne Particle Charging: A Literature Review. *J. Electrostat.* 67:605–615.

Intra, P., and Tippayawong, N. (2011). An Overview of Unipolar Charger Developments for Nanoparticle Charging. *Aerosol Air Qual. Res.* 11:187–209.

ISO/TS 27687 (2008). Nanotechnologies -- Terminology and Definitions for Nano-objects -- Nanoparticle, Nanofibre and Nanoplate.

ISO/TS 80004-1 (2010). Nanotechnologies -- Vocabulary -- Part 1: Core Terms.

ISO/TS 80004-3 (2010). Nanotechnologies -- Vocabulary -- Part 3: Carbon Nano-objects.

Jung, H., and Kittelson, D. B. (2005). Characterization of Aerosol Surface Instruments in Transition Regime. *Aerosol Sci. Technol.* 39:902–911.

Kaptzov, N. A. (1947). *Elektricheskiye Yavleniya v Gazakh i Vacuume*. OGIZ, Moscow.

Kimoto, S., Saiki, K., Kanamaru, M., and Adachi, M. (2010). A Small Mixing-Type Unipolar Charger (SMUC) for Nanoparticles. *Aerosol Sci. Technol.* 44:872–880.

Kruis, F. E., and Fissan, H. (2001). Nanoparticle Charging in a Twin Hewitt Charger. *J. Nanopart. Res.* 3:39–50.

Kulkarni, P., Baron, P. A., and Willeke, K. (2011). *Aerosol Measurement*. John Wiley & Sons, Hoboken, NJ.

Li, L., and Chen, D. R. (2011). Performance Study of a DC-Corona-Based Particle Charger for Charge Conditioning. *J. Aerosol. Sci.* 42:87–99.

Lin, G. Y., and Tsai, C. J. (2010). Numerical Modeling of Nanoparticle Collection Efficiency of Single-Stage Wire-in-Plate Electrostatic Precipitators. *Aerosol Sci. Technol.* 44:1122–1130.

Liu, B. Y. H. and Pui, D. Y. H. (1975). On the Performance of the Electrical Aerosol Analyzer. *J. Aerosol Sci.* 6:249–264.

Liu, B. Y. H., Pui, D. Y. H., Kinstley, W. O., and Fisher, W. G. (1987). Aerosol Charging and Neutralization and Electrostatic Discharge in Clean Rooms. *J. Environ. Sci.* 30:42–46.

Marlow, W. H., and Brock, J. R. (1975). Unipolar Charging of Small Aerosol Particles. *J. Coll. Interface Sci.* 50:32–38.

Marquard, A., Kasper, M., Meyer, J., and Kasper, G. (2005). Nanoparticle Charging Efficiencies and Related Charging Conditions in a Wire-Tube ESP at DC

Energization. *J. Electrostat.* 63:693–698.

Marquard, A., Meyer, J., and Kasper, G. (2006a). Characterization of Unipolar Electrical Aerosol Chargers–Part II Application of Comparison Criteria to Various Types of Nanoaerosol Charging Devices. *J. Aerosol Sci.* 37:1069–1080.

Marquard, A., Meyer, J., and Kasper, G. (2006b). Characterization of Unipolar Electrical Aerosol Chargers–Part I A Review of Charger Performance Criteria. *J. Aerosol Sci.* 37:1052–1068.

Marquard, A. (2007). Unipolar Field and Diffusion Charging in the Transition Regime–Part I: A 2-D Limiting-Sphere Model. *Aerosol Sci. Technol.* 41:597–610.

Marquard, A., Meyer, J., and Kasper, G. (2007). Unipolar Field and Diffusion Charging in the Transition Regime–Part II: Charging Experiments. *Aerosol Sci. Technol.* 41:611–623.

Medved, A., Dorman, F., Kaufman, S. L., and Pocher, A. (2000). A New Corona-Based Charger for Aerosol Particles. *J. Aerosol Sci.* 31:S616–S617.

Murray, K. K., Ainsworth, G. F., and Gross, V. P. (1988). Hood Ionization in Semiconductor wafer processing: an evaluation. *EOS/ESD Symposium Proceedings*. 195–200.

Ntziachristos, N., Giechaskiel, B., Ristimäki, J., and Keskinen, J. (2004). Use of a Corona Charger for the Characterisation of Automotive Exhaust Aerosol. *J. Aerosol Sci*. 35:943–963.

Park, D., An, M., Hwang, J. (2007). Development and Performance Test of a Unipolar Diffusion Charger for Real-time Measurements of Submicron Aerosol Particles Having a Log-normal Size Distribution. *J. Aerosol Sci.* 38:420–430.

Patankar, S. V. (1980). *Numerical Heat Transfer and Fluid Flow*. Hemisphere, Washington, D. C.

Peek, F. W. (1929). *Dielectric Phenomena in High-Voltage Engineering*. McGraw-Hill, New York.

Pui, D. Y. H., Fruin, S., and McMurry, P. H. (1988). Unipolar Diffusion Charging of Ultrafine Aerosols. *Aerosol Sci. Technol.* 8:173–187.

Qi, C., Chen, D. R., and Pui, D. Y. H. (2007). Experimental Study of a New Corona-Based Unipolar Aerosol Charger. *J. Aerosol Sci.* 38:775–792.

Qi, C., Chen, D. R., and Greenberg, P. (2008). Performance Study of a Unipolar Aerosol Mini-Charger for a Personal Nanoparticle Sizer. *J. Aerosol Sci.* 39:450–459.

Qi, C., Asbach, C., Shin, W. G., Fissan, H., and Pui, D. Y. H. (2009). The Effect of Particle Pre-Existing Charge on Unipolar Charging and Its Implication on Electrical Aerosol Measurements. *Aerosol Sci. Technol.* 43:232–240.

Rohmann, H. (1923). Methode sur Messung der Grösse von Schwebeteilchen. *Z. Phys.* 17:253–265.

Romay, F. J., Pui, D. Y. H., and Adachi, M. (1991). Unipolar Diffusion Charging of Aerosol Particles at Low Pressure. *Aerosol Sci. Technol.* 15:60–58.

Romay, F. J., and Pui, D. Y. H. (1992a). On the Combination Coefficient of Positive Ions with Ultrafine Neutral Particles in the Transition and Free-Molecule Regimes. *Aerosol Sci. Technol.* 17:134–147.

Romay, F. J., and Pui, D. Y. H. (1992b). Free Electron Charging of Ultrafine Aerosol Particles. *J. Aerosol Sci.* 23:679–692.

Scheibel, H. G., and Porstendörfer, J. (1983). Generation of Monodisperse Ag- and

NaCl-Aerosol with Particle Diameters between 2 and 300 nm. *J. Aerosol Sci.* 14:113–126.

Tsai, C. J., Chen, S. C., Chen, H. L., Chein, H. M.,Wu, C. H., and Chen, T. M. (2008). Study of a Nanoparticle Charger Containing Multiple Discharging Wires in a Tube. *Sep. Sci. Technol.* 43:3476–3493.

Tsai, C. J., Lin, G. Y., Chen, H. L., Hunag, C. H., and Alonso, M. (2010). Enhancement of Extrinsic Charging Efficiency of a Nanoparticle Charger with Multiple Discharging Wires. *Aerosol Sci. Technol.* 44:807–816.

TSI Incorporated. (2006). Operation and Service Manual, Series 3080 Electrostatic Classifiers, Shoreview, MN, USA.

Unger, L., Boulaud, D., and Borra., J. P. (2004). Unipolar Field Charging of Particles by Electric Discharge: Effect of Particle Shape. *J. Aerosol Sci.* 35:965–979.

Vivas, M. M., Hontañón, E., Schmidt-Ott, A. (2008). Reducing Multiple Charging of Submicron Aerosols in a Corona Diffusion Charger. *Aerosol Sci. Technol.* 42:97–109.

Wang, S. C., and Flagan, R. C. (1990). Scanning Electrical Mobility Spectrometer. *Aerosol Sci. Technol.* 13:230–240.

Whitby, K. T. (1961). Generator for Producing High Concentrations of Small Ions. *Rev. Sci. Instrum.* 32:1351–1355.

Wiedensohler, A. (1988). An Approximation of the Bipolar Charge Distribution for Particles in the Submicron Size Range. *J. Aerosol Sci.* 19: 387–389.

Wiedensohler, A., Buscher, P., Hasson, H. C., Martinsson, B. G., Stratmann, F., Ferron, G., and Busch, B. (1994). A Novel Unipolar Charger for Ultrafine Aerosol Particles with Minimal Particle Losses. *J. Aerosol Sci.* 25: 639–649.

Curriculum Vitae

CHIH – LIANG CHIEN (簡誌良)

Institute of Environmental Engineering   Phone: +886-3-5712121 ext 55524

National Chiao Tung University   Email: clchien.ev91g@nctu.edu.tw

No. 1001, University Road, Hsinchu, 300, Taiwan.

Date of Birth / Nationality: May 26, 1978 / R.O.C.

Education

Ph.D. in Environmental Engineering, National Chiao Tung University   June 2012.

M.S. in Environmental Engineering, National Chiao Tung University   June 2006.

B.S. in Atmospheric Science, National Taiwan University   June 2000.

Positions

Adjunct Instructor, Department of Environmental Engineering and Health, Yuanpei University, Aug. 2011–Jan. 2012.

Awards and Honors

Excellent Paper Award (First Prize), Chinese Institute of Environmental Engineering, 2010.

The Most Popular Poster Award, TAAR, 2010.

Research Scholarship, Sinotech Foundation for Research and Development of Engineering Sciences and Technologies, 2009–2010.

Best Paper Award, TAAR, 2008.

Summer Institute Program Scholarship, NSC / DAAD, 2008.

Professional Service

Reviewer of Journal: Aerosol and Air Quality Research

Aerosol Science and Technology

Publication

Refereed Journals

1. **Chien, C. L.**, Tsai, C. J. (2012). Improvement of the Nanoparticle Charging Efficiency of a Single-wire Corona Unipolar Charger by Using Radial Sheath Air Flow: Numerical

Study, Aerosol Science and Technology. (in preparation)

2. **Chien, C. L.**, Tsai, C. J., Chen, H. L., Lin, G. Y., Wu, J. S. (2011). Modeling and Validation of Nanoparticle Charging Efficiency of a Single-Wire Corona Unipolar Charger, Aerosol Science and Technology, 45, 1468–1479. (SCI)

3. Liu, C. N., **Chien, C. L.**, Lo, C. C., Lin, G. Y., Chen, S. C., Tsai, C. J. (2011). Drag Coefficient of a Spherical Particle Attached on the Flat Surface, Aerosol and Air Quality Research, 11, 482–486. (SCI)

4. **Chien, C. L.**, Huang, S. H., Tsai, C. J. (2009). A New Cross-flow Tube Bundle Heat Exchanger with Staggered Hot and Cold Tubes for Thermophoretic Deposition of Submicron Aerosol Particles, Aerosol Science and Technology, 43, 1153–1163. (SCI)

5. **Chien, C. L.**, Tsai, C. J., Ku, K. W., Li, S. N. (2007). Ventilation Control of Air Pollutant during Preventive Maintenance of a Metal Etcher in Clean Room of Semiconductor Industry, Aerosol and Air Quality Research, 7, 469–488.

6. Tsai, C. J., Chang C. T., Liu, T. W., Huang, C. C., **Chien, C. L.**, Chien, H. M. (2004). Emission Characteristics and Control Efficiency of Acidic and Basic Gases and Aerosols from Packed Towers, Atmospheric Environment, 38, 643–646. (SCI)

Conference Papers

1. Tsai, C. J., **Chien, C. L.**, Chen, H. L., Lin, G. Y., Wu, J. S. (2011). Numerical Modeling of Nanoparticle Charging Efficiency of Corona-Wire Unipolar Aerosol Charger, Proceeding, 7th AAC conference, page 561, Xian, China, Aug. 17–20, 2011.

2. **Chien, C. L.**, Chen, H. L., Lin, G. Y., Tsai, C. J. (2010). Experimental and Numerical Study of a Nanoparticle Charger by Using Sheath Air Flow, Proceeding, 17th International Conference on Aerosol Science and Technology, Abstract no. p60, Taipei, Taiwan, Sep. 24–25, 2010.

3. Lin, G. Y., **Chien, C. L.**, Tsai, C. J. (2010). Numerical Modeling of Nanoparticle Collection Efficiency of Single-Stage Wire-in-Plate Electrostatic Precipitator, Proceeding, 17th International Conference on Aerosol Science and Technology, Abstract no. p50, Taipei, Taiwan, Sep. 24–25, 2010.

4. Tsai, C. J., **Chien, C. L.**, Chen, H. L., Lin, G. Y. (2010). Experimental and Numerical Study of a Nanoparticle Charger by Using Sheath Air Flow, International Aerosol Conference 2010, Abstract no. 7D4, Helsinki, Finland, Aug. 29–Sep. 3, 2010.

5. Lin, G. Y., **Chien, C. L.**, Tsai, C. J. (2010). A Mathematical Model for Predicting the Nanosized Particle Collection Efficiency in a Single-Stage Wire-in-Plate Wet Electrostatic Precipitator, International Aerosol Conference 2010, Abstract no. 4F5, Helsinki, Finland,

Aug. 29–Sep. 3, 2010.

6. **Chien, C. L.**, Tsai, C. J., Chen, H. L., Chen, S. C., Lin, G. Y. (2009). Enhancement of Charging Efficiency of a Nanoparticle Charger by Using Sheath Air Flow, AAAR 28th Annual Conference, Abstract no. 1190, Minneapolis, Minnesota, Oct. 26–30, 2009.

7. Liu, C. N., **Chien, C. L.**, Lo, C. C., Tsai, C. J. (2009). Drag Coefficient of a Sphere on the Flat Surface, AAAR 28th Annual Conference, Abstract no. 876, Minneapolis, Minnesota, Oct. 26–30, 2009.

8. Liu, C. N., **Chien, C. L.**, Lo, C. C., Lin, G. Y., Chen, S. C., Tsai, C. J. (2009). Drag Coefficient of a Sphere Attached on the Flat Surface, Proceeding, 16th International Conference on Aerosol Science and Technology, page 84, Chaoyang University of Technology, Taichung, Taiwan, Sep. 25–26, 2009.

9. Chou, Y. L., Ho, C. E., Tsai, C. J., Chen, C. W., Chang, C. P., Shih, T. S., **Chien, C. L.** (2009). Characteristics of Particles Emitted from Nanopowders Dispersed Using Different Methods, Proceeding, 4th International Conference on Nanotechnology-Occupational and Environmental Health, page 61, Helsinki, Finland, Aug. 26–29, 2009.

10. Huang, S. H., **Chien, C. L.**, Tsai, C. J. (2008). A Miniature Tube Bundle Heat Exchanger of Constant Temperature Gradient for Thermophoretic Deposition of Ultrafine Aerosol Particles, Proceeding, 15th International Conference on Aerosol Science and Technology, page 1, Jinwen University of Science and Technology, Taipei, Taiwan, Sep. 26–27, 2008.

11. Tsai, C. J., Lo, C. C., **Chien, C. L.** (2008). Formation of TiO_2 Nanoparticles in Combustion of Ti Metal Droplet, Proceeding, 15th International Conference on Aerosol Science and Technology, page 60, Jinwen University of Science and Technology, Taipei, Taiwan, Sep. 26–27, 2008.

12. Huang, S. H., **Chien, C. L.**, Tsai, C. J., Lo, C. C., Chen, S. C., Wu, C. H. (2008). Experimental and Numerical Study of Thermophoretic Deposition of Ultrafine Aerosol Particles in a Miniature Tube Bundle Heat Exchanger, 2008 EAC conference, Abstract no. T08A007O, Thessaloniki, Greece, Aug. 24–29, 2008.

13. **Chien, C. L.**, Tsai, C. J., Ku, K. W., Li, S. N. (2007). Ventilation Control of Pollutant Dispersion during Preventive Maintenance of a Metal Etcher in Semiconductor Industry, 5th AAC conference, Proceeding Vol. 1, page 76–77, Kaohsiung, Taiwan, Aug. 26–29, 2007.

14. Tsai, C. J., **Chien, C. L.** (2006). Control of Fugitive Gas Emission during the Preventive Maintenance of an Etcher of Semiconductor Industry, Proceeding, 13th International Conference on Aerosol Science and Technology, page B2–1 ~ B2–10, Chia-Nan Medical

University, Tainan, Taiwan, Sep. 29–30, 2006.

<u>Patents</u>

1. Tsai, C. J., Huang, S. H., **Chien, C. L.** (2011). Tube Bundle Heat Exchanger of Constant Temperature Gradient for Thermophoretic Deposition of Aerosol Particles, Taiwan patent I342946B1, US patent 7,934,542 B2.